

**Studies of Nanoscale Modification of Surfaces and Structures by  
Electrochemical Deposition of Gold and Polyaniline**

**Inaugural – Dissertation  
zur Erlangung des Doktorgrades  
der Mathematisch – Naturwissenschaftlichen Fakultät  
der Heinrich – Heine – Universität Düsseldorf**

vorgelegt von

**Lidiya Komsiyka**  
aus Pazardzhik, Bulgarien

Januar 2008

Aus der Institut für Bio- und Nanosysteme, Forschungszentrum Jülich

Gedruckt mit Genehmigung der Mathematisch-Naturwissenschaftlichen Fakultät  
der Heinrich-Heine-Universität Düsseldorf

Referent: Priv.-Doz. Dr. Georgi Staikov

Koreferent: Prof. Dr. Claus Seidel

Tag der mündlichen Prüfung: 10.01.2008

This work was performed at the Institute of Bio- and Nanosystems at the Research Center Jülich under the supervision of Priv.-Doz. Dr. Georgi Staikov. I would like to thank Prof. Dr. Harald Ibach for giving me the opportunity to work in the Institute in the frame of the Helmholtz research program “Information Technology with Nanoelectronic Systems”.

The present work would have not been completed without all the people who gave me help and support during these three years that I spend in Jülich. Here I want to express my gratitude to all of them.

My deepest thanks go to my supervisor Priv.-Doz. Dr. Georgi Staikov. This work would have been impossible without his guidance, encouragement and support. I am very grateful for the pleasant atmosphere and for the number of fruitful and instructive discussions. I am thankful for all the knowledge that I received from him.

I am also thankful to Prof. Dr. Claus Seidel for agreeing to be my second supervisor and evaluator of this thesis.

I would like to thank Dr. Gábor Mészáros and Priv.-Doz. Dr. Thomas Wandlowski for the fruitful and successful collaboration within the project on fabrication of Au-Au nanogaps and Au-PANI-Au nanobridges. I am also grateful to Dr. Dirk Mayer for supplying the work with lithographical structures.

I would like to express my gratitude also to Dr. Vessela Tsakova for encouraging and supporting me. I am grateful for the collaboration and for the numerous helpful and interesting discussions that we had and hopefully will have in the future.

I would like to thank also the co-workers in Research Center Jülich who contributed to this work, in particular Udo Linke for preparing the single crystal samples, Dr. Andres Muñoz for introducing me to the AFM technique and Dr. Guillermo Beltramo for the advice and help that he gave me. Great thanks go to Hans Peter Bochem and Marcel Merkwitz for performing the SEM measurements.

I thank also my present and former colleagues from the Institute of Bio- and Nanosystems for the friendly and pleasant working atmosphere in the institute.

These three years would have been not the same without the friends that I found here in Germany. I would like to thank Tsveti, Stefan, Julian, Katja, Ani and Svetlio for the encouragement and for always being there for me. I thank also Agnieszka and Misha for the great time that we had. Special thanks go to Anna for her support, her patience, her friendship and for the fun times. I would like to thank also my friends in Bulgaria, especially Magi, for the support and the care.

At last but not at least, I would like to thank my family. Благодаря ви мило ми семейство, че винаги стоите зад мен и зад всяко мое решение. Без вашата подкрепа нямаше да стигна до тук.

Research Center Jülich GmbH is gratefully acknowledged for the financial support.



### **Publications related to the thesis:**

L. Komsiyiska, V. Tsakova and G. Staikov,  
Electrochemical Formation and Properties of Thin Polyaniline Films on Au(111) and p-Si(111).

*Appl. Phys. A* 87 (2007) 405.

L. Komsiyiska and G. Staikov,  
Electrochemical Nucleation and Growth of Au nanoparticles on Glassy Carbon in  $[\text{AuCl}_4]^-$ -containing perchloric acid solution.

*in preparation.*

L. Komsiyiska, G. Mészáros, T. Wandlowski and G. Staikov,  
Fabrication of nanogaps and nanocontacts by Electrodeposition of Gold from a Thiosulfate-Sulfite Electrolytic Bath.

*in preparation.*

### **Poster presentations:**

L. Komsiyiska, V. Tsakova, G. Staikov,  
Electrochemical formation and metal modification of polyanilines layers for electrocatalytic purposes.

*5<sup>th</sup> Stranski-Kaishev- Surface Science Workshop on “Nanophenomena at surfaces– fundamentals of exotic condensed matter properties”*, Pamporovo, 19.02.-25.02.2005.

L. Komsiyiska, V. Tsakova, G. Staikov,  
Electrochemical growth and properties of thin polyaniline films on p-Si (111) and Au (111): A Comparative Study.

*Deutsche Physikalische Gesellschaft Jahrestagung 2006*, Dresden, 27.03.–31.03.2006.

L. Komsijska, V. Tsakova, G. Staikov,

Electrochemical formation and properties of thin polyaniline films on Au(111) and p-Si(111).

*10<sup>th</sup> International Fischer Symposium on "Electrochemical Aspects of Biological and Nanoscopic Structures"*, Benediktbeuern, 23.07-28.07.2006.

## **Research Reports**

L. Komsijska, G. Staikov,

Electrochemical growth and properties of thin polyaniline films on Au (111) and p-Si (111).

*Center of Nanoelectronic Systems for Information Technology, Research Center Jülich, Annual report 2005*, p.111.

L. Komsijska, G. Staikov,

Kinetics of Electrodeposition of gold Nanoparticles on Glassy Carbon.

*Center of Nanoelectronic Systems for Information Technology, Research Center Jülich, Annual report 2006*, p.119.

# Table of Contents

<b>1. Introduction and Objectives of the Thesis</b>	<b>1</b>
<b>2. Theoretical Background</b>	<b>4</b>
2.1 Electrochemical Phase Formation	4
2.1.1 General considerations	4
2.1.2 Metal electrodeposition	8
2.1.2.1 Mechanism and kinetics of initial deposition stages	9
2.1.2.2 Dynamic scaling analysis of growing surfaces	15
2.2 Conducting Polymers	17
2.2.1. General aspects	17
2.2.2 Electrochemical polymerization of polyaniline	20
2.2.3 The concepts of nucleation and growth in electropolymerization	22
2.3 Metal Nanocontacts and Nanogaps	23
2.3.1 Preparation and application of nanogaps	24
2.3.2 Conductance quantization and quantum tunnelling	25
<b>3. Experimental</b>	<b>27</b>
3.1 Electrolytes and Chemicals	27
3.2. Electrode Substrates	29
3.3. Substrate Holders	30
3.4 Electrochemical Cells and Instrumentation	31
3.4.1 Electrochemical experiments on GC, p-Si(111) and Au(111) macroelectrodes	31
3.4.2 Electrochemical low current measurements on microelectrode gold pairs	33
<b>4. Experimental Results and Discussion</b>	<b>36</b>
4.1 Modification of Glassy Carbon by Electrodeposition of Au Nanoparticles	36
4.1.1 Electrochemical nucleation and growth of Au nanoparticles	36

4.1.2	Modification of Au nanoparticles by Cu UPD	50
4.2	Electrochemical Deposition and Properties of Thin PANI Films	53
4.2.1	Kinetics and mechanism of PANI film formation on Au(111) and p-Si(111)	53
4.2.2	Electrochemical behaviour of PANI films on Au(111) and p-Si(111)	61
4.3	Nanoscale Modification of Gold Micro- and Nanostructures	66
4.3.1	AFM study of surface morphology during gold electrodeposition on Au(111)	66
4.3.2	Preparation and properties of gold nanogaps and nanocontacts	71
4.3.3	Preparation and properties of polyaniline nanojunctions	82
<b>5.</b>	<b>Summary and Outlook</b>	<b>93</b>
<b>6.</b>	<b>References</b>	<b>100</b>
	<b>Abbreviations</b>	<b>107</b>
	<b>Symbols</b>	<b>108</b>

# 1. Introduction and Objectives of the Thesis

The processes of electrochemical deposition are very flexible and effective tools for structuring and modification of solid state surfaces. This is mainly because the driving force and the rate of electrochemical phase formation can be controlled easily by the electrode potential and the current [1-8]. An important advantage of electrodeposition over the vapor deposition techniques is given by its high selectivity, which allows a uniform nanoscale modification of structures with extremely high aspect ratios. Another advantage of most electrodeposition techniques is their relatively low operation temperature (often room temperature), which reduces significantly the undesirable interdiffusion between involved materials. Due to these advantages electrodeposition has become recently of great significance for the development of micro- and nanosystem technologies. A typical example is the original electroplating technology (“Damascene plating”) developed by IBM for fabrication of on-chip metal interconnects of new generation electronic devices [9,10]. Many different technologically important materials such as metals, semiconductors and conducting polymers can be electrodeposited on a nanometer scale [7,11,12].

In recent years, of particular interest for the emerging nanotechnology has become the electrodeposition of gold. It is a powerful technique for controlled modification of relatively inert electrodes (like carbon, graphite and silicon) with gold nanoparticles, which exhibit very attractive size-dependent functional properties for various technological applications [13]. However, the key to a successful application of electrodeposition is the understanding of kinetics and mechanism of involved electrochemical phase formation processes in the particular electrochemical system. Although the possibility for electrodeposition of gold nanoparticles from cyanide-free electrolytes on various carbon substrates has been demonstrated by several groups [14-20], there are only few studies of the initial nucleation kinetics [21,22], which are of vital importance for the optimization of deposition conditions. In the present thesis the kinetics of electrochemical nucleation and growth of gold nanoparticles on glassy carbon (GC) are investigated in the systems GC/1mM KAuCl<sub>4</sub> + 0.1M HClO<sub>4</sub> and GC/5mM HAuCl<sub>4</sub> + 42mM Na<sub>2</sub>S<sub>2</sub>O<sub>3</sub> + 42mM Na<sub>2</sub>SO<sub>3</sub>.

As already mentioned above, the electrodeposition of conductive polymers is also of interest for nanotechnology. An interesting property of conductive polymers is the change of their conductivity by many orders of magnitude upon oxidation or reduction [23]. One of the most studied and promising conductive polymers is polyaniline (PANI). This material is characterized by an excellent electrochemical stability and a variety of stable red/ox forms exhibiting different chemical, physical and electronic properties. In electrochemical systems the switch between the conductive and the insulating states of PANI can be controlled by the electrode potential [24]. Recent studies on the charge transport through Au-PANI-Au nanojunctions have shown an abrupt red/ox switching between electrically insulating leucoemeraldine and conductive emeraldine forms [25,26]. This behaviour makes PANI very attractive for application in various sensor and nanoelectronic devices [27-31]. The development of optimal routines for preparation of such devices, however, requires a better understanding of electrochemical phase formation phenomena involved in the very initial stages of PANI electrodeposition on different substrates. The majority of studies on the electrochemical formation of PANI films reported in the literature have used polycrystalline noble metal electrodes such as Au and Pt [32-35]. However, there are only few reports [36,37] dealing with electrodeposition of PANI on silicon despite of the great technological importance of this material. Silicon poses a challenge as a substrate material because it undergoes an anodic oxidation in the potential range of aniline electropolymerization. Thus, the electrodeposition of PANI on silicon occurs practically in the presence of a thin anodic SiO<sub>2</sub> film, which can affect significantly the deposition kinetics and the properties of deposited polymer layers. However, this influence of the SiO<sub>2</sub> layer has not been taken into account in previous studies [36,37]. Therefore, in this thesis information on the role of anodic SiO<sub>2</sub> film in the process of PANI electrodeposition on silicon is obtained by comparative studies on Au(111) and p-Si(111) substrates.

The processes of electrodeposition of Au and PANI are very appropriate also for controlled nanoscale modification of various micro- and nanostructures [12,25,26,38]. In the present work these processes are applied for modification of lithographic Au microelectrode pairs and preparation of Au-Au nanogaps/nanocontacts and Au-PANI-Au nanojunctions.

The objectives of the present thesis are:

- (1) Investigation of initial stages of gold electrodeposition on glassy carbon (GC) from cyanide-free aqueous electrolytes with special emphasis to get an inside into nucleation and growth kinetics and to establish polarization routines for controlled deposition of gold nanoparticles.
- (2) Comparative studies of the mechanism of electrodeposition and the properties of thin PANI films on p-Si(111) and Au(111) substrates by means of electrochemical measurements and microscopic observations.
- (3) Studies of gold electrodeposition related to the modification of lithographically prepared planar pairs of Au microelectrodes in order to reduce the distance between the electrodes and to produce Au-Au nanogaps or nanocontacts.
- (4) Bridging of electrochemically prepared Au-Au nanogaps by selective PANI electrodeposition and characterization of the red/ox behaviour of the conductive polymer nanobridges by electrochemical measurements.

## 2. Theoretical Background

### 2.1 Electrochemical Phase Formation

#### 2.1.1 General considerations

The driving force for electrochemical formation of condensed phases is the electrochemical supersaturation defined by [4,6-8]

$$\Delta\tilde{\mu} = \tilde{\mu}_{(\text{el})} - \tilde{\mu}_{(\text{c})} \quad (2.1)$$

where  $\tilde{\mu}_{\text{el}}$  and  $\tilde{\mu}_{\text{c}}$  represent the electrochemical potentials of the monomer species in the parent electrolyte phase (el) and in the condensed bulk phase (c), respectively. The energy for formation of a cluster consisting of  $n$  monomer particles (atoms, ions or molecules) is given by [4,6-8]

$$\Delta\tilde{G}(n) = -n\Delta\tilde{\mu} + \Phi(n) \quad (2.2)$$

The first term in this Equation is always negative and is related to the transfer of  $n$  monomer particles from the electrolyte to the substrate under the action of the supersaturation  $\Delta\tilde{\mu}$ . The second term  $\Phi(n)$  takes into account the energy contributions due to the creation of new interfaces by the cluster formation. For sufficiently large clusters  $\Phi(n)$  can be derived using the specific interfacial energies in the system substrate/cluster/electrolyte.

Applying this classical thermodynamic approach to the formation of clusters of a condensed three-dimensional (3D) phase one obtains for the formation energy

$$\Delta\tilde{G}_{3\text{D}}(n) = -n\Delta\tilde{\mu}_{3\text{D}} + C_{3\text{D}}n^{2/3} \quad (2.3)$$



where  $\Delta\tilde{\mu}_{3D}$  represents the supersaturation with respect to the condensed 3D phase and  $C_{3D}$  is a constant depending on the cluster shape geometry and the specific interfacial energies in the system substrate/cluster/electrolyte. The  $\Delta\tilde{G}_{3D}(n)$  function given by Equation (2.3) exhibits a maximum at  $n = n_{\text{crit}}$  (Figure 2.1), which is a characteristic feature for the formation of condensed phases by a first order phase transition. The  $n_{\text{crit}}$ -sized cluster stays in metastable equilibrium with the parent phase and is called *critical nucleus*. Only clusters with a size  $n > n_{\text{crit}}$  can grow spontaneously under the action of applied supersaturation  $\Delta\tilde{\mu}_{3D}$ .

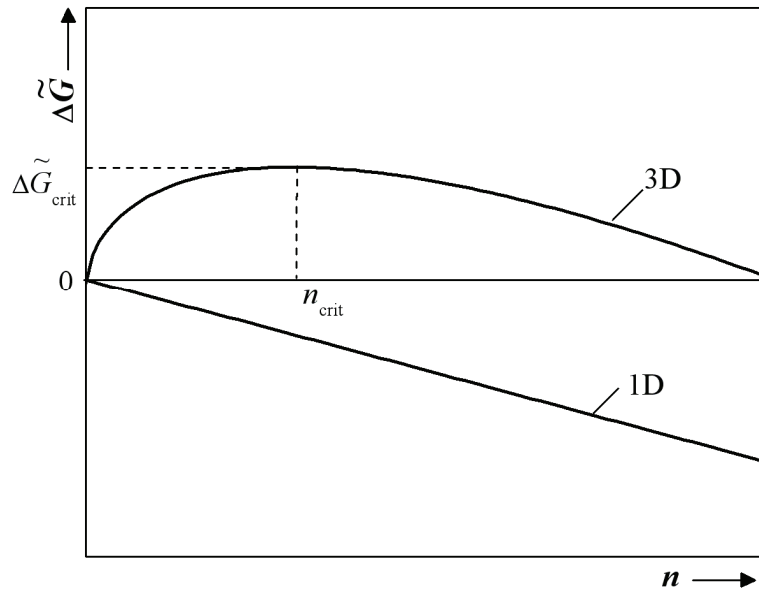


**Figure 2.1** The Gibbs free energy  $\Delta\tilde{G}$  for formation of cluster of a condensed three-dimensional (3D) and one-dimensional (1D) phase as a function of the size of the cluster  $n$ .

The energy barrier for nucleation  $\Delta\tilde{G}_{3D}(n_{\text{crit}})$  and the critical nucleus size  $n_{\text{crit}}$  are determined by the extremum condition ( $[\partial\Delta\tilde{G}_{3D}(n)/\partial n]_{n=n_{\text{crit}}} = 0$ ) and according to Equation (2.3) are interrelated by

$$\Delta\tilde{G}_{3D}(n_{\text{crit}}) = \frac{1}{2}n_{\text{crit}}\Delta\tilde{\mu}_{3D} = \frac{4C_{3D}^3}{27(\Delta\tilde{\mu}_{3D})^2} \quad (2.4)$$

Applying the same approach to the formation of a condensed 2D phase one obtains

$$\Delta\tilde{G}_{2D}(n_{\text{crit}}) = n_{\text{crit}}\Delta\tilde{\mu}_{2D} = \frac{C_{2D}^2}{4\Delta\tilde{\mu}_{2D}} \quad (2.5)$$

where  $\Delta\tilde{\mu}_{2D}$  is the supersaturation with respect to the condensed 2D phase and the constant  $C_{2D}$  depends on the shape and the specific edge energy of the 2D critical nucleus.

The formation of clusters of a condensed 1D phase (linear chain of monomers) is of particular importance for the understanding of the initial stages of electrochemical polymerization. Thus, in the following this case will be briefly considered in the framework of the classical thermodynamic approach. According to this approach the energy of 1D cluster formation can be expressed by the Equation [34,39,40]

$$\Delta\tilde{G}_{1D}(n) = -n\Delta\tilde{\mu}_{1D} + C_{1D} \quad (2.6)$$

where  $\Delta\tilde{\mu}_{1D}$  is the supersaturation with respect to the condensed 1D phase and  $C_{1D}$  is a constant related to the specific surface energy of the both ends of the 1D cluster (chain of monomers). As can be seen from Equations [(2.4)-(2.6)] and Figure 2.1, in contrast to  $\Delta\tilde{G}_{3D}(n)$  and  $\Delta\tilde{G}_{2D}(n)$  the energy of 1D cluster formation  $\Delta\tilde{G}_{1D}(n)$  is a linearly decreasing function of  $n$  and does not exhibit a maximum. This behavior shows that the concept of critical nucleus cannot be applied in this case and the only thermodynamic barrier for initiation of the process of 1D phase formation is connected with the deposition of the first monomer particle on the substrate surface.

As already mentioned the classical thermodynamic approach can be applied for calculation of  $\Phi(n)$  only in the cases of nuclei, consisting of sufficiently large number of monomer particles. However, in the case of very small nuclei, where the use of macroscopic quantities such as specific interfacial energies is no more justified and  $\Phi(n)$  and  $\Delta\tilde{G}(n)$  can be calculated applying the so-called atomistic approach, which is based on the use of the binding energies  $\phi_i$  of monomer particles in different positions  $i$  of the small cluster [4,6-8,41,42]. In contrast to the classical approach the calculations by the atomistic model show that for small critical nuclei  $n_{\text{crit}}$  remains constant in relatively large supersaturation intervals (Figure 2.2).

In each of these intervals the energy barrier for formation of critical nuclei is given by the equation

$$\Delta\tilde{G}(n_{\text{crit}}) = -n_{\text{crit}}\Delta\tilde{\mu} + \Phi(n_{\text{crit}}) = -n_{\text{crit}}\Delta\tilde{\mu} + n_{\text{crit}}\phi_{\infty} - \sum_{i=1}^{n_{\text{crit}}} \phi_i \quad (2.7)$$

where  $\phi_{\infty}$  is the binding energy of a monomer particle in the infinitely large condensed bulk phase.

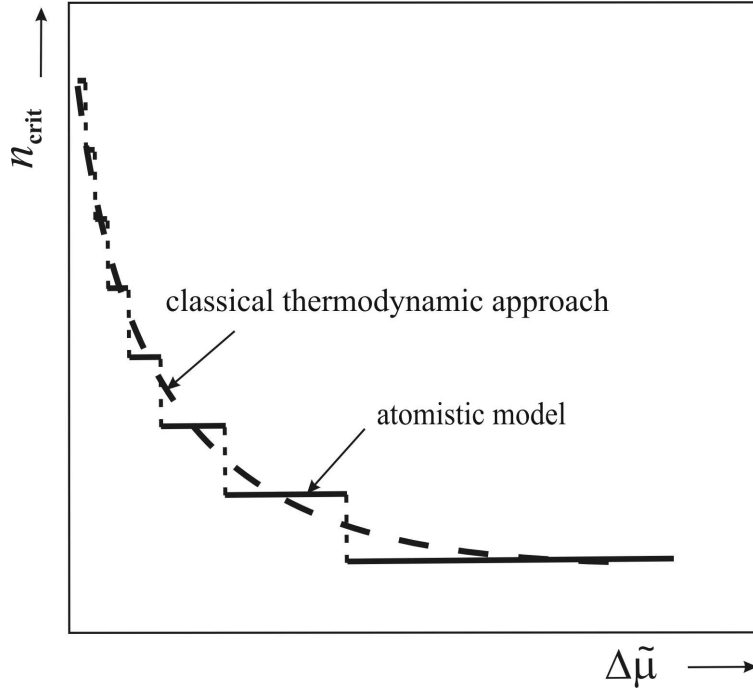


**Figure 2.2** Schematic representation of dependences of the size of critical nucleus  $n_{\text{crit}}$  on the supersaturation  $\Delta\tilde{\mu}$  according to the classical thermodynamic approach (dashed line) and to the atomistic model (solid lines).

The formation of nuclei is a fluctuation process, which can be considered as a sequence of random nucleation events. The corresponding stationary nucleation rate can be expressed generally by [4, 6-8, 41, 42]

$$J = \omega_+ Z N_0 \exp\left(-\frac{\Delta\tilde{G}(n_{\text{crit}})}{k_B T}\right) \quad (2.8)$$

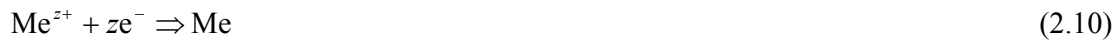
where  $\omega_+$  is the frequency of attachment of monomer particles to the critical nucleus,  $Z$  is the so-called “Zeldovich factor” and  $N_0$  is the number density of active nucleation sites of the substrate. The time dependence of the number density of nuclei  $N(t)$  formed on a substrate exhibiting equally active nucleation sites  $N_0$  can be described by [2-8]

$$N(t) = N_0 [1 - \exp(-f_n t)] \quad (2.9)$$

where  $f_n$  represents the frequency of nucleation per nucleation site. For very high nucleation frequencies  $f_n$  all nucleation sites  $N_0$  convert to nuclei practically instantaneously and the process is called *instantaneous nucleation*. At relatively low  $f_n$ , however, the nucleation sites convert to nuclei progressively with a stationary nucleation rate  $J = N_0 f_n$  and the process is known as *progressive nucleation*.

### 2.1.2 Metal electrodeposition

Electrochemical metal deposition occurs on a foreign or an own substrate from an electrolyte containing simple or complex ions of depositing metal (Me) and can be expressed by



where  $\text{Me}^{z+}$  represents the simple metal cations,  $L^{y-}$  is a ligand and  $m$  is the number of ligands forming the complex metal ions  $[\text{MeL}_m]^{(my-z)-}$ . Simple cations of some metals are not stable in aqueous medium and the deposition process can be realized only from aqueous electrolytes containing complex metal ions. A typical example is the electrochemical deposition of gold which can be performed from aqueous electrolytes containing complex Au ions such as  $[\text{Au}(\text{CN})_2]^-$ ,  $[\text{AuCl}_4]^-$ ,  $[\text{Au}(\text{SO}_3)_2]^{3-}$ ,  $[\text{Au}(\text{S}_2\text{O}_3)_2]^{3-}$  etc..

The electrons ( $\text{e}^-$ ) required for deposition reactions (2.10) and (2.11) can be supplied in two different ways [5, 7]:

- (i) by a Red/Ox reaction ( $\text{Red} \Rightarrow \text{Ox} + ze^-$ ) occurring simultaneously on the substrate
- (ii) by an external source applying a cathodic potential on the substrate.

However, in the first case known as “electroless deposition” the process takes place under open circuit conditions and a direct measurement of the metal deposition rate by the current is impossible. In the second case called “electrodeposition” the deposition rate and the supersaturation of the process can be controlled and measured easily by the electrode potential of the substrate  $E$  and the current density  $i$ . This offers many possibilities for a detailed study of kinetics and mechanism of electrodeposition process.

### 2.1.2.1 Mechanism and kinetics of initial deposition stages

The mechanism of metal electrodeposition on a foreign substrate is determined mainly by the metal-substrate interaction and the crystallographic metal-substrate misfit. In the case of weak metal-substrate interaction the deposition process is independent on the crystallographic misfit and starts with the formation of islands of the 3D Me phase at electrode potentials  $E$  more negative than the Nernst equilibrium potential  $E_{3\text{DMe}}$ , i.e. in the so-called overpotential deposition (OPD) range  $E < E_{3\text{DMe}}$  [4-8]. The driving force of the process, the supersaturation  $\Delta\tilde{\mu}_{3\text{D}}$  is related to the overpotential  $\eta = E - E_{3\text{DMe}} < 0$  by

$$\Delta\tilde{\mu} = -ze\eta > 0 \quad (2.12)$$

This deposition mode is called “Volmer-Weber” growth mode and is shown schematically in Figure 2.3a. In systems with strong metal-substrate interaction, however, the deposition process can start at undersaturations (underpotentials) with respect to the 3D Me phase ( $\Delta\tilde{\mu} = -ze(E - E_{3\text{DMe}}) < 0$ ). This phenomenon is known as underpotential deposition (UPD) and leads to formation of 2D Me phases (monolayers), which act as precursors for the OPD of the 3D Me phase [4, 8, 39]. In the case of significant metal-substrate misfit the deposition takes place by formation of unstrained 3D Me islands on top of predeposited and strained UPD monolayers, a mechanism known as “Stranski-Krastanov” growth mode (Figure 2.3b). If the crystallographic metal-substrate misfit is small the deposition follows a layer-by-layer or “Frank-van der Merwe” growth mechanism (Figure 2.3c).

Of particular importance for the modification of surfaces with nanoscopic metal particles are the systems showing a Volmer-Weber island growth (cf. Figure 2.3a). In such systems the islands of the 3D Me phase form on a bare substrate (i.e. in absence of an UPD layer) and in the initial deposition stages the overall rate of the process is determined by both the nucleation rate and the growth rate of newly formed metal particles.

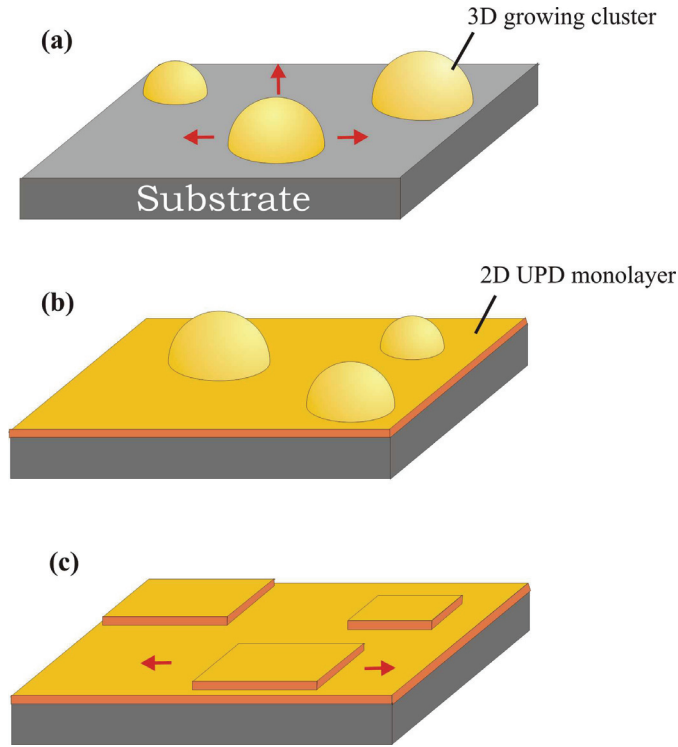


**Figure 2.3** Schematic representation of possible mechanisms of metal electrodeposition on foreign substrate (a): “Volmer-Weber” growth mode; (b): “Stranski-Krastanov” growth mode; (c): “Frank-van der Merwe” growth mechanism.

The current  $I_1(t)$  for the growth of a single isolated hemispherical metal particle under mixed charge transfer and diffusion control is given by [6,8,43-45]

$$|I_1(t)| = p \frac{1 + (t/\tau) - [1 + 2(t/\tau)]^{1/2}}{[1 + 2(t/\tau)]^{1/2}} \quad (2.13)$$

The parameters  $p$  and  $\tau$  are defined by

$$p = \frac{4\pi(zFDc)^2 [1 - \exp(zF\eta / RT)]^2}{i_0 [\exp(-(1-\alpha)zF\eta / RT) - \exp(\alpha zF\eta / RT)]} \quad (2.14)$$

$$\tau = \frac{(zF)^2 Dc [1 - \exp(zF\eta / RT)]}{V_m \{i_0 [\exp(-(1-\alpha)zF\eta / RT) - \exp(\alpha zF\eta / RT)]\}^2} \quad (2.15)$$

where  $D$  and  $c$  are the diffusion coefficient and the bulk concentration of metal ions in the electrolyte,  $i_0$  is the exchange current density,  $(1-\alpha)$  is the cathodic charge transfer coefficient and  $V_m$  represents the molar volume of an atom in the metal particle. For sufficiently short deposition times ( $t < 0.1\tau$ ) the growth of the metal particle is controlled by the charge transfer and Equation (2.13) reduces to

$$|I_1(t)| = \frac{p}{2} \left( \frac{t}{\tau} \right)^2 = K_{ct}(\eta) t^2 \quad (2.16)$$

where  $K_{ct}(\eta) = 2\pi(V_m / zF)^2 \{i_0 [\exp(-(1-\alpha)zF\eta / RT) - \exp(\alpha zF\eta / RT)]\}^3$ . At relatively long deposition times ( $t > 100\tau$ ) the growth becomes diffusion controlled and is described by

$$|I_1(t)| = p \left( \frac{t}{2\tau} \right)^{1/2} = K_d(\eta) t^{1/2} \quad (2.17)$$

where  $K_d(\eta) = \pi zF V_m^{1/2} (2Dc)^{3/2} [1 - \exp(zF\eta / RT)]^{3/2}$ . This behavior is illustrated in the non-dimensional  $\lg(|I_1(t)|/p)$  vs  $\lg(t/\tau)$  plot of Equation (2.13) in Figure 2.4 and shows that the formation of metal particles in the very initial deposition stages (nucleation stages) will take place in all cases under charge transfer control. Under these conditions the attachment frequency of single metal atoms to the critical nucleus is given by  $\omega_+ \sim i_0 \exp[-(1-\alpha)ze\eta / k_B T]$  and according to the atomistic nucleation theory (cf. Equations (2.7), (2.8) and (2.12)) for the overpotential dependence of the nucleation rate follows

$$J(\eta) = A(n_{crit}) \exp \left[ - \frac{(1-\alpha + n_{crit})ze\eta}{k_B T} \right] \quad (2.18)$$

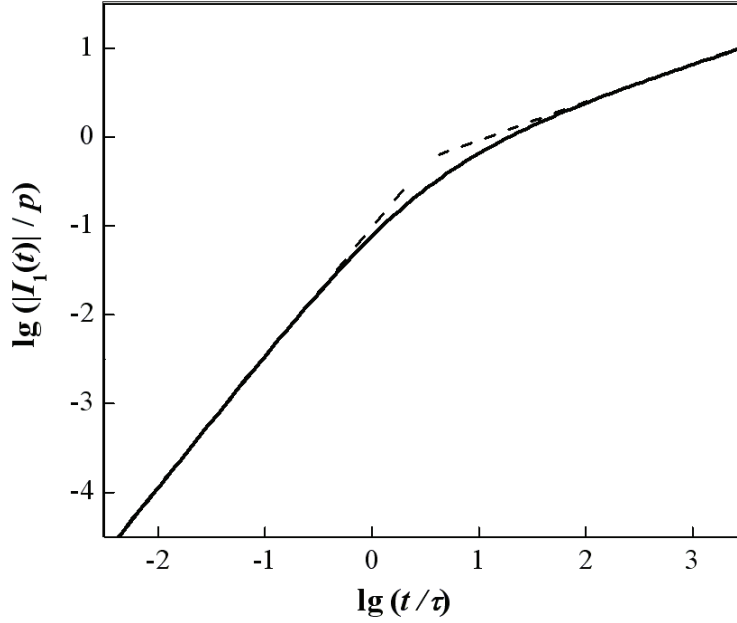


**Figure 2.4** Non-dimensional  $\lg(|I_1(t)|/p)$  vs.  $\lg(t/\tau)$  plot of Equation (2.13).

The 3D hemispherical growth considered above supposes that the growing metal particle has no preferred growth direction. However, if the growth rate in the lateral direction is much higher than vertical growth rate the particle growth becomes quasi two-dimensional. In this case the current for the charge transfer controlled 2D growth of a single particle depends linearly on time and can be expressed by [2-4]

$$|I_1(t)| = k_{ct}(\eta)t \quad (2.19)$$

with  $k_{ct}(\eta) = 2bd(V_m / zF)\{i_0[\exp(-(1-\alpha)zF\eta / RT) - \exp(\alpha zF\eta / RT)]\}^2$  where  $d$  is the thickness of the growing 2D particle and  $b$  is a geometric factor depending on its shape ( $b = \pi$  for a disc).

At high supersaturations (high cathodic overpotentials) and/or active substrates the overall electrodeposition process occurs usually by formation and growth of multiple nuclei. In very initial stages of the process the appearance and growth of individual metal particles can be considered as independent. The expressions for the initial overall current density  $|i(t)|$  derived under these conditions on the basis of Equations (2.16), (2.17) and (2.19) for the cases of instantaneous and progressive nucleation are given in Table 2.1.



**Table 2.1** Time dependences of the initial current density  $|i(t)|$  for different nucleation and growth models [2-4]. The growth constants  $k_{ct}$ ,  $K_{ct}$  and  $K_d$  are given by the Equations:

$$k_{ct}(\eta) = 2bh(V_m / zF) \{i_0 [\exp(-(1-\alpha)zF\eta / RT) - \exp(\alpha zF\eta / RT)]\}^2$$

$$K_{ct}(\eta) = 2\pi(V_m / zF)^2 \{i_0 [\exp(-(1-\alpha)zF\eta / RT) - \exp(\alpha zF\eta / RT)]\}^3$$

$$K_d(\eta) = \pi zF V_m^{1/2} (2Dc)^{3/2} [1 - \exp(zF\eta / RT)]^{3/2}$$

growth dimensionality	shape of growing centers	controlling growth step	nucleation type	current density
2D	discs	charge transfer	instantaneous	$ i(t)  = k_{ct}(\eta) N_0 t$
			progressive	$ i(t)  = \frac{1}{2} k_{ct}(\eta) J t^2$
3D	hemispheres	charge transfer	instantaneous	$ i(t)  = K_{ct}(\eta) N_0 t^2$
			progressive	$ i(t)  = \frac{1}{3} K_{ct}(\eta) N_0 t^3$
		diffusion	instantaneous	$ i(t)  = K_d(\eta) N_0 t^{1/2}$
			progressive	$ i(t)  = \frac{2}{3} K_d(\eta) N_0 t^{3/2}$

In the advanced deposition stages, however, the growth of individual metal particles can not be considered anymore as independent and the interference and overlapping of individual metal particles and/or their diffusion zones of reduced nucleation rate have to be taken into account. In order to solve this problem the actual free surface fraction  $1 - \theta(t)$  available for nucleation is described usually by the Kolmogorov-Avrami relation [2-4, 46, 47]

$$1 - \theta(t) = \exp[-\theta_{ext}(t)] \quad (2.20)$$

where  $\theta_{ext}(t)$  represents the so-called “extended” surface fraction that would be covered by the growing particles and/or their diffusion zones disregarding their interference.

Applying this approach were derived various expressions for the overall current transients using different theoretical models [2-8,48-52]. Theoretical current density transients  $i(t)$  derived on the basis of the model involving diffusion controlled 3D hemispherical growth of metal particles show characteristic maxima and in the limiting cases of progressive and instantaneous nucleation can be expressed by [49]

$$\left[ \frac{i(t)}{i_{\max}} \right]_{\text{inst}}^2 = 1.9542 \left( \frac{t}{t_{\max}} \right)^{-1} \left\{ 1 - \exp \left[ -1.2564 \left( \frac{t}{t_{\max}} \right) \right] \right\}^2 \quad (2.21)$$

$$\left[ \frac{i(t)}{i_{\max}} \right]_{\text{prog}}^2 = 1.2254 \left( \frac{t}{t_{\max}} \right)^{-1} \left\{ 1 - \exp \left[ -2.3367 \left( \frac{t}{t_{\max}} \right)^2 \right] \right\}^2 \quad (2.22)$$

where  $i_{\max}$  and  $t_{\max}$  are the corresponding current maxima coordinates, which are coupled by

$$(i_{\max}^2 t_{\max})_{\text{prog}} = 0.2598 (zFc)^2 D \quad (2.23)$$

$$(i_{\max}^2 t_{\max}^3)_{\text{prog}} = 0.2898 (zF)^2 \left[ \frac{c^3}{8\pi V_m J^2} \right]^{1/2} \quad (2.24)$$

$$(i_{\max}^2 t_{\max})_{\text{inst}} = 0.1629 (zFc)^2 D \quad (2.25)$$

$$(i_{\max}^2 t_{\max}^2)_{\text{inst}} = 0.065 (zF)^2 \left[ \frac{c^3}{8\pi V_m N_0^2} \right]^{1/2} \quad (2.26)$$

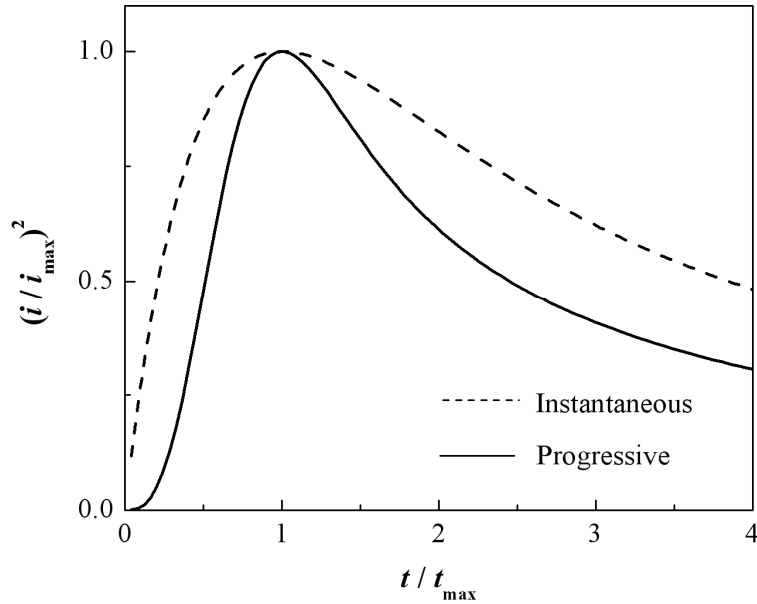


**Figure 2.5**  $[i(t)/i_{\max}]^2$  vs.  $(t/t_{\max})$  plots corresponding to Equation (2.21) (progressive nucleation) and Equation (2.22) (instantaneous nucleation).

The  $[i(t)/i_{\max}]^2$  vs.  $(t/t_{\max})$  plots corresponding to Equations (2.21) and (2.22) are shown in Figure 2.5. As seen the limiting cases of progressive and instantaneous nucleation can be clearly distinguished using such plots.

The above theoretical considerations are related to the initial stages of metal electrodeposition on foreign substrates and are of vital importance for the understanding of the kinetics and mechanism of deposition of metal nanoparticles, which has become recently a subject of intensive theoretical and experimental studies. In the more advanced deposition stages (after the coalescence of growing particles the metal deposition process proceeds practically on a substrate of the same metal (on an own substrate).

The evolution of surface morphology of metal deposits depends on deposition parameters and is of considerable interest for many practical applications of metal electrodeposition. A powerful approach for investigation of the temporal evolution of the topography of a growing surface during metal electrodeposition is the so-called “dynamic scaling approach”, which will be discussed in the following section.

### 2.1.2.2 Dynamic scaling analysis of growing surfaces

According to the dynamic scaling concept [53-56] the evolution of the surface roughness  $w$  can be expressed by

$$w(L, t) = L^H F(t / L^{H/\beta}) \quad (2.27)$$

where  $L$  is the length scale over which  $w$  is measured,  $F(t / L^{H/\beta})$  is a scaling function, and  $H$  and  $\beta$  are the so-called “roughness” and “growth” scaling exponents, respectively. In Equation (2.27)  $w(L)$  is defined as a root mean square (rms) surface roughness by

$$w(L) = \sqrt{\langle (h' - \langle h' \rangle)^2 \rangle} \quad (2.28)$$

where  $h'$  is the surface height. For  $t/L^{H/\beta} \gg 1$  the scaling function  $F(t/L^{H/\beta})$  is constant and for scale lengths smaller than the critical length  $L_c$ , above which  $w$  reaches a saturated value  $w_s$  ( $L \ll L_c$ ) Equation (2.27) reduces to

$$w(L, t) \sim L^H \quad (2.29)$$

At  $t/L^{H/\beta} \ll 1$  and  $L \gg L_c$  follows

$$w_s(t) \sim t^\beta \quad (2.30)$$

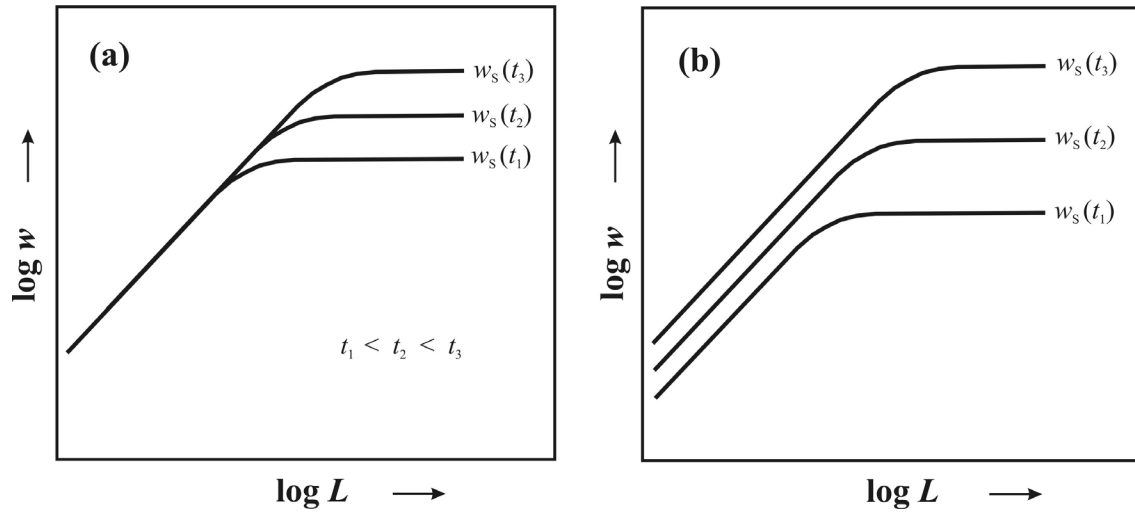


**Figure 2.6** Schematic illustration of (a): Equations (2.29) and (2.30) (normal scaling) and (b): Equations, (2.29') and (2.30') (anomalous scaling).

This behavior is illustrated schematically in Figure 2.6a. However, it has been shown that  $w(L, t)$  can exhibit more complex behavior characterized by the relationships [56]:

$$w(L, t) \sim L^H t^{\beta_{loc}} \quad \text{for } L \ll L_c \quad (2.29')$$

$$w_s(t) \sim t^{\beta + \beta_{loc}} \quad \text{for } L \gg L_c \quad (2.30')$$

where  $\beta_{loc}$  is a local growth exponent giving the time dependence of the small scale roughness. This scaling is illustrated schematically in Figure 2.6b and is called anomalous scaling.

**Table 2.2** Values of the scaling exponents  $H$  and  $\beta$  predicted by different theoretical models.

<b>Model</b>	<b>roughness scaling exponent <math>H</math></b>	<b>growth scaling exponent <math>\beta</math></b>	<b>Reference</b>
stochastic roughening	0	0.5	[57]
erosion and redeposition	0	0	[58]
Kardar, Parisi and Zhang model	0.4	0.25	[59]
surface diffusion	1	0.25	[60]
surface diffusion and step growth	0.67	0.2	[61, 62]

As can be seen from Equations, (2.29') and (2.30') the normal scaling given by Equations (2.29) and (2.30) can be considered as a special case of the anomalous scaling for  $\beta_{\text{loc}} = 0$ .

In order to predict the scaling exponents were developed various theoretical models describing the growth of the surfaces by competition between the stochastic roughening and different smoothening mechanisms involving processes such as erosion and redeposition, surface diffusion etc [54]. Values of scaling exponents  $H$  and  $\beta$  predicted by some theoretical models are given in Table 2.2.

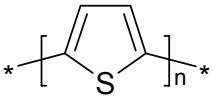
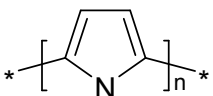
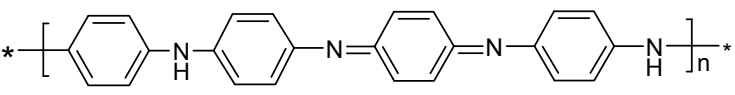
## **2.2 Conducting Polymers**

### **2.2.1. General aspects**

A new class of polymers, exhibiting the ability to be doped over the full range from insulator to metals, has been discovered about 30 years ago [63]. For this discovery A. J. Heeger, A. MacDiarmid and H. Shirakawa were awarded in 2000 with Nobel Prize in Chemistry [64-66].

The unique characteristic of the conducting polymers is that they have on one side the electrical and optical properties of metals and semiconductors and on the other the mechanical properties and the processing advantages of the organic polymers. Due to their interesting features these materials find nowadays various applications in the technology. [28,67-69]. Some examples for conducting polymers and their applications are listed in Table 2.3.

**Table 2.3** Applications of some conductive polymers and their derivatives

Conducting polymer	Application field
Polythiophene (PT) 	Electroluminescence Electrochemical capacitors Cathode material for battery Microlithography Corrosion inhibitor
Polypyrrol (PPy) 	Electrochromic displays Light weight battery Sensors Solar energy cells
Polyaniline (PANI) 	Electrochromic displays Photolithography Rechargeable battery Sensors and biosensors Corrosion inhibitor

Generally all conducting polymers are conjugated systems with one unpaired  $\pi$ - electron per carbon atom. Due to the Peirels distortion the  $\pi$ - band is split into occupied  $\pi$ - (valence) and unoccupied  $\pi^*$ -(conducting) bands and the energy difference between the HOMO ( $\pi$ -) and the LUMO ( $\pi^*$ -) levels represents the band gap. The width of the gap can be controlled via fuctionalization of the polymer backbone [69]. The overlap of the carbon  $p_z$ -orbitals leads to delocalization of the electrons along the polymer chain, exhibiting the possibility for charge mobility. In the case of PANI the  $p_z$ -orbitals of the nitrogen also contribute to the conjugation, which leads to different behaviour of PANI compared to polymers like PT or PPy.

The conjugated polymers can be p- or n- doped via chemical or electrochemical doping. The carriers induced by the doping are delocalized along the polymer chain giving rise of the charge mobility into three dimensions. Due to the reversibility of the doping process the electrical conductivity of these polymers can be switched over the full range from insulator to metal as shown in Figure 2.7. This switch between metallic and insulating state is related also to optical changes and makes the conducting polymers suitable for various technological applications.

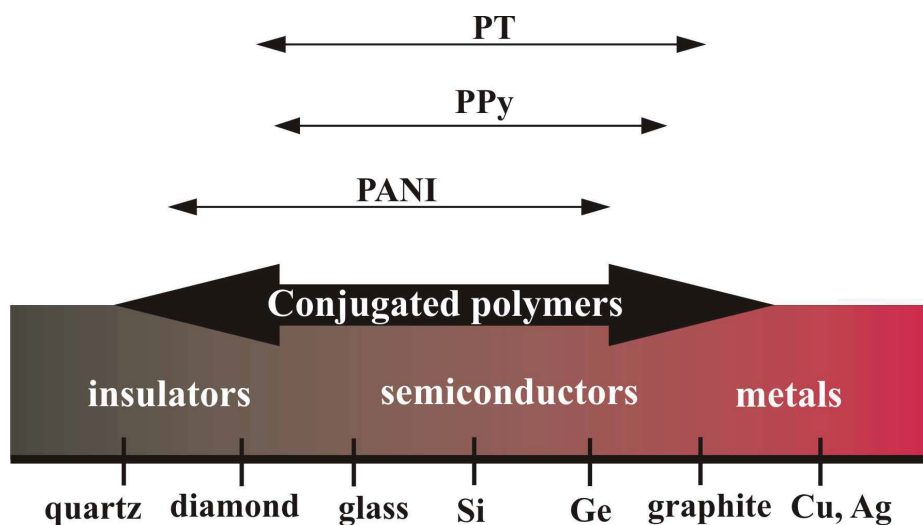


**Figure 2.7** Schematic presentation of the conductivity range of some conjugated polymers.

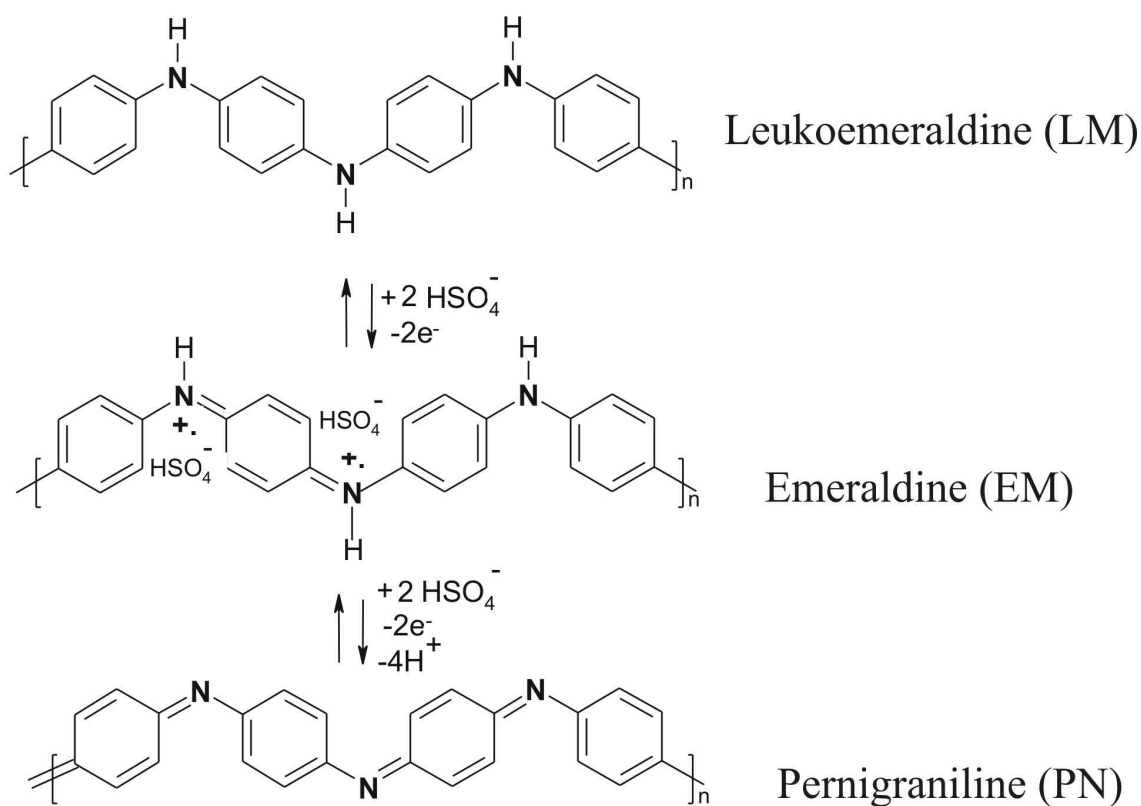


**Figure 2.8** Schematic presentation of the reversible redox transitions of PANI in acid media ( $\text{H}_2\text{SO}_4$ ).

According to the literature in acid media PANI is involved in two reversible redox processes, which can be controlled electrochemically (Figure 2.8) [70, 71]. At cathodic potential the

polymer is in its fully reduced Leukoemeraldine (LM) state, containing amine nitrogen atoms. In this form PANI exhibits characteristics of p-type semiconductor with very bright band gap and low conductivity. By partial oxidation occurs transition of the LM state into half oxidized Emeraldine form (EM), which can be drawn as polysemiquinone radical cation, consisting of separated and mobile conductive sites, known as polarons [72]. In order to balance the formed positive charges, counter anions from the solution intercalate into the polymer matrix. This process is observed as an electrochemical doping and PANI exhibits high electric conductivity in the EM form. The EM state can be further electrochemically converted into the fully oxidized Pernigraniline state (PN) accompanied by deprotonation of the amine nitrogens and expulsion of the counter inions. Due to the oxidation reaction the PN form contains imine nitrogen atoms and has low conductivity. The reversible transition between the different redox states of PANI can be illustrated adequately using cyclic voltammetry, as shown later in this work.

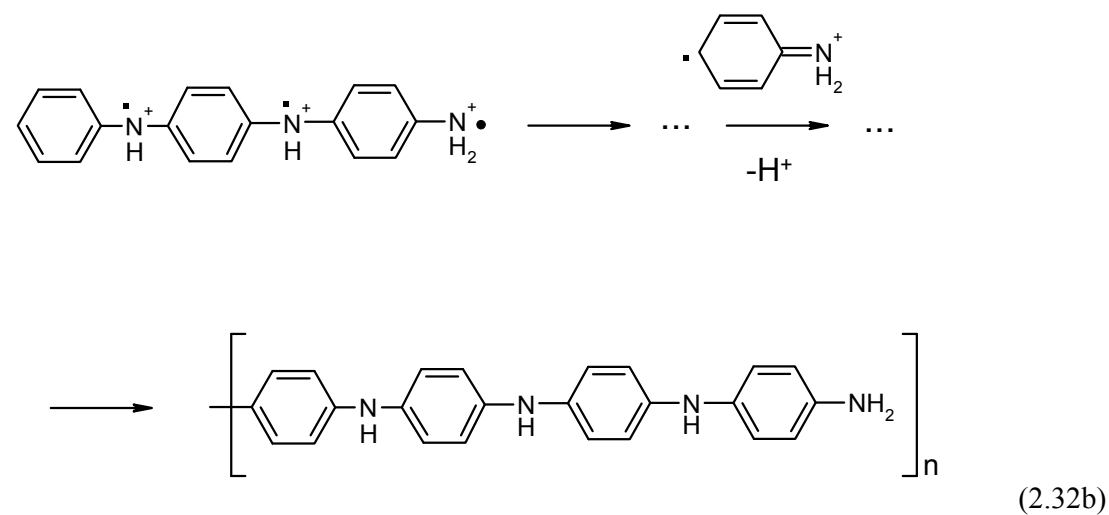
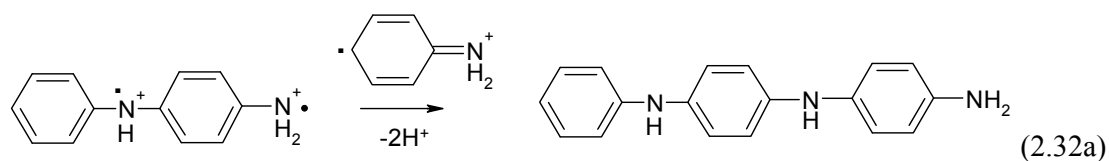
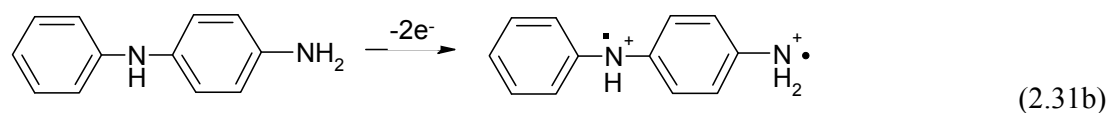
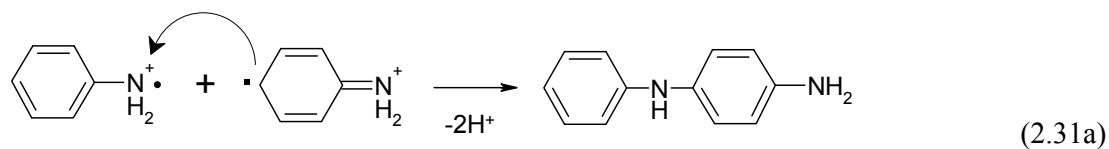
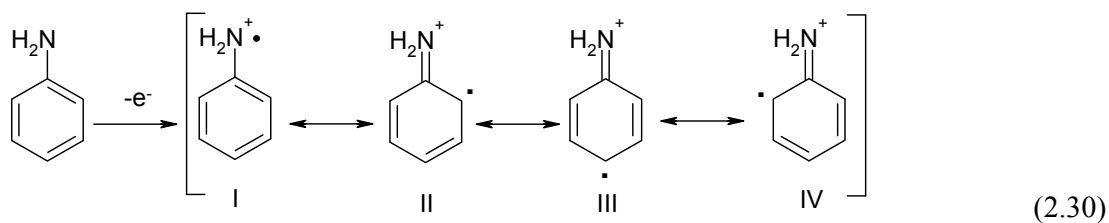
### 2.2.2 Electrochemical polymerization of polyaniline

Various routines such as typical organic procedures or electrochemical techniques are applied nowadays to synthesize conductive polymers [69]. One of the most widely studied conductive polymers is polyaniline (PANI), which can be synthesized from monomer containing solution either chemically (using oxidizing agents) or electrochemically applying different polarization routines.

No matter whether PANI is synthesized chemically or electrochemically, it is generally admitted that the initial stage of the polymerization starts with the formation of radical cation by oxidation of the monomer aniline and is the rate determining step [71]. Due to the electronic effects induced in the benzene ring by the *o*- and *p*- orientating amino (-NH<sub>2</sub>) group, the oxidized aniline species has several resonant forms (I, II, III, IV), which can be expressed by (2.30).

The second stage of the aniline electropolymerization corresponds most probably to the formation of *p*-aminodiphenylamine by interaction of the cation radical I and the resonant form III, where steric interactions are avoided (2.31a)





In the following step the formed dimer also undergoes an oxidation till dimer cation (cf. 2.32b). At least two possible scenarios for the further formation of the polymer chain have been discussed in the literature. According to Moilner et al. [73] the dimer cation reacts with another dimer to a tetramer, which undergoes an oxidation and binds with another oxidized tetramer to form an octameric chain. In a second scenario the dimer cation is reacting first

with an activated monomer according to (2.32a) [71, 74]. The further polymerization proceeds by similar head-tail reactions of the cation radical monomer and the oxidized end of the polymer chain (2.32b).

Although the interaction between the oxidized aniline and the chain end seems to be the most favourable, a branching occurs by attachment of the cation radical monomer to other sites of the polymer chain. This branching is responsible for the formation of 2D or 3D microscopic polymer structures discussed in the following section.

### **2.2.3 The concepts of nucleation and growth in electropolymerization**

The investigations on electrochemical formation of conductive polymer layers are strongly influenced by the well known concepts of “electrochemical nucleation and growth” originating from the numerous and detailed studies in the field of metal electrodeposition [2-8]. Potentiostatic current transients obtained in the course of anodic polymerization are readily interpreted by using theoretical equations derived for the metal nucleation and growth case, paying little attention to some specific features of the electropolymerization process. Limitations to the use of available “nucleation and growth” models for the electropolymerization case are rarely discussed [32,34]. However, as already mentioned according to the theory of first order phase transitions the nucleation is the process of formation of supercritical clusters of the new phase able to grow irreversibly up to macroscopic dimensions via addition of monomeric species. In the case of electropolymerization the “nucleation” stage is rather complicated because of several reasons [34]. The main point relates to the difficulty in defining how and where the critical nuclei appear. There could be at least two different ways for the formation of irreversibly growing polymer clusters on the electrode surface – growth of oxidized monomers adhering to the electrode surface through successive addition of monomers (or oligomers) from the solution or alternatively precipitation of larger oligomeric species previously formed in the solution.

Another important point is the dimensionality of the newly formed polymer phase. Generally the electropolymerization occurs exclusively in one dimension and results in the formation of linear chains (1D phase formation). According to the classical theory, a first order phase transition is absent in the case of 1D phase formation [34,39,75]. This means that in the particular case of formation of linear polymer chains the concept of critical nucleus formation

has no physical meaning and the single oxidised monomer adhering to the electrode surface is able to grow irreversibly to macroscopic dimensions (cf. section 2.1.1).

The “nucleation and growth” models developed for the case of metal electrodeposition discussed in this work previously (section 2.1.2) involve assumptions concerning the nucleation kinetics and the growth geometry without referring to the origin of the stable clusters. Thus, the electrochemical “nucleation and growth” models are in fact phenomenological growth models and the term nucleation staying for the appearance of stable growing clusters but not necessarily for nucleation in the thermodynamic sense addressed above. This justifies the use of such phenomenological models for the electropolymerization, bearing in mind that “nucleation” in this case is the appearance of irreversibly growing polymer structures and not formation of critical nuclei according to the classical first order phase transition theory.

As for the growth stage, growth in the metal electrodeposition case is allowed either in 2 or in 3 dimensions, assuming a constant growth rate irrespective of the size of the growing cluster. In contrast, growth in the polymer case is very specific - although individual segments of the polymer structure grow through one dimensional chains, the microscopic picture of polymer layer formation corresponds to formation of 2D or 3D polymer structures, consisting of numerous chains with various extent of ordering, structural specifics (e.g. branching) and possible interchain interactions. Due to these specific factors the microscopic growth of the polymer structures, resulting from the simultaneous growth of multiple chains, may occur preferentially in 2 or 3 dimensions and it is reasonable to apply the formal models for 2D or 3D growth. Nevertheless, bearing in mind the variety of factors influencing the formation of the microscopic polymer structure, the assumption for a constant (size independent) growth rate seems not to be very realistic and the growth models should be applied only in a relatively narrow time range in the very initial stages of electropolymerization.

## **2.3 Metal Nanocontacts and Nanogaps**

This section begins with a brief review of the experimental approaches, used nowadays for fabrication of nanostructures for studies of the fundamental aspects of electron transport in nanoscale contacts and single molecules. The second subsection provides a theoretical basis to

discuss the experimental results obtained in this work during the studies on preparation of nanoscale gaps and metal point contacts by gold electrodeposition.

### **2.3.1 Preparation and application of nanogaps**

A major challenge on the way of further miniaturisation of electronic components is the fabrication of nanoscale building blocks, assembling of the blocks into devices and measuring the fundamental electron transport properties of the devices. On the nanoscale occur novel physical, chemical, electrical and electrochemical phenomena, which may lead to new operations modes and applications. Several experimental techniques, such as scanning tunnelling microscopy (STM), atomic force microscopy (AFM) and mechanical break junction have been applied in order to form nanostructures and to study the fundamental electron transport in nanoscale contacts and single molecules [12,76-82]. These techniques however, are not compatible with device application. Therefore, recently big attention has been paid to the fabrication of individually addressed electrode pairs with molecular scale gaps combining conventional lithographic techniques with electromigration [83] or electrochemical metal deposition and dissolution [84].

The electrochemical techniques are suitable for commercial applications and offer unique advantages toward the other methods. First, nanostructures can be re-fabricated until the most desirable structure is created using electrochemical metal deposition and dissolution, due to the reversibility of these processes. Second, the deposition rate and the morphology can be easily controlled by the applied electrode potential or current density. The nanogap width can be precisely monitored via different feedback signals such as tunnelling current [85,86], ac-impedance [87,88] or potential drop in the electrochemical double layer [89]. Nanogaps in the range from 1 nm to more than 100 nm have been prepared by narrowing the original microscopic spacing between lithographically formed electrode pairs using electrochemical deposition of various metals [85-91]. Figure 2.9 shows schematically different nanogap applications. The nanogaps can be transformed into nanoscale contacts by further electrodeposition. Such nanocontacts have potential application in single atom memory devices, chemical sensors and biosensors due to their unique properties, which differ significantly from those of the bulk materials. Li et. al. [92] studied the influence of molecular adsorption on stable metallic nanocontacts, prepared by electrochemical deposition of copper on gold electrodes, separated by 100 nm gap. They showed that the observed dependence of

the quantized conductance of the wire upon adsorption of molecules may be used for chemical sensor applications.

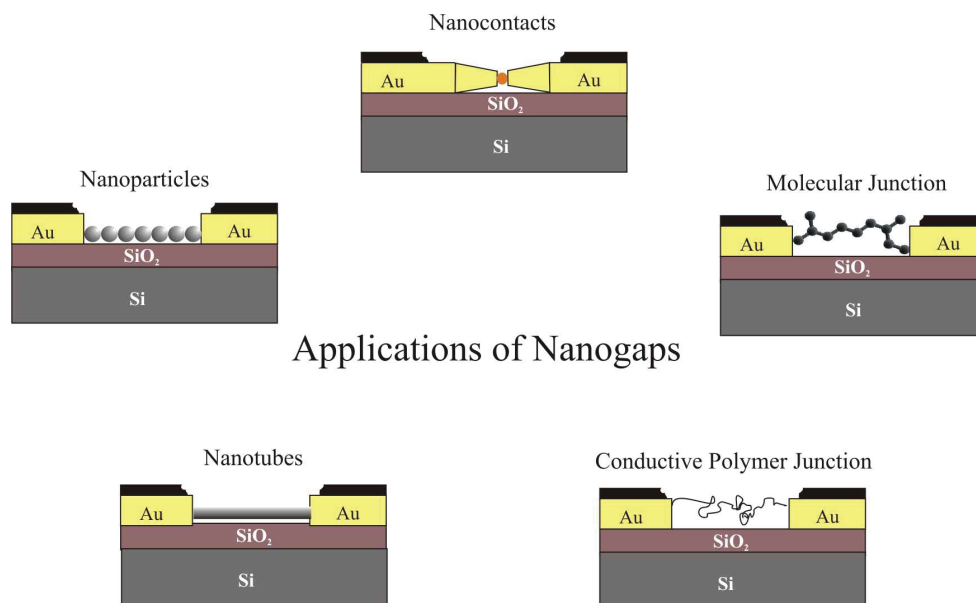


**Figure 2.9** Schematic presentation of possible applications of individually addressed electrode pairs separated by nanoscale gaps.

Individually addressed electrode pairs separated by molecular scale gaps can be bridged by carbon nanotubes [93], conductive polymers [25] and even single molecules [94]. Such nanobridges can be used for fundamental studies in order to understand in detail their electrical and electrochemical characteristics.

### 2.3.2 Conductance quantization and quantum tunnelling

According to the Ohm's law the conductance ( $G$ ) on the microscopic scale of a given sample with conductivity ( $\sigma$ ) is proportional to its cross sectional area ( $S$ ) and inversely proportional to its length ( $l$ ):

$$G = \sigma S / l \quad (2.34)$$

If the size of a contact between two metal pieces is much larger than the mean free path of electrons, the electron transport is described by the classical diffusive scattering. When the diameter of the contact is in the same order like the electron wavelength, the electron

transport becomes ballistic and the conductance exhibits quantum behaviour, which can not be described by the Ohm's law (Equation (2.34)). This quantum behaviour leads to a stepwise increase or decrease of the conductance during the formation or destruction of nanocontacts and has been demonstrated for various metals [81,85-90].

The conductance of nanoscale contacts is described by the Landauer formula [95]:

$$G = \frac{2e^2}{h} \sum_{i=1}^N T_i \quad (2.35)$$

where  $e$  is the electron charge,  $h$  is the Planck's constant,  $N$  is the number of conducting channels ( $N=1,2,3,\dots$ ) and  $T_i$  represents the transmission probability of each mode. The transmission probability depends on the chemical valence of the metal. In the case of alkali metals and for many monovalent transition metals,  $T_i$  is close to 1 and Equation (2.35) can be expressed as following:

$$G = NG_0 \quad (2.36)$$

Here  $G_0 = \frac{2e^2}{h}$  represents the conductance quantum, so that the conductance is quantized.

For other metals  $T_i$  may deviate significantly from 1 and each quantum step in this case could not be exactly  $1G_0$  [92].

Quantum tunnelling occurs if a voltage bias is applied between two electrodes separated with a small nanoscale gap. The resulting tunnelling current  $I_t$  decays exponentially with the gap width  $s$  and can be expressed by the following relation [96, 97]:

$$I_t(s) = I_t(0) \exp(-ks) \quad (2.37)$$

where the decay constant  $k$  depends on the effective tunnel barrier height. This sensitive dependence of the tunnelling current on the distance between the electrodes has been applied for monitoring and precise control of the nanogap width during the electrochemical narrowing [85].

### 3. Experimental

#### 3.1 Electrolytes and Chemicals

The following cyanide-free aqueous electrolytes were used in the experiments on gold electrodeposition:

(I) 1mM KAuCl<sub>4</sub> + 0.1M HClO<sub>4</sub> (pH=1)

(II) 5mM HAuCl<sub>4</sub> + 42mM Na<sub>2</sub>S<sub>2</sub>O<sub>3</sub> + 42mM Na<sub>2</sub>SO<sub>3</sub> (pH≈7.5)

In both electrolytes (I) and (II) the gold exists not as a free cation, but in the form of complex ions [AuCl<sub>4</sub>]<sup>-</sup> and [Au(S<sub>2</sub>O<sub>3</sub>)(SO<sub>3</sub>)<sub>2</sub>]<sup>5-</sup>. Recent studies show that the gold thiosulphate - sulphite mixtures can be successfully applied in the microelectronics for gold electroplating, due to its good compatibility with the resist layers, used in the lithography [98, 99]. The electrolyte (II) has been prepared according to the routine described by Roy et al. [100] by slowly adding an aqueous solution of chlorauric acid (HAuCl<sub>4</sub>) to a solution containing Na<sub>2</sub>S<sub>2</sub>O<sub>3</sub> and Na<sub>2</sub>SO<sub>3</sub>. Under these conditions the tetrachloraurate complex [AuCl<sub>4</sub>]<sup>-</sup> undergoes homogeneous reduction and ligand exchange leading mainly to formation of the gold thiosulphate complex ions [Au(S<sub>2</sub>O<sub>3</sub>)(SO<sub>3</sub>)<sub>2</sub>]<sup>5-</sup> [101]. It is very important to monitor the pH during the formation of the [Au(S<sub>2</sub>O<sub>3</sub>)(SO<sub>3</sub>)<sub>2</sub>]<sup>5-</sup> ions because at pH<6 the S<sub>2</sub>O<sub>3</sub><sup>2-</sup> ions disproportionate and brownish precipitate appears in the transparent solution. Therefore, during the preparation of the electrolyte solution the pH has been kept in the range from 7.5 to 8 via adding portions of 10% KOH when necessary.

The electrodeposition of polyaniline was performed in freshly prepared aqueous electrolyte solution containing 0.1M Aniline + 0.5M H<sub>2</sub>SO<sub>4</sub>.

Additional modification and electrochemical characterization of nanoscale gold and polyaniline electrodeposits have been performed in the following solutions:

0.1M H<sub>2</sub>SO<sub>4</sub>  
 0.5M H<sub>2</sub>SO<sub>4</sub>  
 1mM CuSO<sub>4</sub> + 0.1M H<sub>2</sub>SO<sub>4</sub>  
 1mM K<sub>2</sub>PtCl<sub>4</sub> + 0.05M H<sub>2</sub>SO<sub>4</sub>  
 0.5M H<sub>2</sub>SO<sub>4</sub> + 1M CH<sub>3</sub>OH

All electrolyte solutions have been prepared from chemicals with the most possible purity grade and Millipore<sup>®</sup> water. The used chemicals are listed in table 3.1.

**Table 3.1** Chemicals used in the present work

Chemicals	Company	Purity grade
KAuCl <sub>4</sub>	Aldrich	99.995 %
HAuCl <sub>4</sub> . 3H <sub>2</sub> O	Aldrich	99.9+%
H <sub>2</sub> PtCl <sub>4</sub>	Aldrich	99.99%
H <sub>2</sub> PtCl <sub>6</sub> . H <sub>2</sub> O	Aldrich	99.9+%
CuSO <sub>4</sub>	Fluka	99.0%
C <sub>6</sub> H <sub>5</sub> NH <sub>2</sub> (aniline)	Merck	f.s.
Na <sub>2</sub> SO <sub>3</sub>	Merck	99.0%
Na <sub>2</sub> S <sub>2</sub> O <sub>3</sub> . 5H <sub>2</sub> O	Merck	99.5%
96 % H <sub>2</sub> SO <sub>4</sub>	Merck	s.p.
70 % HClO <sub>4</sub>	Merck	s.p.
32% HCl	Merck	s.p.
65% HNO <sub>3</sub>	Merck	s.p.
KOH	Merck	99.0%
40% HF	Merck	p.a.
NH <sub>4</sub> F	Riedel-de Haen	p.a.
<i>i</i> -propanol	KMF Laborchemie Handels	p.a.
Methanol	KMF Laborchemie Handels	p.a.
Acetone	KMF Laborchemie Handels	p.a.
Ethanol	KMF Laborchemie Handels	p.a.



### 3.2. Electrode Substrates

Glassy carbon (GC), p-Si(111), Au(111) and lithographically prepared silicon based chips, containing gold electrode pairs have been used as substrates in the present work.

The GC substrates with a size 6mm×6mm (HTW, Germany) have been mechanically polished with diamond paste (up to 0.3  $\mu\text{m}$ ) to achieve mirror like surface. After the mechanical polishing the GC substrates were subsequently cleaned ultrasonically for 10min in ethanol and 10 min in Millipore<sup>®</sup> water.

The silicon substrates (6.5mm×6.5mm) were cut from p-Si(111) wafers (boron doped,  $10^{16} \text{ cm}^{-3}$ ) and then subsequently cleaned ultrasonically for 15 min in *i*-propanol, methanol, acetone and water. Before each electrochemical experiment the p-Si(111) substrates have been subsequently etched for 20 s in 1% HF solution to remove the native oxide and for 4 min in 40%  $\text{NH}_4\text{F}$  under nitrogen atmosphere in order to obtain a H-terminated silicon surface.

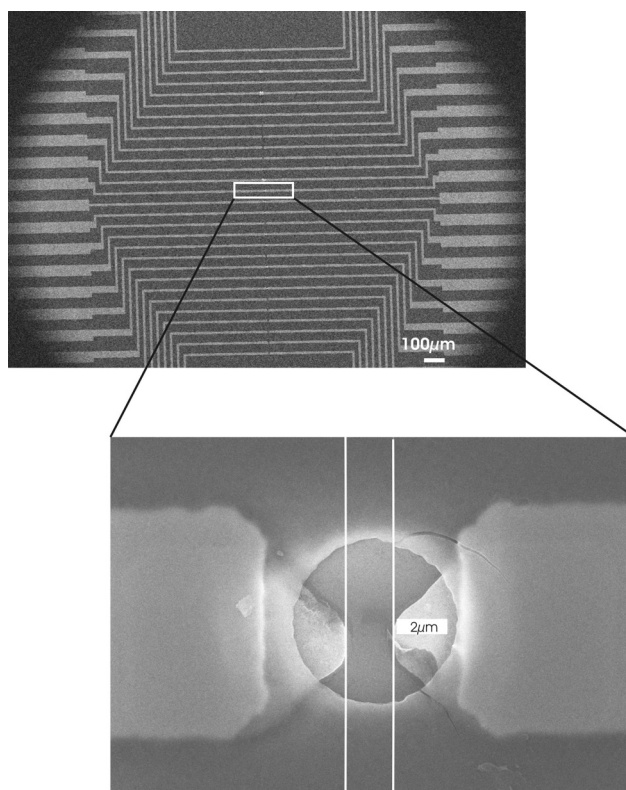


**Figure 3.1** SEM images of silicon chip, containing 29 opposite gold electrode pairs separated by 2 $\mu\text{m}$  distance.

The Au(111) substrates in form of single crystal discs (11mm in diameter) have been polished and flame annealed before each experiment.

Silicon based chips containing 29 gold microelectrode pairs (with microelectrodes separated by a 2 $\mu$ m gap) have been prepared in the clean room of IBN2 (Forschungszentrum Jülich GmbH) by conventional optical lithography (Figure 3.1). A silicon wafer, with surface layer of silicon dioxide has been used as substrate to fabricate the structures. The resist layer of PMMA (poly-methyl-methacrylate) exhibits hydrophobic properties. Therefore, before each electrochemical experiment the chips have been ultrasonically treated in presence of a droplet of the working solution on the surface in order to guarantee a complete wetting contact between the microelectrodes and the aqueous electrolyte [86].

### 3.3. Substrate Holders

The holder for GC and p-Si(111) substrates is shown in Figure 3.2. The active electrode area of the substrate is defined by a 4 mm opening in the Teflon holder 1. A copper plate 2 and brass screw 3 press the substrate from the back side in order to avoid penetration of the electrolyte. In the case of p-Si(111) an Ohmic contact has been established at the back side of the substrate by Ga-In alloy (Merck). The holder is closed by a Teflon screw 4 and a viton ring 5 to prevent entry of the electrolyte in the holder. To establish an electric contact with the sample a copper bar 6 (placed in a Teflon tube 7) is pressed to the messing screw 3 through an entrance on the left side of the sample holder.



**Figure 3.2** Teflon sample holder for GC and p-Si(111) substrates.

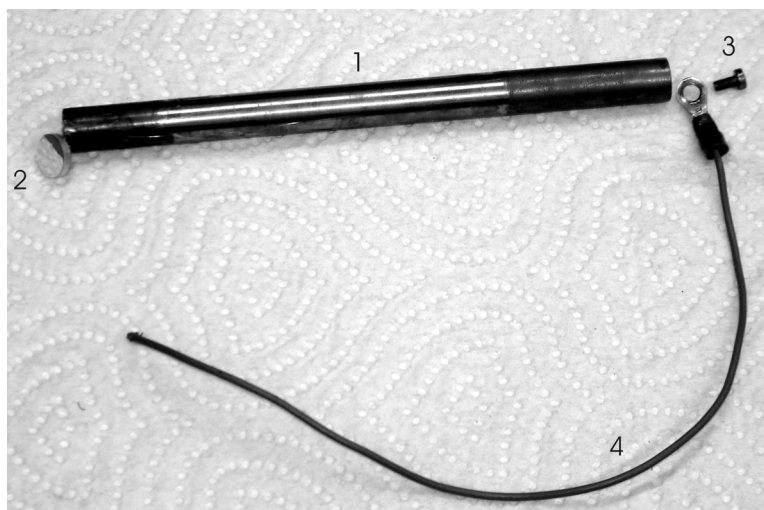


**Figure 3.3** Brass sample holder for Au(111) substrates.

The holder for Au(111) substrates is shown in Figure 3.3. A cylindrical brass bar (11mm in diameter) acts as a sample holder in this case. The gold single crystal disc 2 is attached and fixed on the one side of the brass cylinder using conducting silver paste. The electric contact with the sample is made on the other side of the brass holder. After mounting the Au(111) substrate, the holder has been positioned in the electrochemical cell using a quickfit. The so-called dipping technique has been applied in order to contact the Au(111) face of the substrate and the solution.

### 3.4 Electrochemical Cells and Instrumentation

#### 3.4.1 Electrochemical experiments on GC, p-Si(111) and Au(111) macroelectrodes

The measurements have been performed at room temperature (21°C) in a conventional three electrode cell, containing the working electrode, a platinum plate as a counter electrode and a saturated mercury sulfate electrode (MSE) or saturated calomel electrode (SCE) as reference electrodes (Figure 3.4). The reference electrode has been positioned in a Lugging capillary in order to reduce the distance to the working electrode. The electrochemical cell has been equipped with nitrogen input and outlet so that prior and during each measurement the cell was deaerated with pure nitrogen. All potentials in the present work are referred to the standard hydrogen electrode (SHE).

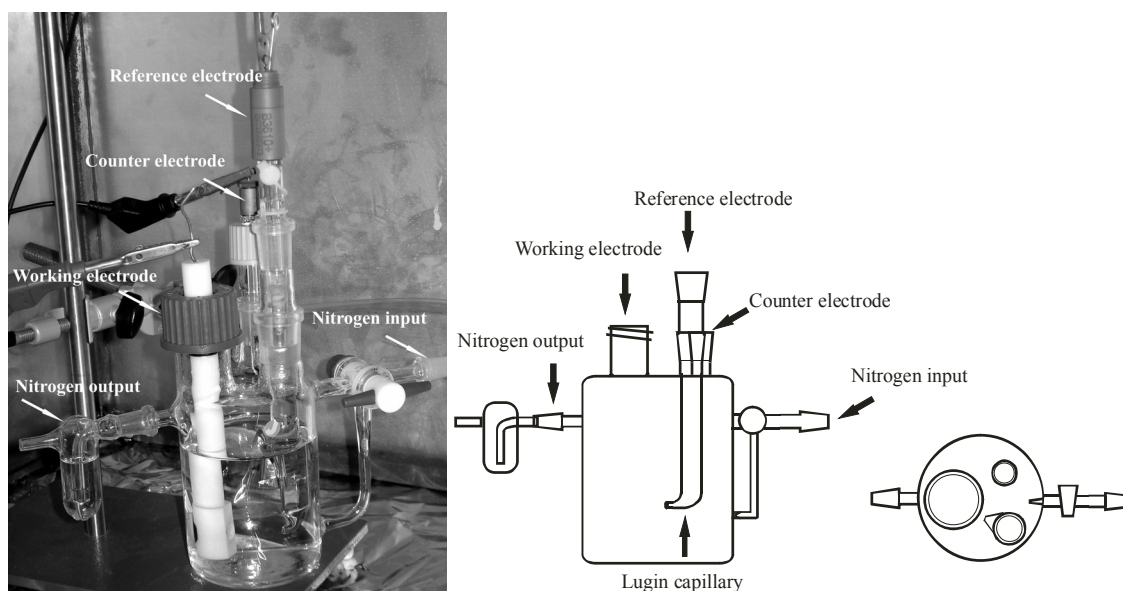


**Figure 3.4** Photograph and schematic presentation of three-electrode electrochemical cell, used for the experiments on GC, p-Si(111) and Au(111) macroelectrodes.



**Figure 3.5** AFM microscope, equipped with antivibration table and noise isolation chamber.

To avoid external disturbances the measurements have been performed in a homemade Faraday cage. Some measurements on p-Si(111) have been carried out under illumination using a fiber optic quartz halogen illuminator, providing a fairly uniform beam of visible light (emission spectrum distributed between 500 and 1500 nm) with an intensity of 70,000 lx. The

electrochemical cells and all glass and Teflon accessories have been soaked for at least two hours in hot 65% HNO<sub>3</sub> + 95% H<sub>2</sub>SO<sub>4</sub> mixture and after that rinsed and boiled in Millipore® water.

Electrochemical measurement techniques such as cyclic voltammetry, chronoamperometry and electrochemical impedance spectroscopy have been applied using computer controlled potentiostat/galvanostat Autolab PGSTAT30 (Eco Chemie, Netherlands) and impedance spectrum analyzer IM5d (Zahner Elektrik, Germany).

The morphology of electrodeposits has been characterized by scanning electron microscopy (SEM) using a Leo1550 SEM equipment with electron beam energies ranging between 2keV and 20 keV. All presented SEM measurements have been performed by Hans-Peter Boehm (IBN, FZ-Jülich). In some cases ex-situ atomic force microscopy (AFM) has been also applied to study the surface topography of electrodeposits. A commercial scanning probe microscope (Molecular Imaging, Tempe, Arizona, USA) combined with a Nanoscope E controller (Digital Instruments Inc., Santa Barbara, California, USA) have been used for these studies. Triangular Ti-Pt coated cantilevers (CSC11, Micro Mash, USA) with 30 kHz free response frequency and 0.35 N/m spring constant were used for the AFM imaging. Antivibration table and home made acoustic noise isolation chamber have been used in order to achieve better imaging (Figure 3.5).

### **3.4.2 Electrochemical low current measurements on microelectrode gold pairs**

The experiments on gold microelectrode pairs have been performed using a homemade four electrode bipotentiostat developed by Dr. Gábor Mészáros and Dr. Thomas Wandlowski (IBN3, Forschungszentrum Jülich) [102]. A simplified scheme of the bipotentiostat is shown in Figure 3.6. The current measuring unit of the bipotentiostat measures separately the currents of the two working microelectrodes, while the potential controlling unit provides two signals. The first signal represents the potential of the working electrode 1 with respect to a reference electrode. The second signal corresponds to the potential difference between the two working electrodes. Both signals can be customized by digital (stepwise) time functions. An alternative linear sweep generator is also implemented

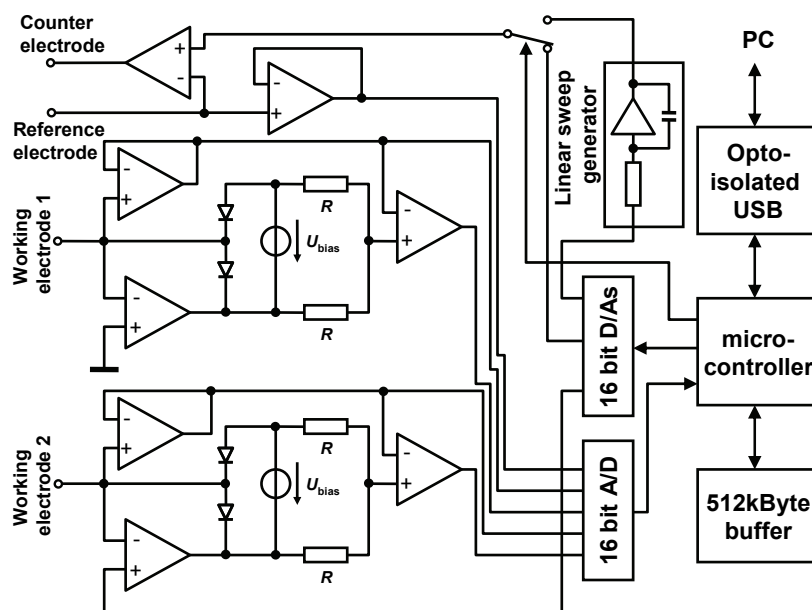


**Figure 3.6** Simplified scheme of bipotentiostat for low current measurements [102].

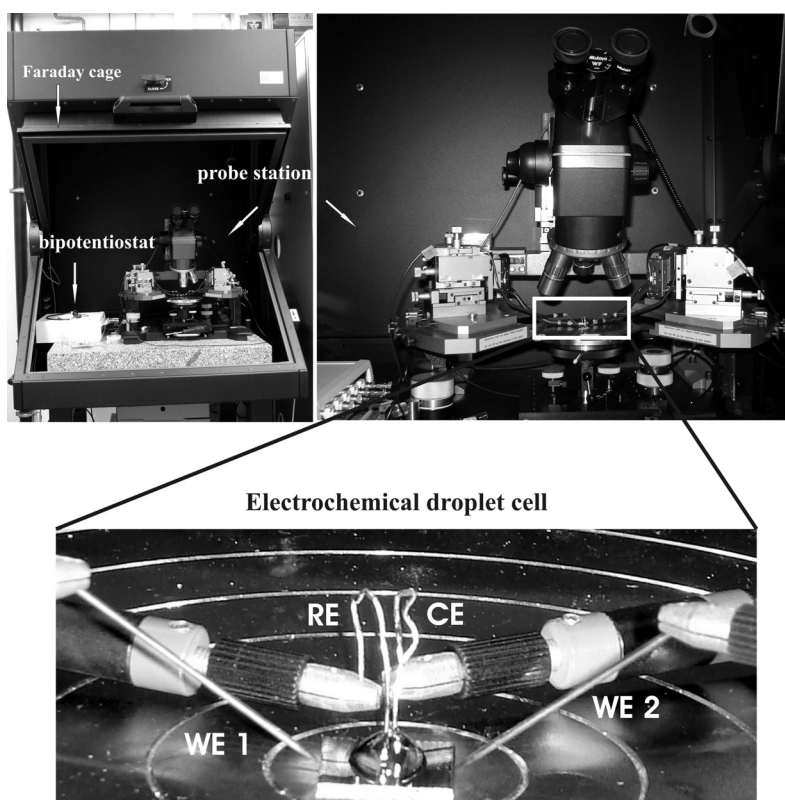


**Figure 3.7** Experimental setup for electrochemical measurements on lithographical chips, consisting of Faraday cage, commercial probe station and home made bipotentiostat.

The microcontroller controls the measurements with the help of 16 bit D/A converters and an 8 channel 16 bit A/D converter. The user interface and the visualization of the recorded data are implemented on the basis of an in-house developed Windows® program. The microcontroller communicates via a galvanically isolated USB interface to a PC [102].

On Figure 3.7 is presented the complete setup used for the electrochemical measurements on the chips containing gold microelectrode pairs. The bipotentiostat and the Süss Probe Station 335 PM-V1 (Süss MicroTec AG, Germany) are placed in a grounded Faraday cage. In this case the electrochemical cell represents a droplet cell and contains four electrodes. The working electrodes (WE1 and WE2) can be connected to the bipotentiostat via needles using the optical microscope and micromanipulators. Flame annealed gold wires serve as counter (CE) and reference (RE) electrodes during the gold deposition. Thus the potentials in the case of gold electrodeposition on the microelectrodes refer to the Nernst equilibrium potential of gold in the corresponding electrolyte. In the case of electrodeposition of polyaniline flame annealed platinum wires have been used as CE and RE and the given potentials are also referred to the Standard Hydrogen Electrode (SHE).

## 4. Experimental Results and Discussion

### 4.1 Modification of Glassy Carbon by Electrodeposition of Au Nanoparticles

#### 4.1.1 Electrochemical nucleation and growth of Au nanoparticles

The nucleation and growth phenomena involved in the initial stages of gold electrodeposition on GC substrates were investigated by cyclic voltammetry, potentiostatic transient measurements and SEM observations. The cyclic voltammogram in Figure 4.1 shows the electrochemical behaviour during Au electrodeposition in the system GC/1mM KAuCl<sub>4</sub> + 0.1M HClO<sub>4</sub>. In this system the active gold species in the electrolyte solution are the [AuCl<sub>4</sub>]<sup>-</sup> complex ions and the overall deposition reaction can be expressed by



The absence of cathodic current at potentials more positive than 1V in the initial cathodic scan of the cyclic voltammogram in Figure 4.1 shows that an Au UPD does not occur in this system and the deposition process follows the so-called Volmer-Weber mechanism. The sharp increase of the cathodic current observed at potentials more negative than 1V indicates the onset of nucleation of the gold 3D bulk phase. The following cathodic current peak at about 0.92V shows that the deposition process becomes diffusion controlled. The diffusion control is reflected also in the limiting diffusion current observed during the reversed anodic scan. This behaviour is in agreement with that reported previously for gold electrodeposition on HOPG and GC from similar electrolytes containing [AuCl<sub>4</sub>]<sup>-</sup> complex ions [22, 103].

The cathodic current observed during the reversed anodic scan at electrode potentials more positive than 1V indicates that the apparent equilibrium potential of gold in this system is



more positive than the standard Nernst potential  $E_{3\text{DAu}}^0 = 1.01 \text{ V}$  corresponding to the reaction (4.1) [104].

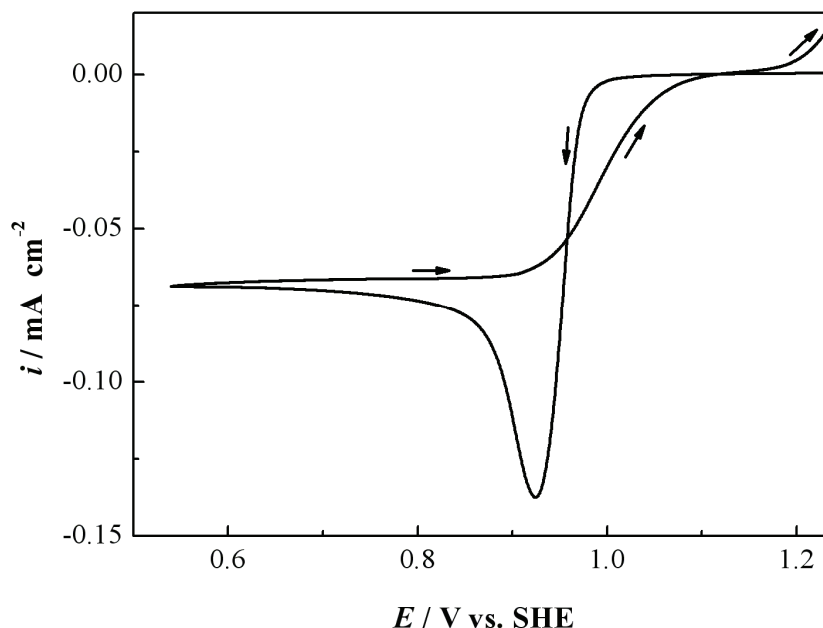


**Figure 4.1** Cyclic voltammogram recorded in the system GC/1mM KAuCl<sub>4</sub> + 0.1M HClO<sub>4</sub>. The potential scan is initiated at  $E = 1.24 \text{ V}$  in the cathodic direction with a scan rate  $|dE/dt| = 1 \text{ mV s}^{-1}$ .

Obviously in the investigated system the equilibrium is more complex and the overall deposition reaction (4.1) involves some intermediate steps. According to Anderson and Sawtelle [105] the mechanism of gold electrodeposition from electrolytes containing  $[\text{AuCl}_4]^-$  complex and low concentration of free  $\text{Cl}^-$  ions can be described by:



The proposed mechanism consists of two successive charge transfer steps (4.3) and (4.4) coupled with the preceding chemical reaction (4.2) and could be assigned to the investigated system GC/1mM KAuCl<sub>4</sub> + 0.1M HClO<sub>4</sub>.

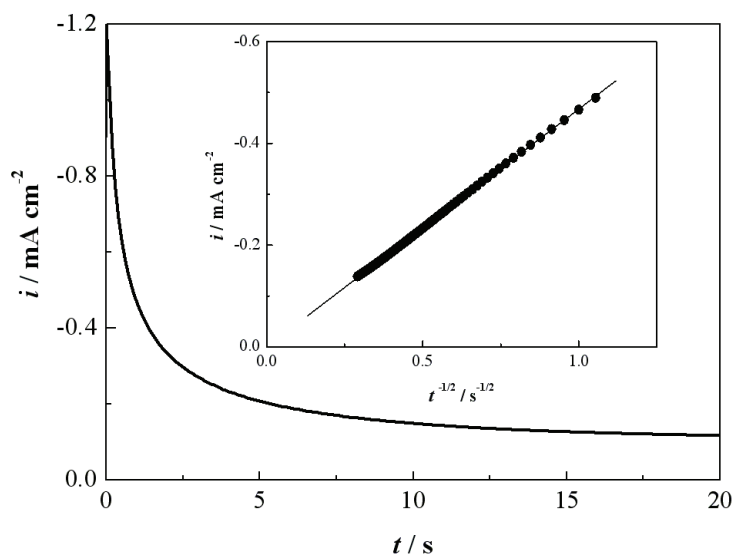
The diffusion coefficient  $D$  of  $[\text{AuCl}_4]^-$  ions can be estimated roughly from the observed limiting current density  $i_{\text{lim}}$  using the relation

$$|i_{\text{lim}}| = zFD \frac{c}{\delta_N} \quad (4.5)$$

where  $\delta_N$  is the thickness of the Nernst diffusion layer. Assuming that  $\delta_N$  is approximately 0.025 cm, one obtains a value of  $D = 6.4 \times 10^{-6} \text{ cm}^2 \text{ s}^{-1}$ , which is in agreement with the values reported previously [22, 103]. A better way for estimation of  $D$  is to analyse the potentiostatic current transients measured at sufficiently high cathodic potentials. The transient measurements show that at  $E < 0.6 \text{ V}$  the current transients follow the so-called Cottrell relation [106]

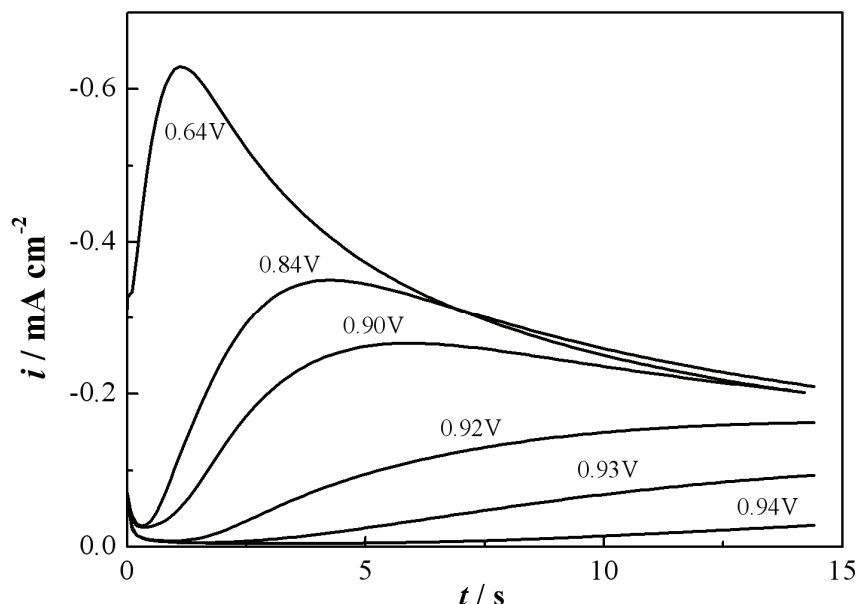
$$i = zFc(D/\pi)^{1/2} t^{-1/2} \quad (4.6)$$

Figure 4.2 shows a current transient measured at  $E = 0.54 \text{ V}$ . From the slope of the obtained linear  $i - t^{-1/2}$  dependence (shown in the inset of Figure 4.2) and Equation (4.6) was estimated a diffusion coefficient value of  $D = 1.1 \times 10^{-5} \text{ cm}^2 \text{ s}^{-1}$ , which is close to the value obtained from Equation (4.5).



**Figure 4.2** Potentiostatic current transient at  $E = 0.54 \text{ V}$  during gold electrodeposition in the system GC/1mM  $\text{KAuCl}_4 + 0.1\text{M HClO}_4$  (Inset:  $i$  vs.  $t^{-1/2}$  plot of the transient).

The potentiostatic transient measurements have been used also for investigation of the nucleation and growth phenomena in the initial stages of gold deposition. Figure 4.3 shows current transients obtained at different electrode potentials in the range  $0.64\text{ V} < E < 0.94\text{ V}$ . The transients exhibit the characteristic behaviour of a process involving nucleation and 3D diffusion-controlled growth (cf. Figure 2.5) [49]. After an initial decay related to adsorption processes, the current increases due to nucleation and growth of gold nanoparticles. The current maximum observed at high cathodic potentials results from the overlap of the growing particles and/or their diffusion zones.



**Figure 4.3** Potentiostatic current transient for deposition of gold at different electrode potentials in the system GC/1mM KAuCl<sub>4</sub> + 0.1M HClO<sub>4</sub>.

In Figure 4.4 the current transients obtained at 0.84V and 0.64V are represented in nondimensional  $(i/i_{\max})^2$  vs.  $(t/t_{\max})$  plots. For comparison are shown also the theoretical curves corresponding to the models involving progressive and instantaneous nucleation (cf. Equations (2.21) and (2.22) and Figure 2.5). It is clearly seen, that the current transient obtained at 0.84V corresponds to the model involving progressive nucleation, whereas the transient at 0.64V fits well with the theoretical curve for instantaneous nucleation.

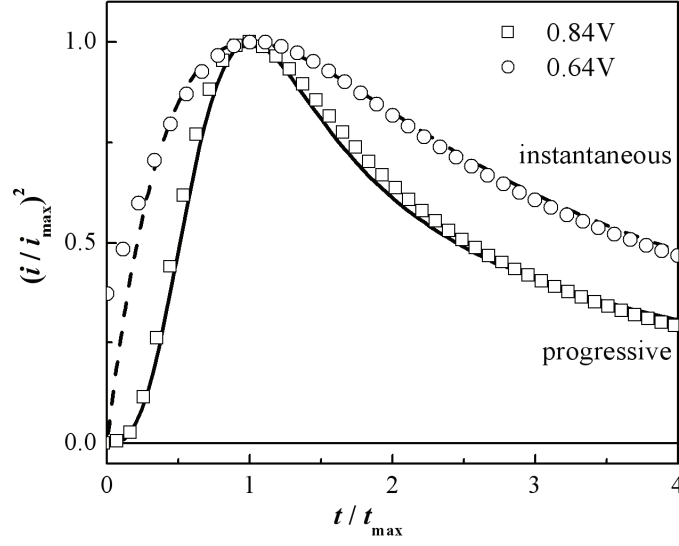


**Figure 4.4** Nondimensional  $(i/i_{\max})^2$  vs.  $(t/t_{\max})$  plots of potentiostatic current transients for deposition of gold at 0.84V ( $\square$ ) and 0.64V ( $\circ$ ) in the system GC/1mM  $\text{KAuCl}_4$  + 0.1M  $\text{HClO}_4$  compared to the theoretical curves corresponding to the models of progressive nucleation (solid line) and instantaneous nucleation (dashed line).

In the case of progressive nucleation the nucleation rate  $J$  can be extracted from the coordinates of the current maximum (cf. Equation (2.24)) using the relation:

$$J = 0.2898 (8\pi V_m c)^{-1/2} \frac{(zFc)^2}{i_{\max}^2 t_{\max}^3} \quad (4.7)$$

From the current maximum of the transient obtained at 0.84V was determined a nucleation rate value of  $J = 2 \times 10^5 \text{ s}^{-1} \text{ cm}^{-2}$ . The saturated number density of nuclei  $N_s$  corresponding to this nucleation rate can be estimated from the equation [49]:

$$N_s = \lim_{t \rightarrow \infty} [N(t)] = J \int_0^\infty \exp(-J\pi k' D t^2 / 2) dt = (J / 2k'D)^{1/2} \quad (4.8)$$

where  $k' = \frac{4}{3} (8\pi V_m c)^{1/2}$ . A value of  $N_s = 6.8 \times 10^5 \text{ cm}^{-2}$  was determined for

$J = 2 \times 10^5 \text{ s}^{-1} \text{ cm}^{-2}$  using Equation (4.8) and the diffusion coefficient  $D = 1.1 \times 10^{-5} \text{ cm}^2 \text{ s}^{-1}$  estimated from the Cottrell dependence in Figure 4.2.

Information about the nucleation kinetics was obtained by analyzing the initial rising parts of current transients obtained in the potential range  $E \geq 0.84$  V, where the nucleation should be progressive. The transient analysis was performed at relatively short times, i.e. before the overlapping of the diffusions zones of growing gold nanoparticles. The initial rising parts of current transients shown in Figure 4.3 are represented in Figure 4.5 as  $i^{2/3}$  vs.  $t$  plots. The observed linear dependences confirm the suggestion that in this potential range the deposition process can be described by the model for progressive nucleation and diffusion-controlled 3D growth (cf. Table 2.1) [3, 49]. According to this model the initial current density by complete diffusion control can be expressed by the equation

$$i^{2/3} = -1.53Dc(\pi JzF)^{2/3}V_m^{1/3}(t - t_0) \quad (4.9)$$

where  $t_0$  represents the induction period.

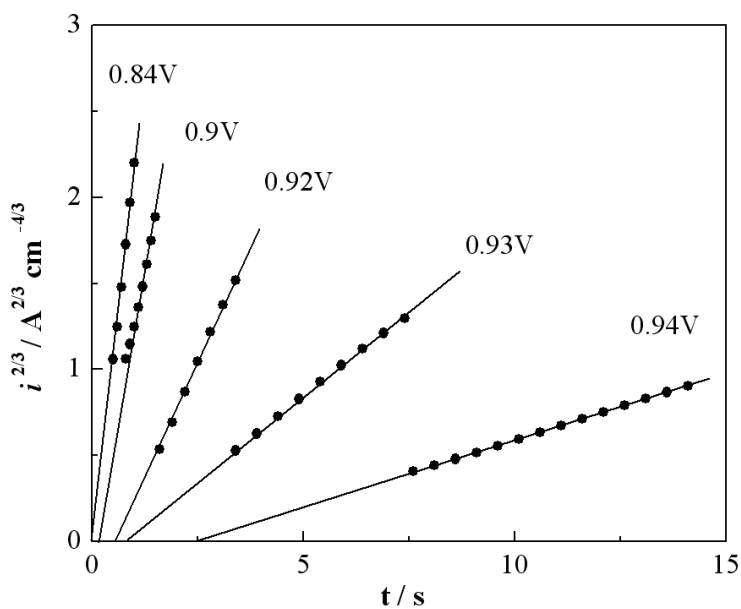


**Figure 4.5**  $i^{2/3}$  vs.  $t$  plots of the initial rising parts of the potentiostatic current transients shown in Figure 4.3.

The nucleation rate  $J$  was extracted from the slopes of the straight lines in Figure 4.5 using Equation (4.9) and the diffusion coefficient  $D = 1.1 \times 10^{-5} \text{ cm}^2 \text{ s}^{-1}$  determined above. The obtained data for the nucleation rate at different electrode potentials were analyzed on the

basis of the atomistic theory of electrochemical nucleation [6-8, 40-42]. According to this theory the nucleation rate  $J$  is given by Equation (2.18), which can be rewritten in the form

$$J(E) = A'(n_{\text{crit}}) \exp \left[ - \frac{(1 - \alpha + n_{\text{crit}})zeE}{k_B T} \right] \quad (4.10)$$

This Equation predicts a change of the slope of the  $\ln J$  vs.  $E$  plot of experimental data if clusters with different size  $n_{\text{crit}}$  are critical nuclei in neighboring potential ranges.

Figure 4.6 represents the experimental data for the nucleation rate at different electrode potentials obtained from the linear  $i^{2/3} - t$  dependences in Figure 4.5. The  $\ln J$  vs.  $E$  plot of the experimental data shows two distinct linear regions in good agreement with the predictions of the atomistic nucleation theory. Values of  $n_{\text{crit}} = 1$  and  $n_{\text{crit}} = 0$  were estimated for the potential ranges  $0.94 \text{ V} > E > 0.91 \text{ V}$  and  $0.91 \text{ V} > E > 0.84 \text{ V}$  from the slopes of the straight lines in Figure 4.6 using Equation (4.10) with  $\alpha = 0.5$ .

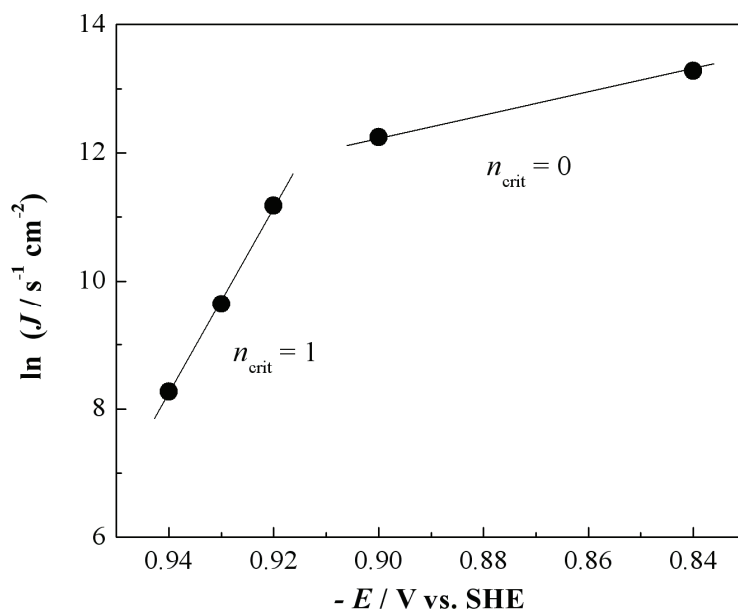


**Figure 4.6** Logarithmic dependence of the nucleation rate on the applied potential obtained from the linear  $i^{2/3} - t$  dependences in Figure 4.5.

These values indicate that in the potential range  $0.94 \text{ V} > E > 0.91 \text{ V}$  a single Au adatom is critical nucleus, whereas at potentials more negative than  $0.91 \text{ V}$  the role of critical nucleus

plays each nucleation site and the single Au atom adsorbed on a nucleation site represents a supercritical cluster, which can grow spontaneously. The results are in agreement with previous studies on gold electrodeposition in a similar system (GC/5mM H<sub>Au</sub>Cl<sub>4</sub> + 6M LiCl [22]), where values of  $n_{\text{crit}}$  below 1 were reported for relatively high cathodic potentials ( $E < 0.84 \text{ V}$ ).

The results presented in Figure 4.4 show clearly that at sufficiently high cathodic potentials the nucleation type changes from progressive to instantaneous. Based on Equation (2.26), a number density of nucleation sites of  $N_0 = 3 \times 10^6 \text{ cm}^{-2}$  was determined from the transient at 0.64V corresponding to instantaneous nucleation. In agreement with the theoretical model, the obtained  $N_0$ -value is larger than the saturated number density of nuclei  $N_s = 6.8 \times 10^5 \text{ cm}^{-2}$  determined above from the analysis of the current transient at 0.84 V corresponding to progressive nucleation.

Information on the morphology, size distribution and number density of electrodeposited gold nanoparticles was obtained by SEM observations. The SEM images of Au nanoparticles deposited in the potential range  $0.84 \text{ V} < E < 0.94 \text{ V}$  show a broad size distribution, which is in good agreement with the progressive nucleation mechanism derived from the analysis of potentiostatic current transients (cf. Figure 4.5). However, a relatively broad size distribution of Au nanoparticles is observed also at deposition potentials  $E \leq 0.64 \text{ V}$  corresponding to instantaneous nucleation if the deposition time is relatively long. In this case the distribution broadening results from the interference of diffusion depletion zones of individual growing particles distributed randomly on the substrate surface. This interparticle diffusion coupling (IPC) leads to dispersion in the growth rates of individual particles and to a broadening of resulting size distribution [107]. However, if the electrodeposition is carried out under conditions of instantaneous nucleation but at relatively short times, the diffusion depletion zones are small and the deposited Au nanoparticles exhibit a relatively uniform size. Thus, in order to obtain Au nanoparticles with a narrow size distribution we applied the so-called double-pulse polarization technique shown schematically in Figure 4.7. The first short pulse (with a duration  $t_1$ ) to a relatively high cathodic potential  $E_1$  leads to deposition of small Au nanoclusters under conditions of instantaneous nucleation. During the following second pulse to a relatively low cathodic potential  $E_2$  (much lower than the critical potential for nucleation), a formation of new nuclei is impossible and the Au nanoclusters formed during the first pulse grow further under kinetic control. The nanoparticles deposited under these conditions exhibit a uniform size determined by the potential  $E_2$  and duration  $t_2$  of the

second potential pulse. Basically, this technique separates the nucleation and growth processes in time and has been developed originally for experimental studies of electrocrystallization [4,6,8]. Recently the double-pulse method has been applied successfully also for electrodeposition of compact thin metal films [108] and metal nanoparticles with narrow size distribution [107].

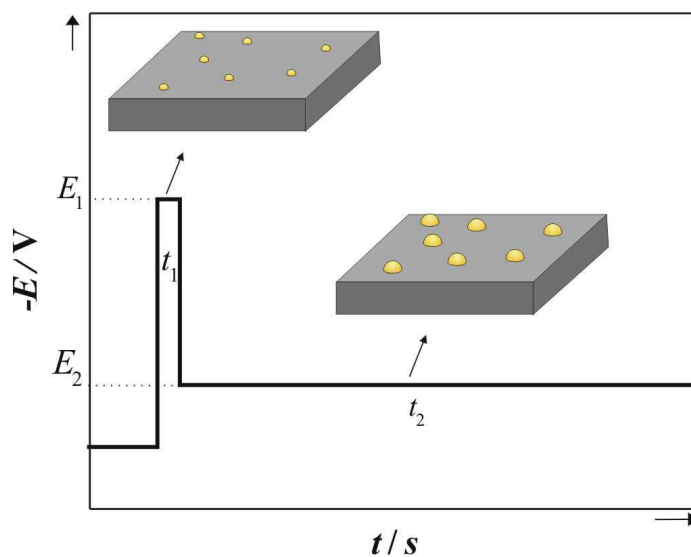


**Figure 4.7** Schematic representation of the double-pulse polarization technique

Figures 4.8 shows SEM images of Au nanoparticles created under conditions of instantaneous nucleation by single-pulse deposition at  $E = 0.64$  V for  $t = 100$  ms (Figure 4.8a) and by double-pulse deposition with a first pulse at  $E_1 = 0.64$  V for  $t_1 = 1$  ms and a second pulse at  $E_2 = 0.99$  V for  $t_2 = 120$  s (Figure 4.8b). The Au nanoparticles observed in both images are distributed randomly on the GC substrate indicating a random distribution of the nucleation sites. In the case of double-pulse electrodeposition is obtained a narrower size distribution, which demonstrates the applicability of this technique for preparation of Au nanoparticles.

The analysis of SEM images of Au nanoparticles created by electrodeposition under conditions of instantaneous nucleation shows  $N_0$ -values ranging between  $2 \times 10^8 \text{ cm}^{-2}$  and  $5 \times 10^8 \text{ cm}^{-2}$ . These values are about two orders of magnitude higher than the value of  $N_0 = 3 \times 10^6 \text{ cm}^{-2}$  obtained above from the analysis of the current transient at  $E = 0.64$  V (Figure 4.4).



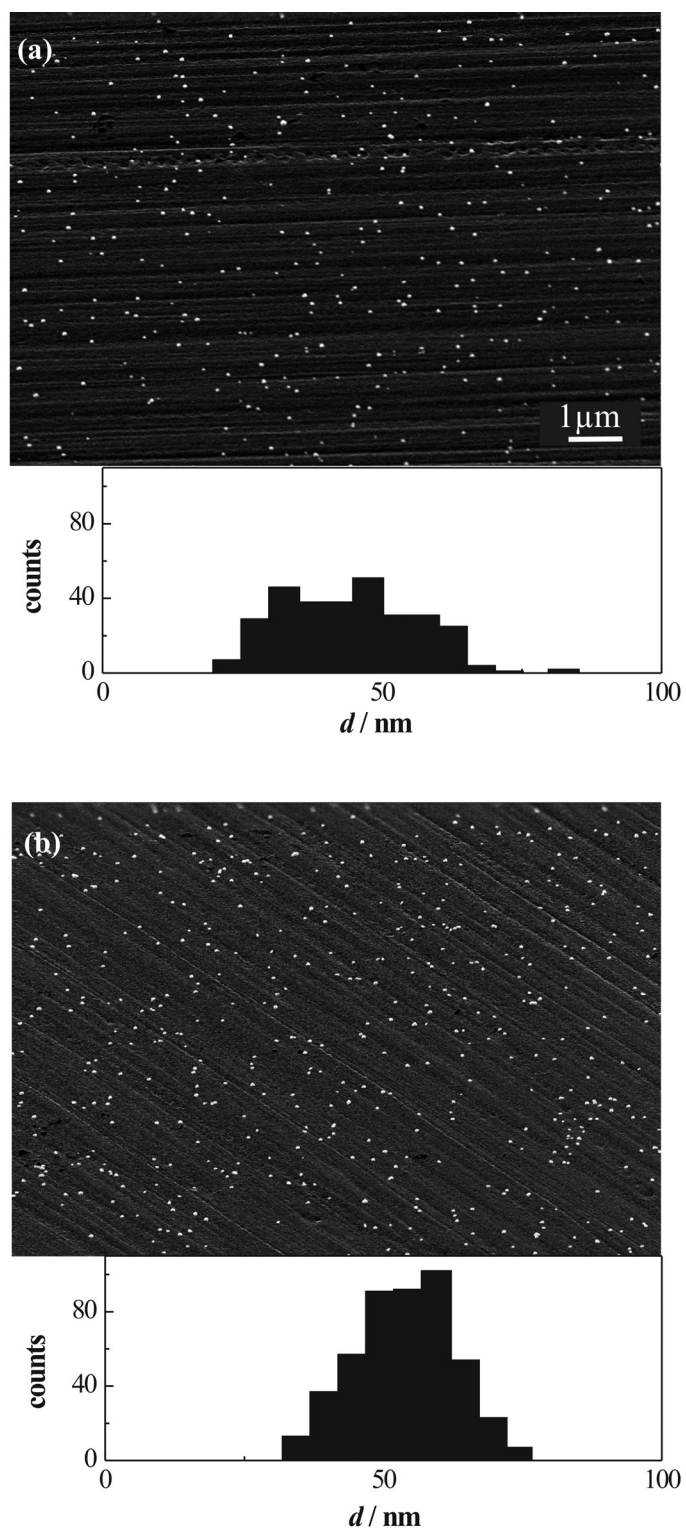


**Figure 4.8** SEM images of Au nanoparticles deposited in the system GC/1mM KAuCl<sub>4</sub> + 0.1M HClO<sub>4</sub>. (a): single-pulse deposition at  $E = 0.64 \text{ V}$  for  $t = 100 \text{ ms}$ ; (b): double-pulse deposition ( $E_1 = 0.64 \text{ V}$ ,  $t_1 = 1 \text{ ms}$ ;  $E_2 = 0.99 \text{ V}$ ,  $t_2 = 120 \text{ s}$ ). The corresponding size distributions are shown at the bottom side of the images.

Thus, the results presented in Figures 4.4 and 4.5 should be considered as a qualitative agreement between the experimental current transients and theoretical current-time relations. Differences between the calculated and microscopically determined values of the number densities of nuclei and nucleation sites have been reported by many authors and have been related to possible deviations of real experimental systems from the theoretical models [109-116]. Recently Radisic et al. [117-119] reported interesting *in situ* transmission electron microscopy (TEM) studies of electrochemical nucleation and growth of Cu nanoparticles on Au substrates. The obtained results for the size and the number density of growing Cu nanoparticles determined by *in situ* TEM and predicted by the theoretical models show significant discrepancy. The authors suggested that this discrepancy is due to processes of adsorption and surface diffusion involved in the very initial deposition stages, which are not included in the conventional theoretical models. However, the question why the microscopic observations show nuclei number densities several order of magnitude higher than those predicted by the theoretical models remains to be answered.

The initial stages of gold electrodeposition on GC substrates were studied also in the system GC/5mM HAuCl<sub>4</sub> + 42mM Na<sub>2</sub>S<sub>2</sub>O<sub>3</sub> + 42mM Na<sub>2</sub>SO<sub>3</sub> (pH~7.5). As already discussed in section 3.1, in this system the gold exists as a [Au(S<sub>2</sub>O<sub>3</sub>)(SO<sub>3</sub>)<sub>2</sub>]<sup>5-</sup> complex ion in the electrolyte solution and the overall deposition process can be described by the reaction

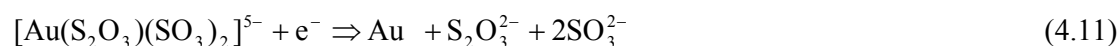
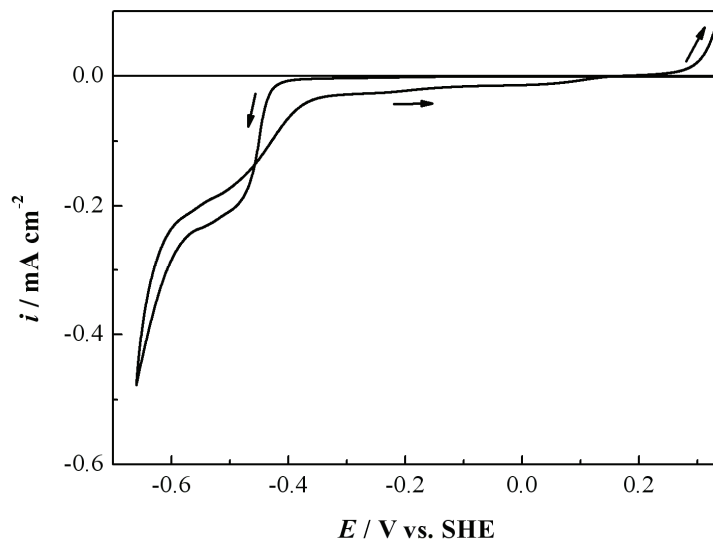


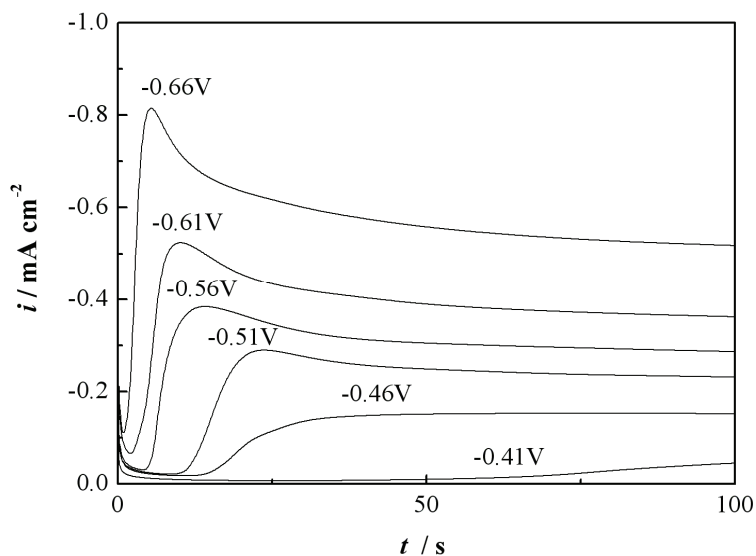
Figure 4.9 shows the cyclic voltammogram for gold electrodeposition in this system. As can be seen, during the initial cathodic scan the sharp increase of the cathodic current is observed at potentials more negative than -0.4 V. However, the open circuit potential of flame-annealed gold wire in freshly prepared electrolyte solution is  $E^{\text{OCP}} \approx 0.2 \text{ V}$ . Thus, the cyclic voltammogram reveals that the process of Au electrodeposition on the GC substrate starts at very high cathodic overpotentials indicating a significant barrier for nucleation of the 3D bulk Au phase in this system. Due to the high cathodic potentials ( $E < -0.4 \text{ V}$ ), the processes of nucleation and the growth of gold nanoparticles in the initial deposition stages interfere with the simultaneously occurring hydrogen evolution.

Figure 4.10 shows a series of potentiostatic transients, obtained during gold electrodeposition at different cathodic potentials. The initial parts of the transients are characterized by a

relatively slow initial current decay, which could be assigned to the slow formation of Au adatoms on the electrode surface. This current decay is followed by a current increase, due to the nucleation and growth of the 3D Au phase.



**Figure 4.9** Cyclic voltammogram of Au electrodeposition in the system GC/5mM H<sub>AuCl</sub><sub>4</sub> + 42mM Na<sub>2</sub>S<sub>2</sub>O<sub>3</sub> + 42mM Na<sub>2</sub>SO<sub>3</sub> ( $|dE/dt| = 1 \text{ mV s}^{-1}$ ).



**Figure 4.10** Potentiostatic current transients for deposition of gold at different electrode potentials in the system GC/5mM H<sub>AuCl</sub><sub>4</sub> + 42mM Na<sub>2</sub>S<sub>2</sub>O<sub>3</sub> + 42mM Na<sub>2</sub>SO<sub>3</sub>.

At longer times the current passes through a maximum and reaches a steady state value. With increasing cathodic potential the current maximum appears at shorter times as expected for a

diffusion-controlled deposition process. The observed steady state current increases with increasing cathodic potential, which indicates a significant contribution of the hydrogen evolution. Therefore, a quantitative transient analysis based on the existing theoretical nucleation and growth models was impossible in this system.

However, recently Zach and Penner [120] have shown that the hydrogen coevolution can be advantageous for the diffusion-controlled electrodeposition of metal nanoparticles with narrow size distribution. These authors demonstrated that Ni particles with a uniform size can be prepared by single pulse electrodeposition at relatively high cathodic potentials under conditions of massive H<sub>2</sub> coevolution. The effect was attributed mainly to the local stirring of electrolyte solution in the vicinity of the growing nanoparticles by the evolution of H<sub>2</sub> bubbles, which reduces significantly the interparticle diffusion coupling. However, up to now this “H<sub>2</sub> coevolution technique” could be applied successfully only for electrodeposition of ferromagnetic Ni, Co and Fe nanoparticles [107]. Thus, the detailed deposition mechanism is not completely clarified.

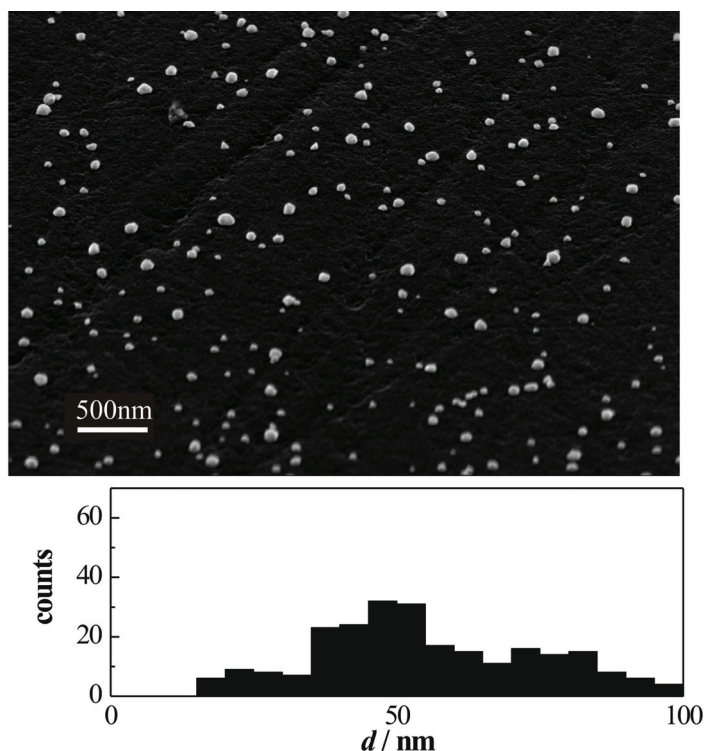


**Figure 4.11** SEM image and the corresponding size distribution of Au nanoparticles deposited in the system GC/5mM HAuCl<sub>4</sub> + 42mM Na<sub>2</sub>S<sub>2</sub>O<sub>3</sub> + 42mM Na<sub>2</sub>SO<sub>3</sub> at  $E = -1$  V for  $t = 1$  s .

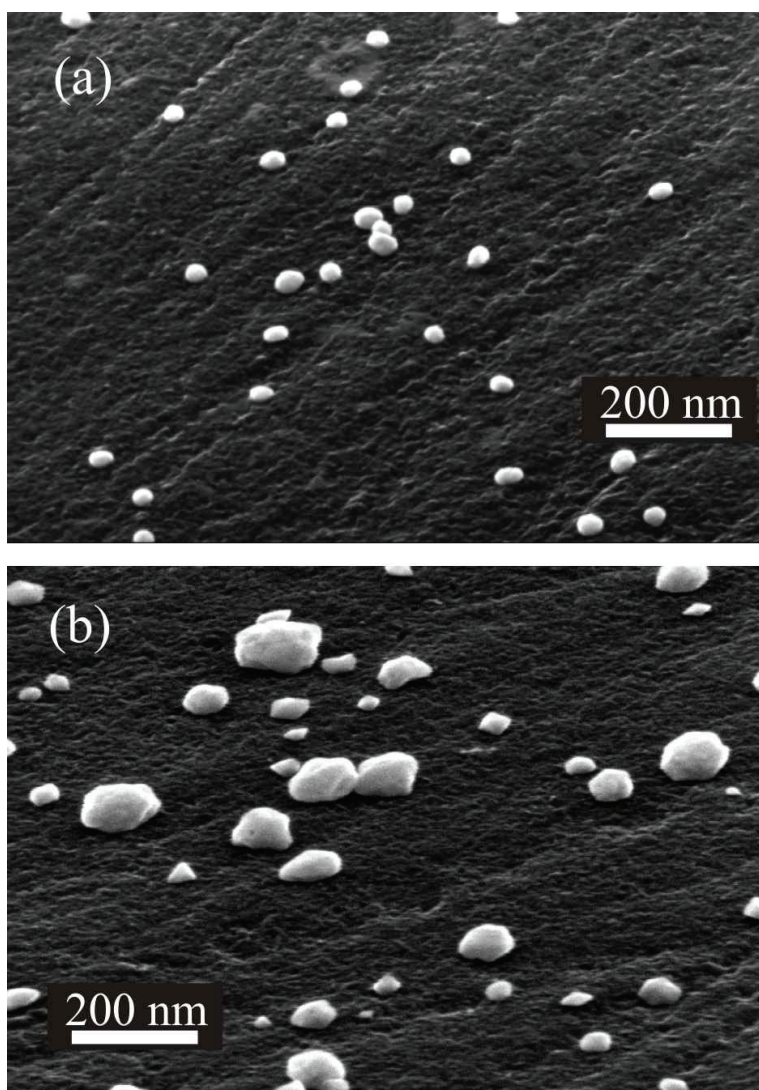


**Figure 4.12** SEM images of Au nanoparticles electrodeposited in the systems (a): GC/1mM KAuCl<sub>4</sub> + 0.1M HClO<sub>4</sub> at  $E = 0.64$  V for  $t = 100$  ms and (b): GC/5mM HAuCl<sub>4</sub> + 42mM Na<sub>2</sub>S<sub>2</sub>O<sub>3</sub> + 42mM Na<sub>2</sub>SO<sub>3</sub> at  $E = -1$  V for  $t = 1$  s .

The attempts to apply the “H<sub>2</sub> coevolution technique” for deposition of Au nanoparticles with a narrow size distribution in the system GC/5mM HAuCl<sub>4</sub> + 42mM Na<sub>2</sub>S<sub>2</sub>O<sub>3</sub> + 42mM Na<sub>2</sub>SO<sub>3</sub> were unsuccessful. Figure 4.11 shows as an example a SEM image of Au nanoparticles electrodeposited in this system by single potential pulse to  $E = -1$  V , where the Au electrodeposition is accompanied by a massive hydrogen coevolution. As seen, the corresponding size distribution is very broad and the size of deposited Au particles ranges between 10 and 100 nm. Electrodeposition of Au nanoparticles with uniform size could not be achieved in this system also by the double-pulse deposition technique applied successfully in the system GC/1mM KAuCl<sub>4</sub> + 0.1M HClO<sub>4</sub>. The results presented above indicate that the

electrodeposition of gold in the system GC/5mM  $\text{HAuCl}_4$  + 42mM  $\text{Na}_2\text{S}_2\text{O}_3$  + 42mM  $\text{Na}_2\text{SO}_3$  is strongly inhibited and the involved nucleation process remains progressive even at very high cathodic potentials.

The different properties of the electrolytes in both investigated systems influence significantly not only the electrodeposition kinetics but also the morphology of gold nanoparticles. Figure 4.12 shows two high magnification SEM images of Au particles deposited at relatively high cathodic potentials in both electrochemical systems. The gold nanoparticles electrodeposited in the system GC/1mM  $\text{KAuCl}_4$  + 0.1M  $\text{HClO}_4$  exhibit uniform size and a hemispherical shape. In contrast, the Au particles, obtained in the system GC/5mM  $\text{HAuCl}_4$  + 42mM  $\text{Na}_2\text{S}_2\text{O}_3$  + 42mM  $\text{Na}_2\text{SO}_3$  are characterized by different sizes and show a faceting.

In the next section are presented and discussed some experimental studies dealing with the additional UPD modification of the Au nanoparticles electrodeposited in the system GC/1mM  $\text{KAuCl}_4$  + 0.1M  $\text{HClO}_4$ .

#### **4.1.2 Modification of Au nanoparticles by Cu UPD**

Underpotential deposition (UPD) of metals is a versatile method for preparation of epitaxial monolayers on noble metal single crystal substrates and received much attention in the recent years [4,39,121-124]. Recently, the UPD of Cu has been used as an intermediate step in the preparation of Au nanoparticles modified by a Pt monolayer electrocatalyst [125-127].

In the present work the Au nanoparticles electrodeposited on GC by the double-pulse technique described in the previous section were modified by selective UPD of Cu. The UPD modification was used for both characterization of the electrochemical behaviour of gold nanoparticles and preparation of Pt monolayer electrocatalysts.

Figure 4.13a shows cyclic voltamograms measured in the underpotential range of Cu on a bare GC substrate and a GC substrate modified with Au nanoparticles (GC/Au). As expected, no UPD of Cu is observed on the bare GC substrate. The redox peaks observed in the voltammogram obtained on the GC/Au substrate are related to the deposition and dissolution of the Cu monolayer on the surface of the gold nanoparticles.

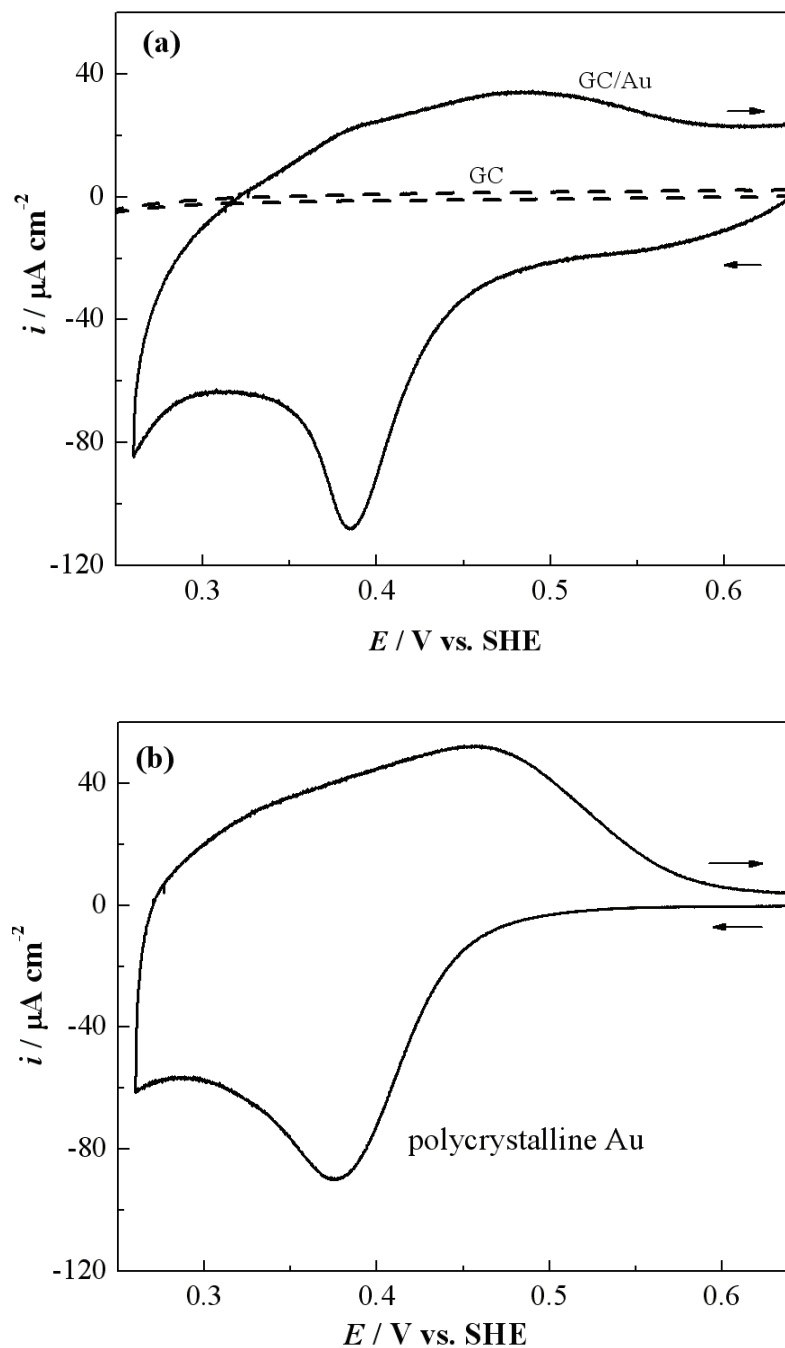


**Figure 4.13** Cyclic voltammograms obtained in the UPD range of Cu in 1mM CuSO<sub>4</sub> + 0.1M H<sub>2</sub>SO<sub>4</sub> ( $|dE/dt| = 50 \text{ mV s}^{-1}$ ). (a): bare GC substrate (dashed line) and GC/Au substrate (solid line) modified with Au nanoparticles by the double-pulse deposition technique ( $E_1 = 0.64 \text{ V}$ ,  $t_1 = 1 \text{ ms}$ ;  $E_2 = 0.99 \text{ V}$ ,  $t_2 = 240 \text{ s}$ ); (b): polycrystalline Au microelectrode.

Figure 4.13b shows the corresponding cyclic voltammogram obtained by the same conditions on a polycrystalline Au microelectrode. The comparison shows that the positions of redox peaks in both cyclic voltammograms are similar, which indicates that the electrodeposited Au nanoparticles do not exhibit some preferential faceting in good agreement with SEM observations (cf. Figure 4.12a).

In Figure 4.14 is shown schematically the procedure used for modification of electrodeposited Au nanoparticles by a Pt monolayer. In the first step the Au nanoparticles electrodeposited by the double-pulse technique on the GC substrate were modified by a Cu UPD monolayer at  $E = 0.25$  V for 120s. In the following step the Cu UPD monolayer was replaced with a Pt monolayer by immersing the modified GC substrate in an electrolyte solution containing complex  $[\text{PtCl}_4]^{2-}$  ions. In this electroless displacement process the copper UPD atoms  $\text{Cu}^0$  undergo an irreversible oxidation up to  $\text{Cu}^{2+}$  ions, supplying the necessary electrons for reduction of  $[\text{PtCl}_4]^{2-}$  ions to platinum atoms  $\text{Pt}^0$ . Under these conditions on the gold nanoparticles is formed a shell Pt monolayer coverage

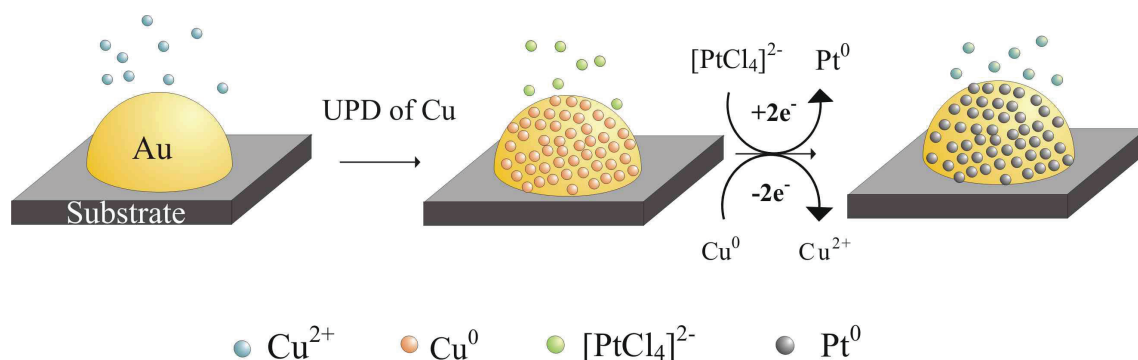


**Figure 4.14** Schematic presentation of the procedure applied for preparation of Au/Pt (core/shell) nanoparticles involving UPD of a copper monolayer and its displacement by Pt.

The presence of Pt monolayer, covering the gold nanoparticles was detected using the methanol electrooxidation reaction, since Au and GC exhibit much lower electrocatalytic activity towards this reaction. In Figure 4.15 are compared the voltametric curves obtained before and after the modification of electrodeposited Au nanoparticles with a Pt monolayer in a methanol containing electrolyte (0.5M  $\text{H}_2\text{SO}_4$  + 1M  $\text{CH}_3\text{OH}$ ) solution.



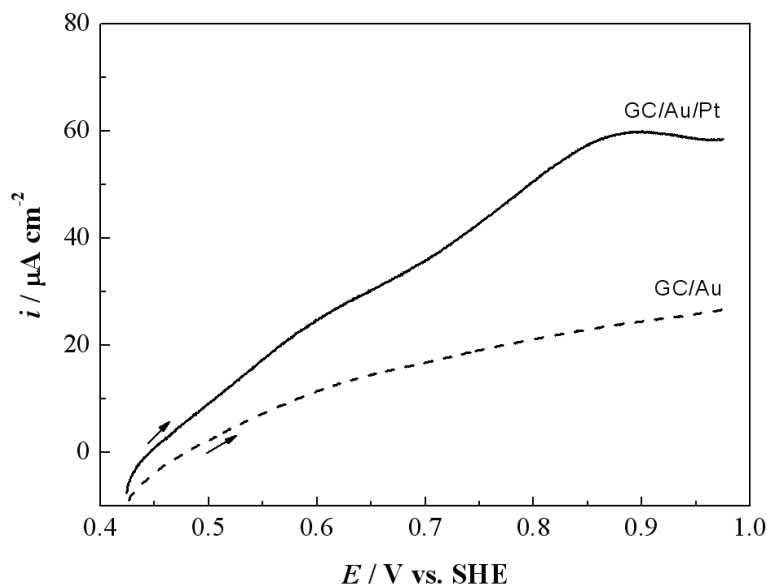


**Figure 4.15** Anodic voltammetric curves obtained in 0.5M H<sub>2</sub>SO<sub>4</sub> + 1M CH<sub>3</sub>OH on (a): GC substrate modified with Au nanoparticles (GC/Au) and (b): GC substrate modified with Au/Pt (core/shell) nanoparticles;  $|dE/dt| = 50 \text{ mV s}^{-1}$ .

As expected the modified Au/Pt nanoparticles show a much higher electrocatalytic activity toward methanol oxidation reflected in the increased anodic current. The prepared Au/Pt (core/shell) nanoparticles show a good long term catalytic response towards the methanol electrooxidation and can be applied successfully as electrocatalysts in the fuel cell technology.

## 4.2 Electrochemical Deposition and Properties of Thin PANI Films

### 4.2.1 Kinetics and mechanism of PANI film formation on Au(111) and p-Si(111)

The kinetics and mechanism of very initial stages of PANI electrodeposition on Au(111) and p-Si(111) substrates have been studied analyzing potentiostatic current transients. The transient measurements were performed in the potential range  $0.9 \text{ V} < E < 1 \text{ V}$ . However, as already mentioned in the introduction chapter, in this potential range the electropolymerization process on p-Si(111) substrates is accompanied by an anodic oxidation of silicon and the deposition of PANI occurs practically on a substrate modified by a thin SiO<sub>2</sub> film. In this case the contribution of anodic oxidation of silicon to the total transient

current complicates the analysis of current transients and the evaluation of PANI deposition kinetics. Thus, in order to avoid this complication, prior to each transient measurement the H-terminated p-Si(111) substrates were oxidized potentiodynamically with 50 mV/s up to 1V in an aniline free sulfuric acid solution. Under these conditions the silicon substrate becomes modified by a thin SiO<sub>2</sub> layer with an average thickness of about 1.5 nm [128,129]. During PANI electrodeposition on such substrates in the potential range  $0.9 \text{ V} < E < 1 \text{ V}$  the oxide film remains practically unchanged and the corresponding current transients can be related only to the polymer deposition kinetics.

Typical current transients for PANI electrodeposition on Au(111) and oxide modified p-Si(111) substrates are shown in Figs. 4.16a and 4.17a respectively. The shape of the transients observed during the polymerization on both substrates is characterized by two rising parts (at short and long times) divided by a shoulder, in good agreement with previous studies of PANI deposition on Au and Pt microelectrodes [33-35]. The very initial parts of the transients correspond to the initial stages of formation of PANI layers involving appearance and growth of islands consisting of 1D polymer chains. The current increase observed at longer times (after the shoulder) is related to a progressive branching of the growing polymer chains, which leads to an exponential increase of growth sites and the growth current. As already discussed in section 2.2.2, information on the initial stages of PANI electrodeposition can be obtained analyzing the initial parts of current transients on the basis of phenomenological growth models developed for the case of electrocrystallization of metals (cf. Table 2.1).

Figures 4.16b and 4.17b show the initial parts of experimental current transients in Figures. 4.16a and 4.17a as  $i^{1/2}$  vs.  $t$  and  $i^{1/3}$  vs.  $t$  plots. The observed linear plots indicate that the current transients for the initial stages of formation of PANI films on Au(111) and p-Si(111) can be described by the relations

$$i(t) = K'(E)(t - t_0)^2 \quad (4.12)$$

$$i(t) = K''(E)(t - t_0)^3 \quad (4.13)$$

In these relations  $t_0$  represents the induction period and the constants  $K'$  and  $K''$  depend on the electrode potential  $E$  and the growth geometry. Equations (4.12) and (4.13) correspond to

models including appearance and charge transfer controlled (kinetically controlled) 2D or 3D growth of polymer islands (cf. Table 2.1).

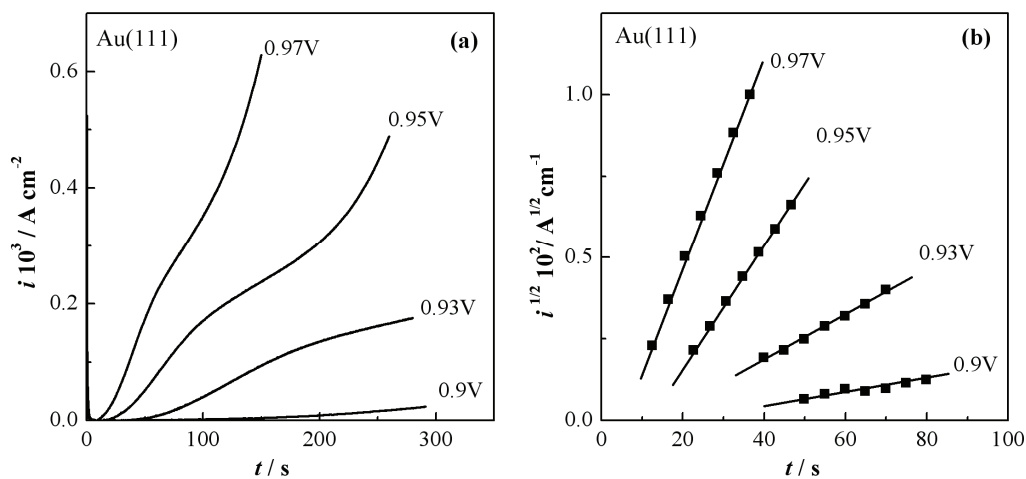


**Figure 4.16** Potentiostatic current transients for electrodeposition of PANI in the system Au(111)/0.1M Aniline+0.5M H<sub>2</sub>SO<sub>4</sub> (a): overall transients; (b):  $i^{1/2}$  vs.  $t$  plots of the initial parts of the transients in (a).

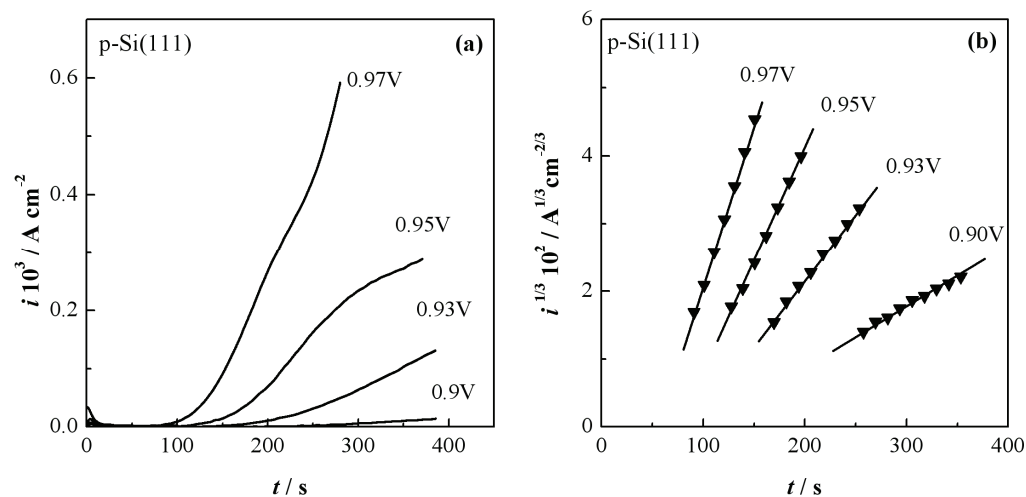


**Figure 4.17** Potentiostatic current transients for electrodeposition of PANI in the system p-Si(111)/0.1M Aniline+0.5M H<sub>2</sub>SO<sub>4</sub> (a): overall transients; (b):  $i^{1/3}$  vs.  $t$  plots of the initial parts of the transients in (a).

Two different growth models could be attributed to the time dependence given by Equation (4.12): (i) a model including progressive appearance and 2D growth of polymer islands or (ii) a model including instantaneous appearance and 3D island growth. Previous studies have shown clearly that the initial stages of PANI electrodeposition on polycrystalline gold microelectrodes involve appearance and 2D growth of polymer islands [33]. Thus, it is reasonable to suggest that in the case of PANI electrodeposition on Au(111) the observed current-time dependence (Figure 4.16b) can be explained by the model for progressive appearance and 2D island growth corresponding to Equation (4.12). The initial  $i(t)$  dependence obtained on p-Si(111) (cf. Figure 4.17b and Equation (4.13)) corresponds to a growth model with progressive appearance and 3D growth of polymer islands (cf. Table 2.1).

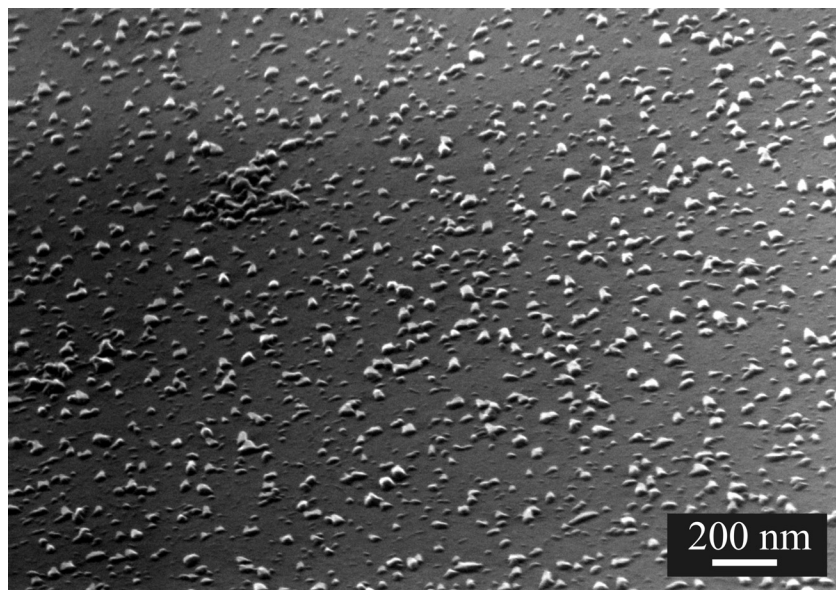


**Figure 4.18** SEM image of PANI deposit obtained in the system p-Si(111)/0.1M Aniline+0.5M  $\text{H}_2\text{SO}_4$  by electrodeposition at  $E = 0.93\text{V}$  for  $t = 250\text{s}$ .

A typical SEM image of PANI deposit on p-Si(111) obtained after deposition at 0.93 V for 250 s is shown in Figure 4.18. The observed 3D PANI islands with wide size distribution confirm the proposed mechanism involving progressive appearance and 3D growth. The transients for PANI electrodeposition on p-Si(111) in Figure 4.17a show a much longer induction period  $t_0$ , which can be attributed to the poorly conductive thin  $\text{SiO}_2$  film modifying the silicon surface.

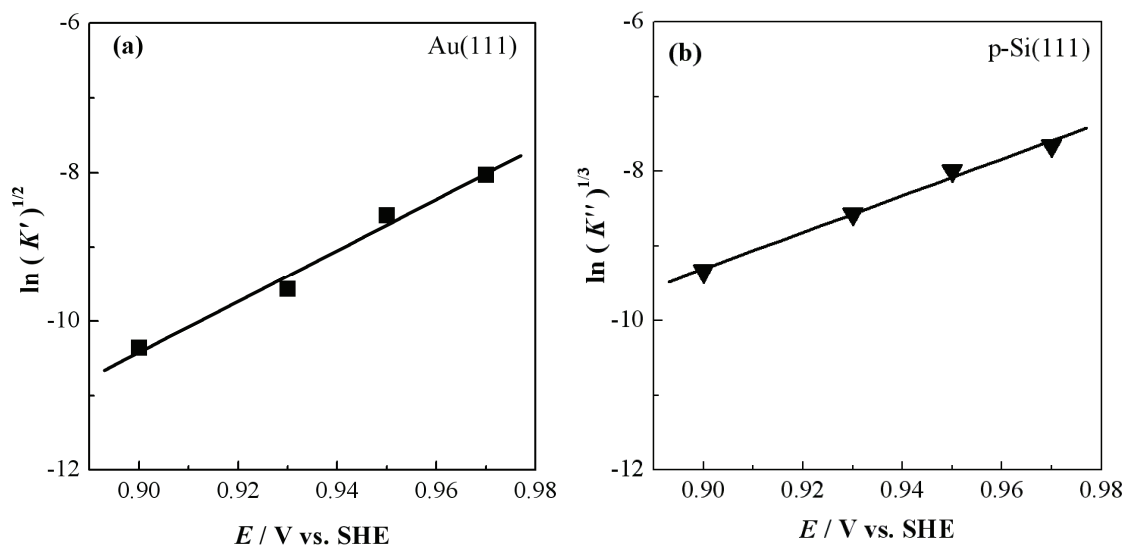
For relatively high anodic potentials  $E \gg k_B T / ze$  the prefactors  $K'$  and  $K''$  in Equations (4.12) and (4.13) can be expressed by

$$K'(E) = k_{ct}(E)A_{2D}(E) \sim \exp(3\alpha zeE / k_B T) \quad (4.14)$$

$$K''(E) = K_{ct}(E)A_{3D}(E) \sim \exp(4\alpha zeE / k_B T) \quad (4.15)$$

where  $k_{ct}(E) \sim \exp(2\alpha zeE / k_B T)$ ,  $K_{ct}(E) \sim \exp(3\alpha zeE / k_B T)$ ,  $\alpha$  is the anodic charge transfer coefficient (cf. Table 2.1) and  $z$  is the number of electrons involved in the electropolymerization reaction. The relations (4.14) and (4.15) suggest that the rates of appearance of stable growing 2D and 3D polymer islands  $A_{2D}(E)$  and  $A_{3D}(E)$  are proportional to the anodic term  $\exp(\alpha zeE / k_B T)$  of the well known Butler-Volmer relation.

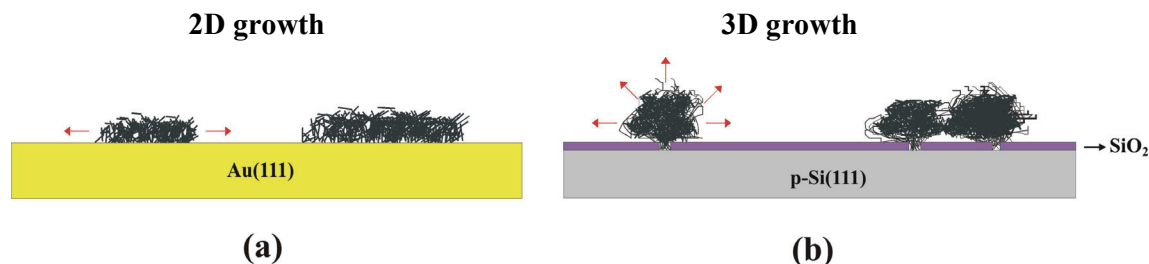
Figure 4.19 shows the slopes  $(K')^{1/2}$  and  $(K'')^{1/3}$  of experimental  $i^{1/2} - t$  and  $i^{1/3} - t$  dependences in Figures 4.16b and 4.17b as a function of the electrode potential  $E$ .



**Figure 4.19**  $\ln(K')^{1/2}$  vs.  $E$  (a) and  $\ln(K'')^{1/3}$  vs.  $E$  (b) plots of the slopes of experimental  $i^{1/2} - t$  and  $i^{1/3} - t$  dependences in Figures 4.16b and 4.17b.

From the slopes of the obtained linear  $\ln(K')^{1/2} - E$  and  $\ln(K'')^{1/3} - E$  dependences were estimated  $\alpha z$ -values of  $0.59 \pm 0.05$  and  $0.49 \pm 0.05$  for the Au(111) and p-Si(111), respectively. These results are in good agreement with the  $\alpha z$ -values reported previously for

polycrystalline Au and Pt microelectrodes [33,34] and indicate that the charge transfer stoichiometry of PANI electrodeposition in the initial deposition stages does not depend significantly on the substrate nature.



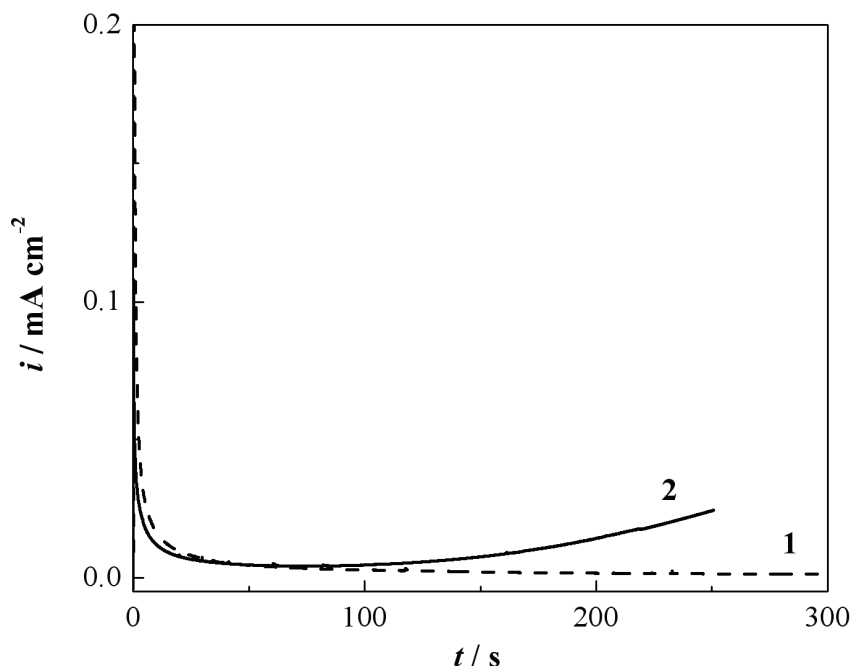
**Figure 4.20** Schematic representation of initial stages of PANI electrodeposition on (a): Au(111) and (b): p-Si(111).

Figure 4.20 represents schematically the proposed mechanisms of the initial stages of PANI electrodeposition on Au(111) and p-Si(111) substrates. The preferential island growth in the lateral direction (2D growth) on Au(111) is attributed to the high electronic conductivity of the gold substrate and the good adhesion of PANI (Figure 4.20a). In the case of PANI electrodeposition on p-Si(111) is suggested that the 3D island growth arises from the presence of the thin anodic SiO<sub>2</sub> surface film, which is inhomogeneous and exhibits a number of defects acting as active sites for the appearance and growth of the polymer islands (Figure 4.20b).

Additional experiments were performed on p-Si(111) substrates covered by a native SiO<sub>2</sub>, in order to understand better the role of the surface oxide layer in the initial stages of PANI electrodeposition. Figure 4.21 shows a potentiostatic current transient (curve 1) measured at  $E = 0.93$  V on p-Si(111) covered by a native oxide. As seen, no current increase related to PANI electrodeposition is observed in the time scale of 300 s, which indicates that under these conditions the electropolymerization process is strongly inhibited. This behavior was confirmed also by SEM observations and can be addressed to the homogeneous and compact native SiO<sub>2</sub> film in comparison to the electrochemical anodic oxide layer.

However, a cathodic gold photoelectrodeposition can be realized successfully on native oxide modified p-Si(111) substrates. The electrodeposition of gold was performed under illumination from the gold thiosulphate-sulphite electrolyte solution described in sections 3.1 and 4.1.

Figure 4.22a shows a SEM image of gold nanoparticles, which has been deposited on p-Si(111) covered by native oxide applying a deposition potential of  $E = -0.46$  V for 10 s. The current transient for PANI electrodeposition obtained at  $E = 0.93$  V on such p-Si(111)/SiO<sub>2</sub>/Au substrate (curve 2 in Figure 4.21) shows that gold nanoparticles catalyze the electropolymerization process and act as active deposition sites.



**Figure 4.21** Current transients for potentiostatic deposition of PANI at  $E = 0.93$  V on p-Si(111) covered by a native oxide in absence (dashed curve 1) and in presence (solid curve 2) of Au nanoparticles photoelectrodeposited at  $E = -0.46$  V for  $t = 10$  s.

The SEM image in Figure 4.22b represents the PANI deposit corresponding to curve 2 in Figure 4.21. The observed morphology is rather surprising and shows that the PANI covers not only the gold nanoparticles but also the surface of the insulating native SiO<sub>2</sub> film. This behavior is illustrated more clearly in Figure 4.22c showing a SEM image of PANI deposit obtained at longer deposition time of 300 s. These results indicate that under these deposition conditions PANI is in direct electrical contact only with the gold nanoclusters and the observed enhanced lateral growth on the insulating SiO<sub>2</sub> surface is due to autocatalytic and branching effects during the polymerization process.



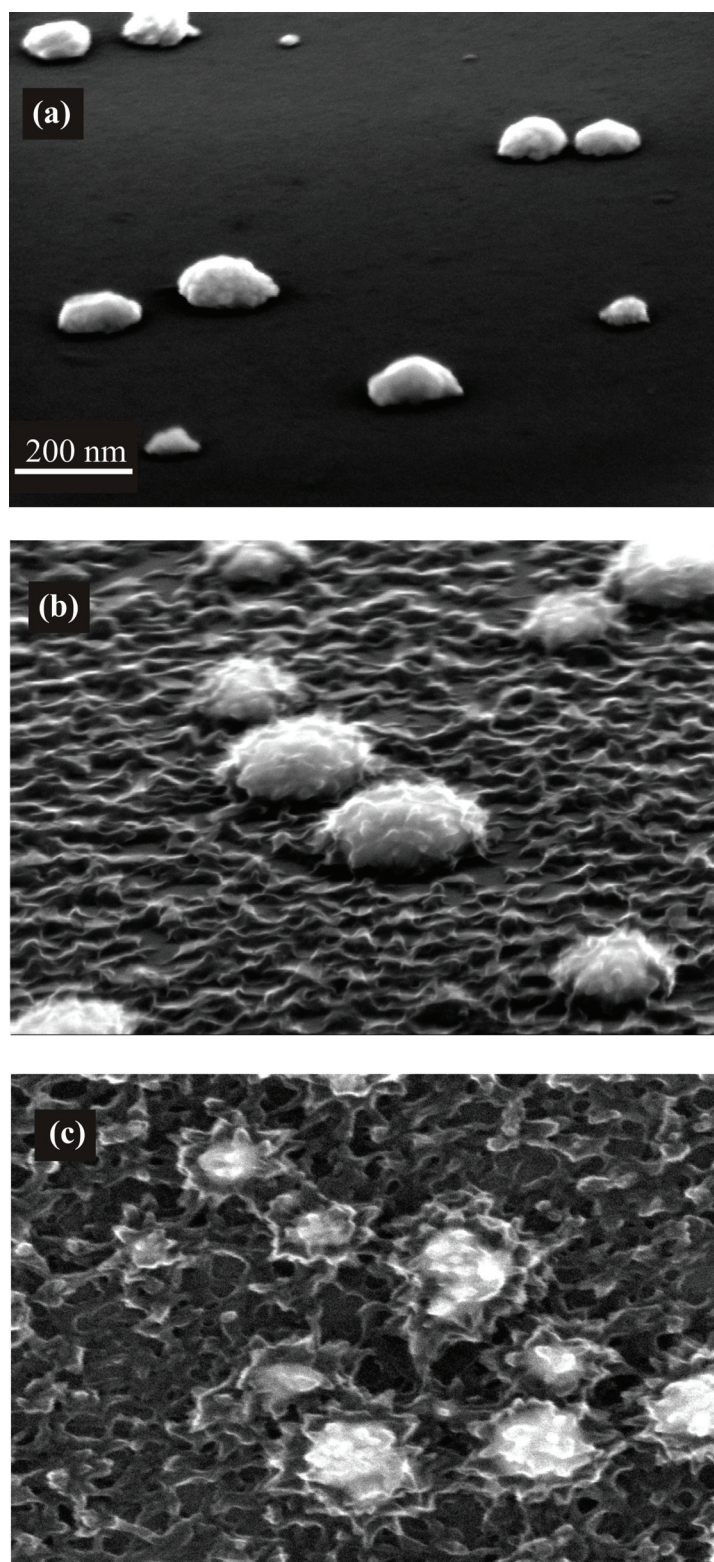
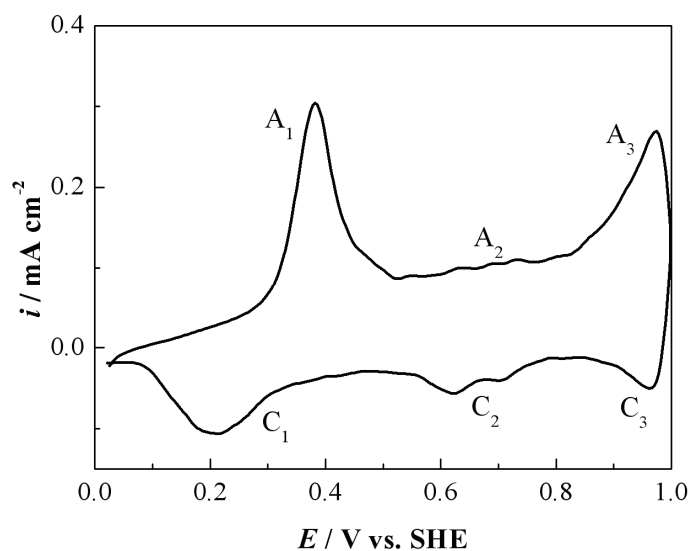


**Figure 4.22** SEM images of gold nanoparticles, photoelectrodeposited at  $E = -0.46$  V for 10 s on p-Si(111) covered by native oxide. (a): unmodified gold nanoparticles; (b): gold nanoparticles modified by electrodeposition PANI at 0.93V for 250s; (c): gold nanoparticles modified by electrodeposition PANI at 0.93V for 300s.



#### 4.2.2 Electrochemical behaviour of PANI films on Au(111) and p-Si(111)

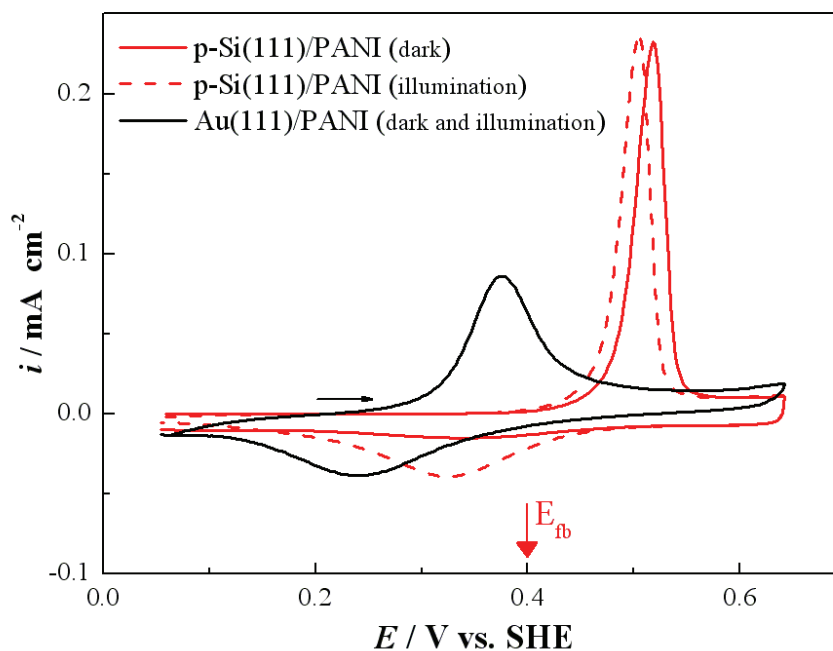
The electrochemical behavior of electrodeposited PANI layers was studied in a monomer free acid electrolyte (0.5M  $\text{H}_2\text{SO}_4$ ) using cyclic voltammetry, potentiostatic transient measurements and electrochemical impedance spectroscopy. Figure 4.23 shows a typical cyclic voltammogram measured in the potential range  $0\text{ V} < E < 1\text{ V}$  on a PANI film electrodeposited potentiostatically on Au(111). The first peak pair  $A_1/C_1$  refers to the anodic oxidation of the nonconductive LM form to the conductive EM state and to the reversed cathodic reduction reaction (cf. section 3.3). The second peak pair  $A_2/C_2$  is addressed usually to side reactions occurring in the deposited PANI film such as hydrolysis, degradation and oxidation of short oligomeric chains, trapped into the polymer matrix [130,131]. The peak pair  $A_3/C_3$  appearing at more anodic potentials ( $E > 0.9\text{ V}$ ) is assigned to the transition of the EM form to the low conductive PN form and to the reverse PN-EM transition.



**Figure 4.23** Cyclic voltammogram measured in aniline free 0.5M  $\text{H}_2\text{SO}_4$  solution on a PANI film electrodeposited potentiostatically on Au(111);  $|dE/dt| = 5\text{ mV s}^{-1}$ .

In order to avoid the influence of the degradation reactions the electrochemical behavior of electrodeposited PANI films was investigated in the potential range  $0\text{ V} < E < 0.64\text{ V}$ , where only the switching between the LM and EM forms takes place. Figure 4.24 shows typical cyclic voltammograms of PANI films on Au(111) and electrochemically oxidized p-Si(111) measured in the switching region starting from the fully reduced LM state at 0V. From the cyclic voltammogram can be estimated the so-called redox charge density defined as

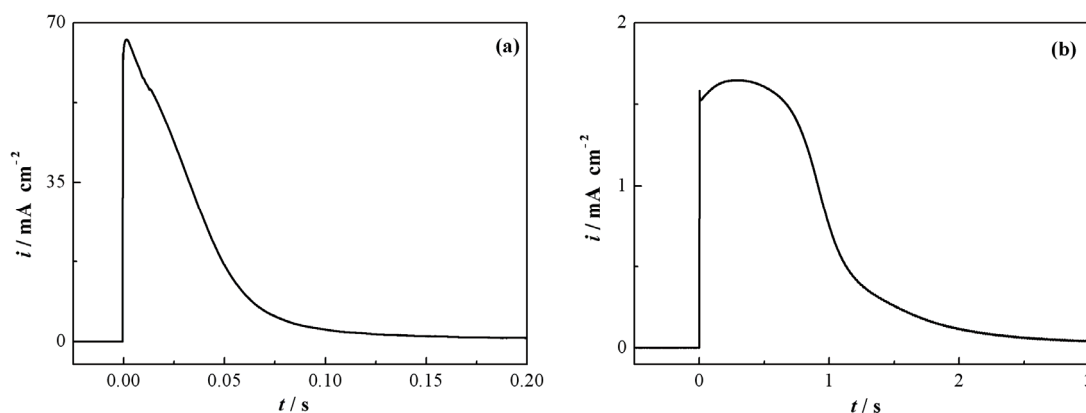
$Q = (Q_{A_1} + |Q_{C_1}|)/2$ , which can be used as a qualitative measure for the quantity of deposited electroactive polymer. The redox charge density  $Q$  estimated from the cyclic voltammograms is similar for both PANI layers. The cyclic voltammogram obtained on Au(111)/PANI shows the characteristic anodic and cathodic peaks ( $A_1$  and  $C_1$ ) for the redox transitions between the insulating LM state and the conductive EM state (cf. Figure 4.23). Measurements on p-Si(111)/PANI show that the anodic peak  $A_1$  is shifted to more positive electrode potentials close to the flat band potential of p-Si ( $E_{fb} \approx 0.4V$ ) [128] and the cathodic reduction peak  $C_1$  is practically missing. Under illumination the shift of the anodic peak  $A_1$  becomes smaller and the reduction peak  $C_1$  appears in the cyclic voltammogram at a potential more cathodic than  $E_{fb}$ . This behaviour indicates clearly that in this case the “switch” process between the LM and EM states of PANI is influenced not only by the presence of the thin SiO<sub>2</sub> layer but also by the electronic band structure of p-Si(111) substrate. It should be mentioned that the illumination does not influence the electrochemical behaviour of PANI on Au(111) and the behaviour of the layer remains unchanged.



**Figure 4.24** Electrochemical behaviour of PANI ( $Q \sim 2\text{mC cm}^{-2}$ ) on Au(111) and on p-Si(111) in 0.5M H<sub>2</sub>SO<sub>4</sub>;  $|dE/dt| = 5\text{mV s}^{-1}$ .

Information about the substrate influence on the kinetics of the LM-EM transition can be obtained also by potentiostatic transient measurements [132]. Typical current transients measured by switching the electrode potential from  $E = 0\text{ V}$  (corresponding to fully reduced

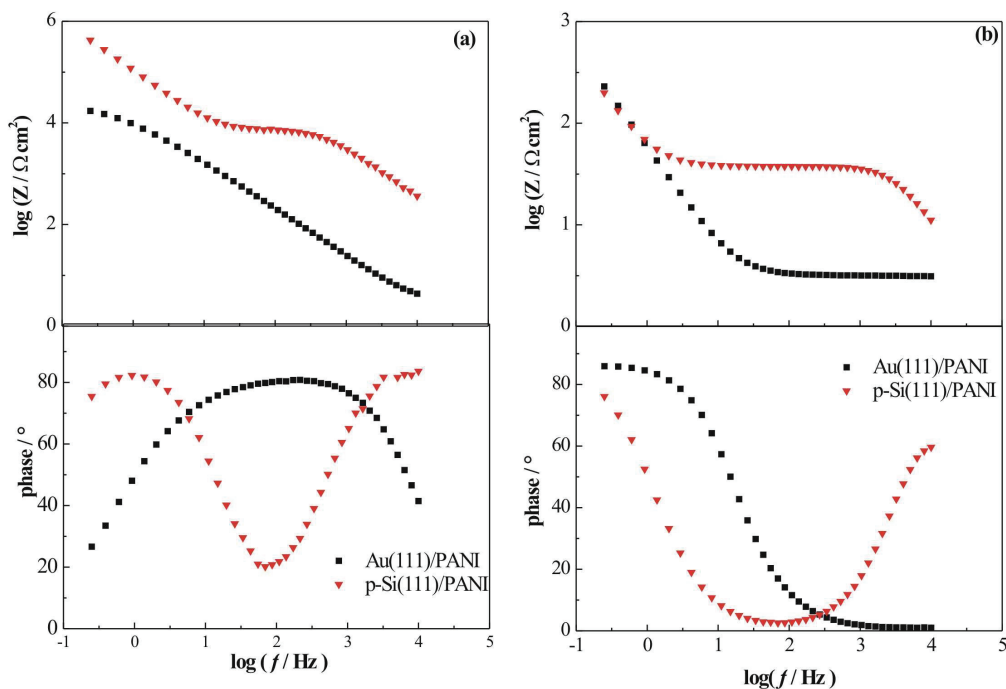
LM state) to  $E = 0.64$  V (corresponding to oxidized EM state) are presented in Figure 4.25. The current transient of the PANI layer electrodeposited on Au(111) shows that the LM-EM transition is relatively fast and is completed within 100 ms (Figure 4.25a). In contrast, the transition from the LM to the EM state of the PANI layer on p-Si(111) is much slower (Figure 4.25b) due to impeded charge transfer processes at the p-Si(111)/PANI interface.



**Figure 4.25** Potentiostatic current transients, obtained during switching of the potential from 0V to 0.64V on PANI layers ( $Q \sim 2 \text{mC cm}^{-2}$ ) deposited on (a): Au(111) and (b): p-Si(111).

The steady state properties of the LM and EM forms of electrodeposited PANI films were studied by electrochemical impedance spectroscopy. In order to achieve a full transformation of both PANI forms, the impedance measurements were performed after long time polarization (about 5 min) at the corresponding electrode potential. Figure 4.26 shows typical impedance spectra of electrodeposited PANI films measured in the dark in an aniline free 0.5M  $\text{H}_2\text{SO}_4$  solution at electrode potentials  $E = 0$  V and  $E = 0.64$  V. The insulating LM and the conducting EM states are clearly distinguishable from their impedance spectra. The results obtained on Au(111) substrates are similar to those reported previously for polycrystalline gold electrodes [132]. The higher impedances observed at high and medium frequencies on p-Si(111) are related to the contributions of the space charge layer in the silicon substrate and of the anodic  $\text{SiO}_2$  film at the p-Si(111)/PANI interface.

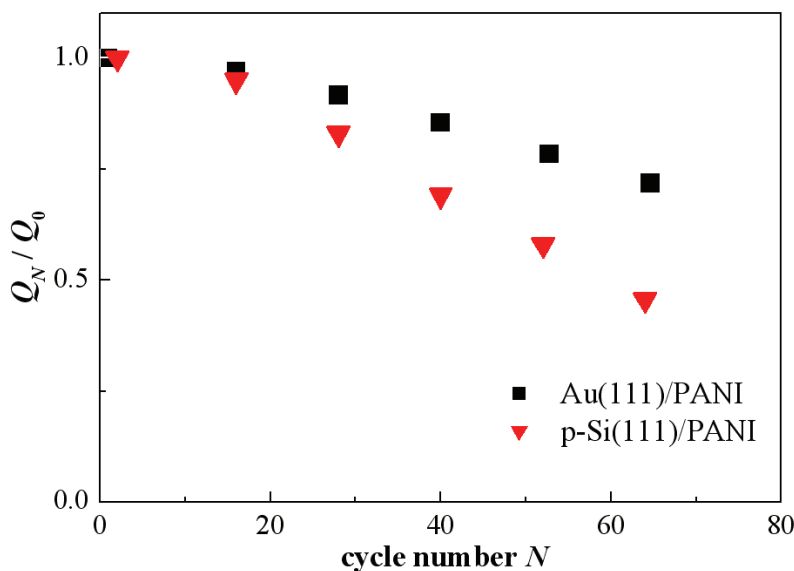
The electrochemical stability of electrodeposited PANI layers was characterized by continuous potentiodynamic cycling in the potential range  $0 \text{ V} < E < 1 \text{ V}$ . As a measure for the electrochemical stability was used the ratio between the redox charge  $Q_N$  of the  $N^{\text{th}}$  cycle and the initial redox charge  $Q_0$ .



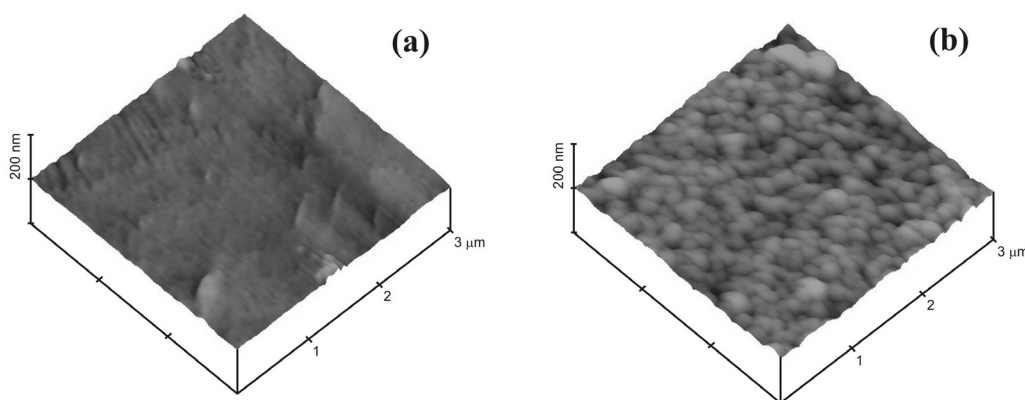
**Figure 4.26** Impedance spectra of PANI films ( $Q = 2.5 \text{ mC cm}^{-2}$ ) on Au(111) and p-Si(111) measured in 0.5M  $\text{H}_2\text{SO}_4$  at (a): 0V and (b): 0.64V (*ac*-amplitude 10mV).

Figure 4.27 shows the degradation ratio  $Q_N/Q_0$  as a function of the cycle number  $N$  for PANI layers with similar initial redox charges prepared by potentiodynamic deposition on Au(111) and p-Si(111). After 65 cycles the electrochemical activity of the PANI layer deposited on p-Si(111) is reduced by about 50 %, whereas the layer on Au(111) still possesses 75% of its efficiency. A relatively low electrochemical stability has been reported recently also for PANI layers electrodeposited on non-platinum metal substrates such as Ti, Ni, Al, Pb and SS, which similarly to Si undergo an anodic oxidation in the potential range of PANI deposition [133]. Therefore, the faster degradation rate observed during the potentiodynamic cycling of PANI layer deposited on p-Si(111) can be addressed to the weak adhesion of the polymer on the oxide covered silicon substrate.

The differences in the electrochemical behaviour of electrodeposited PANI films on Au(111) and p-Si(111) discussed above can be related also to the different morphology of the layers. Figure 4.28 shows the surface morphology of PANI layers deposited under potentiodynamic conditions on Au(111) and p-Si(111) substrates.



**Figure 4.27** Electrochemical stability of electrodeposited PANI layers on Au(111) and p-Si(111) during the continuous potentiodynamic cycling between 0 and 1V in 0.5M $H_2SO_4$  ( $|dE/dt| = 50 \text{ mV s}^{-1}$ );  $Q_0$  : initial redox charge;  $Q_N$  : redox charge of the  $N^{\text{th}}$  cycle.



**Figure 4.28** AFM images of PANI films ( $Q \sim 4 \text{ mC cm}^{-2}$ ) electrodeposited on (a): Au(111) and (b): p-Si(111) under potentiodynamic conditions ( $|dE/dt| = 50 \text{ mV s}^{-1}$ ).

As seen the PANI film on Au(111) is characterized by relatively compact structure and smooth surface (Figure 4.28a), which promote a rapid charge transfer through the polymer layer. In contrast, the PANI layer on p-Si(111) exhibits a globular structure and higher surface roughness (Figure 4.28b). In this case the charge transport between different domains in the PANI film is hindered. The observed surface morphologies could be attributed to different growth modes during the initial deposition stages of PANI on Au(111) and p-Si(111) as derived from the analysis of potentiostatic current transients (cf. Figures 4.16 and 4.17).

### 4.3 Nanoscale Modification of Gold Micro- and Nanostructures

In the first two sections of this chapter are presented studies related to the fabrication of gold nanogaps and nanocontacts by narrowing a micrometer scale distance between two opposite gold microelectrodes using gold electrodeposition from the non-toxic gold electrolyte solution (5mM  $\text{HAuCl}_4$  + 42mM  $\text{Na}_2\text{S}_2\text{O}_3$  + 42mM  $\text{Na}_2\text{SO}_3$ ). This electroplating solution was selected due to its compatibility with the lithographic resist used for the preparation of gold microelectrodes as already mentioned in the experimental section 3.1. Of particular importance for the development of optimal polarization routines for preparation of nanogaps and nanocontacts is the knowledge of evolution of surface roughness during the gold electrodeposition. An AFM study of the evolution of surface morphology during the electrodeposition of gold on Au(111) is presented in section 4.3.1. The results on the preparation and properties of gold nanocontacts and nanogaps are discussed in section 4.3.2. The last section 4.3.3 presents study on the bridging of electrochemically fabricated Au-Au nanogaps by electrodeposition of polyaniline.

#### 4.3.1 AFM study of surface morphology during gold electrodeposition on Au(111)

A typical cyclic voltammogram for electrodeposition of gold in the system Au(111)/5mM  $\text{HAuCl}_4$  + 42mM  $\text{Na}_2\text{S}_2\text{O}_3$  + 42mM  $\text{Na}_2\text{SO}_3$  is shown in Figure 4.29.

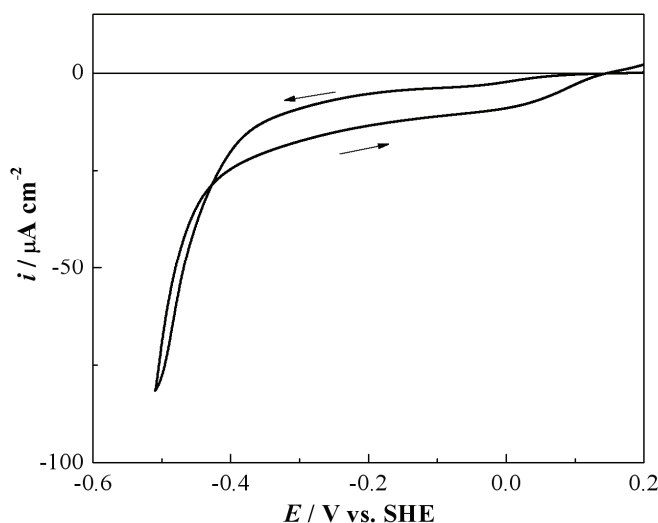
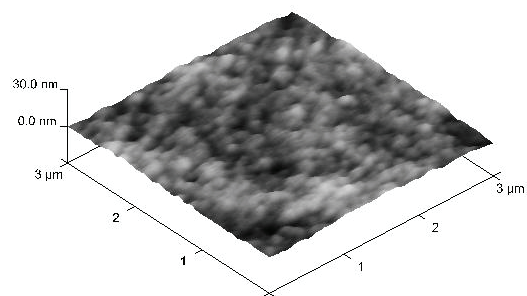
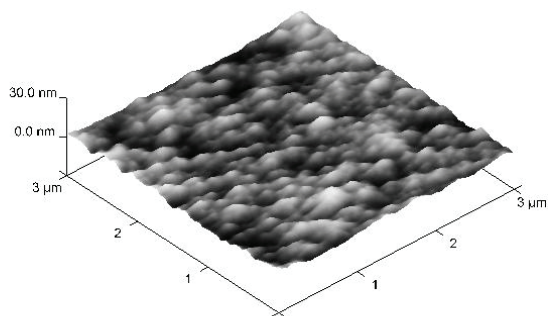


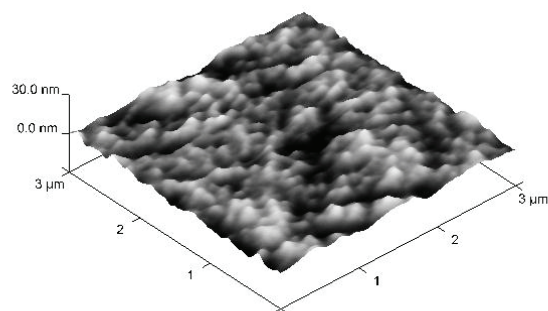
**Figure 4.29** Cyclic voltammogram of Au electrodeposition in the system Au(111)/5mM  $\text{HAuCl}_4$  + 42mM  $\text{Na}_2\text{S}_2\text{O}_3$  + 42mM  $\text{Na}_2\text{SO}_3$ ;  $|dE/dt| = 1 \text{ mV s}^{-1}$



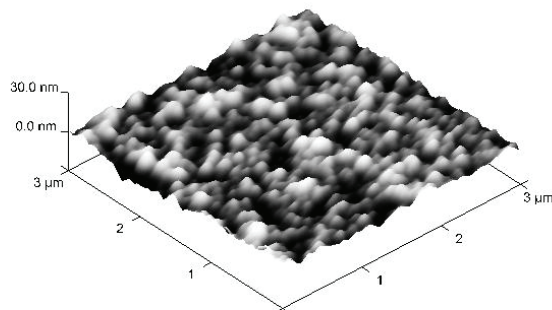
(a)



(b)



(c)



(d)

**Figure 4.30** AFM images showing surface morphology obtained after electrodeposition of Au in the system Au(111)/5mM  $\text{HAuCl}_4$  + 42mM  $\text{Na}_2\text{S}_2\text{O}_3$  + 42mM  $\text{Na}_2\text{SO}_3$  at  $E = -0.26$  V for (a): 300s, (b): 600s, (c):900s and (d): 1200s.

A cathodic deposition current is observed at electrode potentials below 0.15 V vs SHE. At more negative electrode potentials  $E < -0.4$  V starts the hydrogen evolution reaction, which takes place simultaneously with the gold electrodeposition process. Therefore, in order to avoid possible influences of hydrogen evolution on deposit morphology, the AFM studies of gold electrodeposition have been performed at a relatively low cathodic potential  $E = -0.26$  V.

Figure 4.30 shows AFM images of surface morphology obtained after electrodeposition of gold on Au(111) at  $E = -0.26$  V for different deposition times. Typical cross sections from the images shown in Figure 4.30 are presented in Figure 4.31. As seen under these deposition conditions the growth morphology is characterized by the formation of growing mounds, which become higher at longer deposition times. This mound morphology is very similar to that observed previously by in-situ STM imaging of gold electrocrystallization on Au(111) from a cyanide-based electrolyte solution [134].

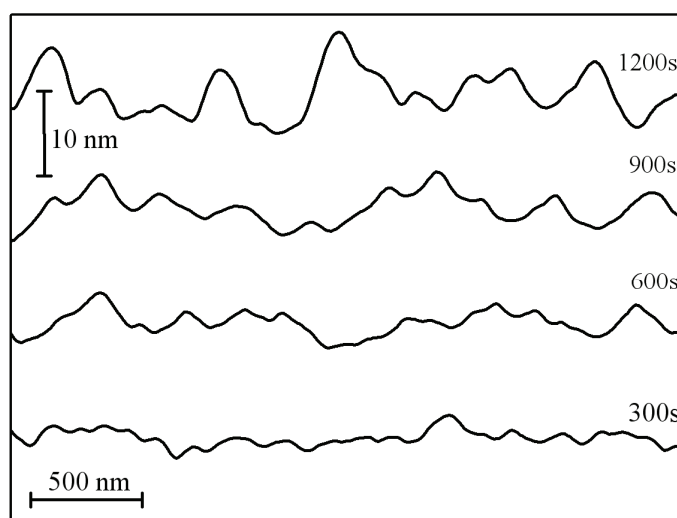


**Figure 4.31** Line scans from AFM images shown in Figure 4.30.

The formation of multilayer mounds is observed frequently also in many cases of homoepitaxial growth on single crystal substrates under UHV conditions [135]. This behaviour is related usually to the existence of the so-called Ehrlich-Schwoebel barrier (step-edge barrier) located at the step edges so that the diffusing adatoms on a terrace go more easily to the upper step than to the lower step. Therefore, the Ehrlich-Schwoebel barrier can



influence significantly the surface diffusion and can lead to the formation of the observed multilayer mounds.

The evolution of surface morphology shown in Figure 4.30 has been characterized applying the so-called dynamic scaling analysis described in section 2.1.2.2. AFM images with scan sizes ranging between  $500 \times 500$  and  $3000 \times 3000$  nm were analyzed statistically in order to determine the scaling exponents. Figure 4.32 shows the obtained experimental dependencies of the surface roughness  $w$  on the scale length  $L$  as  $\log w$  vs.  $\log L$  plots. As seen, for each deposition time the  $w(L)$ -dependence is characterized by a critical scale length  $L_c$ , above which the surface roughness  $w$  reaches a constant saturated value  $w_s$ . At relatively small scale lengths ( $L \ll L_c$ ) the surface roughness  $w$  increases linearly with  $L$  in accordance with the dynamic scaling concept. However, in this scale range  $w$  depends also on the deposition time, which shows that the evolution of the surface roughness follows an anomalous scaling behaviour and the experimental data in Figure 4.32 have to be analyzed using the relations (2.29') and (2.30').

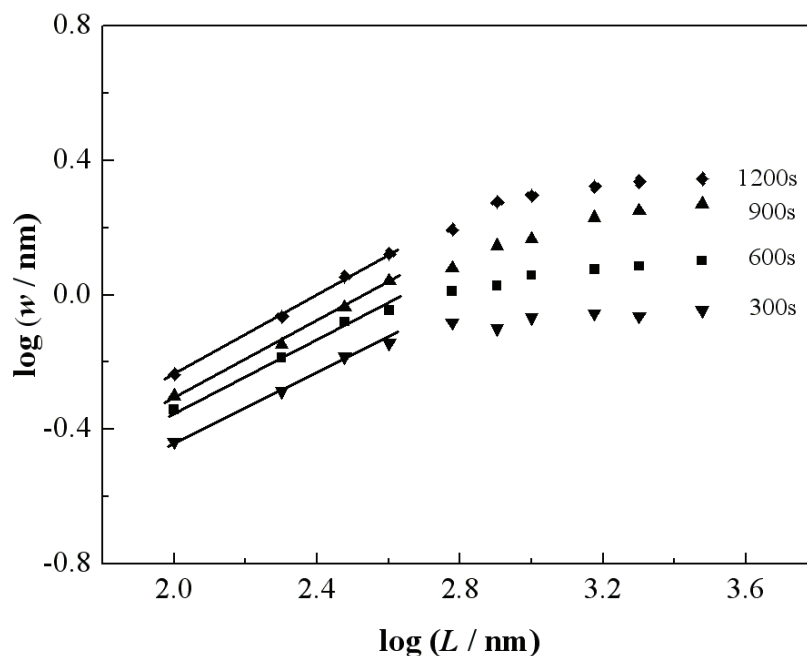


**Figure 4.32**  $\log w$  vs.  $\log L$  for Au electrodeposition at  $E = -0.26\text{V}$  in the system  $\text{Au}(111)/5\text{mM H AuCl}_4 + 42\text{mM Na}_2\text{S}_2\text{O}_3 + 42\text{mM Na}_2\text{SO}_3$  at different electrodeposition times obtained from dynamic scaling analysis of AFM images.

A roughness exponent  $H = 0.6 \pm 0.05$  was estimated from the slopes of the linear parts of experimental  $\log w$  vs.  $\log L$  plots. Figure 4.33 shows the local surface roughness at  $L = 200$  nm as a function of the deposition time in a  $\log w$  vs.  $\log t$  plot. From the slope of the observed linear dependence could be estimated a local growth exponent  $\beta_{\text{loc}} = 0.35 \pm 0.05$ .

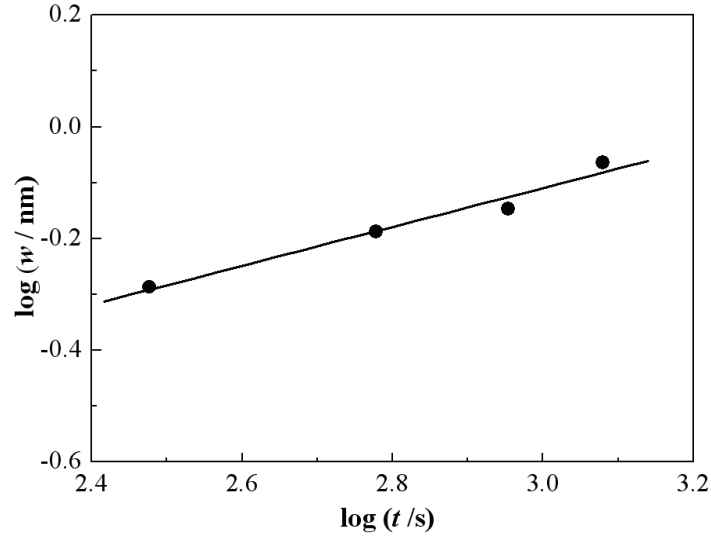


**Figure 4.33** Time dependence of the local surface roughness ( $L = 200$  nm).

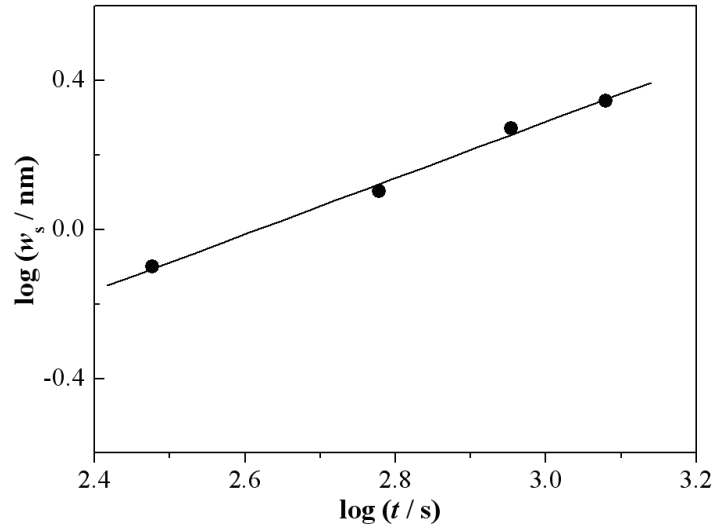


**Figure 4.34** Time dependence of the saturated surface roughness.

A logarithmic plot of the time dependence of saturated surface roughness  $w_s$  (for  $L \gg L_c$ ) is shown in Figure 4.34. The slope of the observed straight line gives a value

of  $\beta + \beta_{\text{loc}} = 0.58 \pm 0.05$ , which corresponds to a value of the growth exponent of  $\beta = 0.23 \pm 0.05$ .

In order to obtain more information about the mechanism of surface roughening during gold electrodeposition the experimentally estimated values of scaling exponents  $H$  and  $\beta$  have been compared to those predicted by various theoretical models (cf. Table 2.2). The comparison shows that the surface roughness evolution resulting from the performed gold electrodeposition can be described by model involving surface diffusion and step growth characterized by the scaling exponents  $H = 2/3$  and  $\beta = 1/5$  [61,62].

These results are consistent with the observed mound morphology and show that due to the relatively high surface mobility of gold the smoothening of the growing surface by surface diffusion contributes significantly to the evolution of the surface roughness during the electrodeposition of gold in the investigated system.

#### **4.3.2 Preparation and properties of gold nanogaps and nanocontacts**

As already mentioned above, the studies on preparation of gold nanogaps and nanocontacts were performed on pairs of planar opposite gold microelectrodes fabricated on silicon chips by conventional optical lithography (cf. section 3.2). Preliminary experiments on gold electrodeposition on such (as fabricated) gold microelectrodes have shown that the deposition process starts with a formation of 3D gold clusters only on preferential sites of the electrode surface (Figure 4.35a). At longer deposition times the coalescence of the growing gold clusters leads to formation of an inhomogeneous deposit exhibiting a significant surface roughness (Figure 4.35b). The observed growth morphology is rather surprising because in this case the gold electrodeposition takes place on a native gold substrate. This behaviour indicates that after the lithographical preparation the surface of gold microelectrodes is contaminated and the gold deposition process starts similarly as on a foreign substrate by formation of isolated 3D gold clusters.

A contamination free gold surface can be obtained by cycling the electrode potential in the region of formation and reduction of gold oxide in sulfuric acid solution [136]. In Figure 4.36

are shown cyclic voltammograms obtained on the lithographically prepared gold microelectrodes in 0.1M H<sub>2</sub>SO<sub>4</sub>.

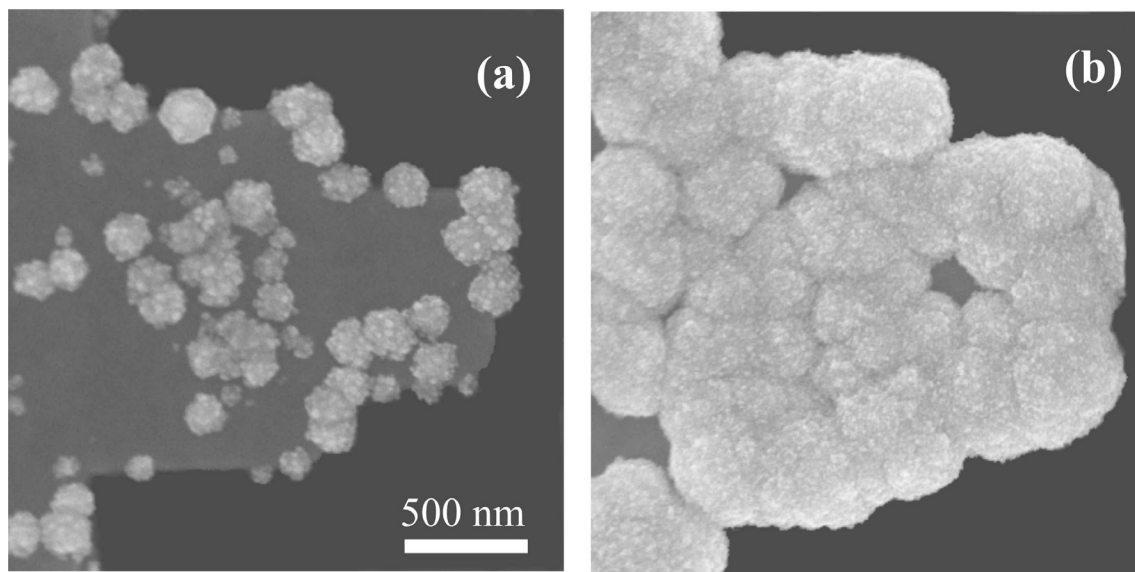


**Figure 4.35** SEM images of gold deposited on lithographically prepared gold microelectrodes from 5mM H<sub>AuCl</sub><sub>4</sub> + 42mM Na<sub>2</sub>S<sub>2</sub>O<sub>3</sub> + 42mM Na<sub>2</sub>SO<sub>3</sub> at E = -0.2V for (a): 30s and (b): 300s.

The voltammetric peaks A<sub>1</sub> and C<sub>1</sub> observed in the potential range 0.5V – 0.9V correspond to the adsorption and desorption of sulfate ions, whereas the peaks A<sub>2</sub> and C<sub>2</sub> are related to the formation and reduction of surface gold oxide. As seen, each consecutive cycle activates the surface of the gold microelectrodes, which is reflected in the increase of the adsorption/desorption peaks A<sub>1</sub>/C<sub>1</sub> and oxidation/reduction peaks A<sub>2</sub>/C<sub>2</sub>. However, due to the phase transformations occurring during the gold oxidation/reduction the observed activation after continuous cycling is attributed not only to a decontamination of the electrode surface but also to a significant increase of the surface roughness [136]. This roughening of the electrode surface can be critical for the preparation of nanogaps and nanocontacts by gold electrodeposition. Therefore, before the gold electrodeposition, in order to obtain a reproducible contamination free gold surface with a minimal roughness, the following polarization routine has been applied as an electrochemical activation procedure. After an initial activation applying one single potential cycle in the potential range 0.5V – 1.7V, the gold microelectrodes were conditioned further by a continuous potential cycling for 10 min with a scan rate  $|dE / dt| = 50 \text{ mV/s}$  only in the range of sulfate adsorption-desorption (0.5V – 0.9V).

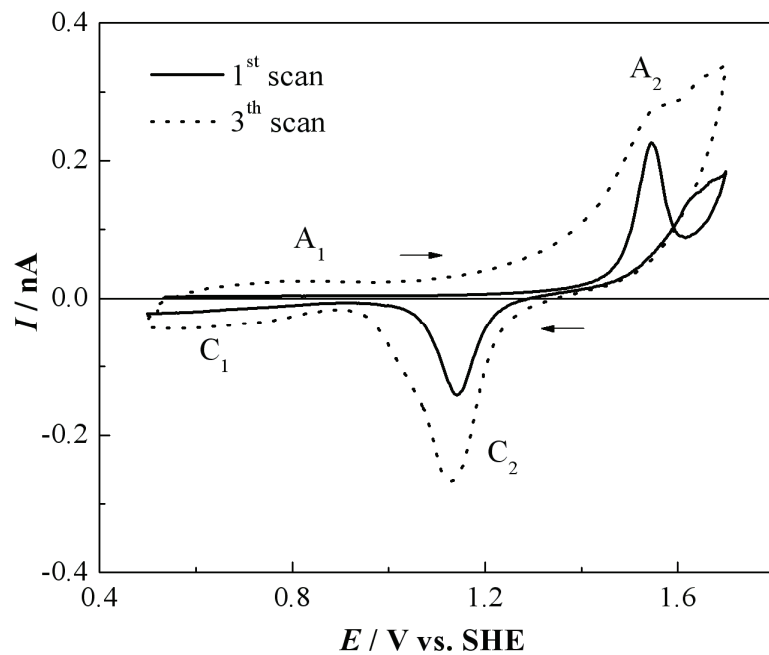


**Figure 4.36** Cyclic voltammograms of an Au microelectrode in 0.1M H<sub>2</sub>SO<sub>4</sub> ( $|dE/dt| = 50 \text{ mV s}^{-1}$ ).

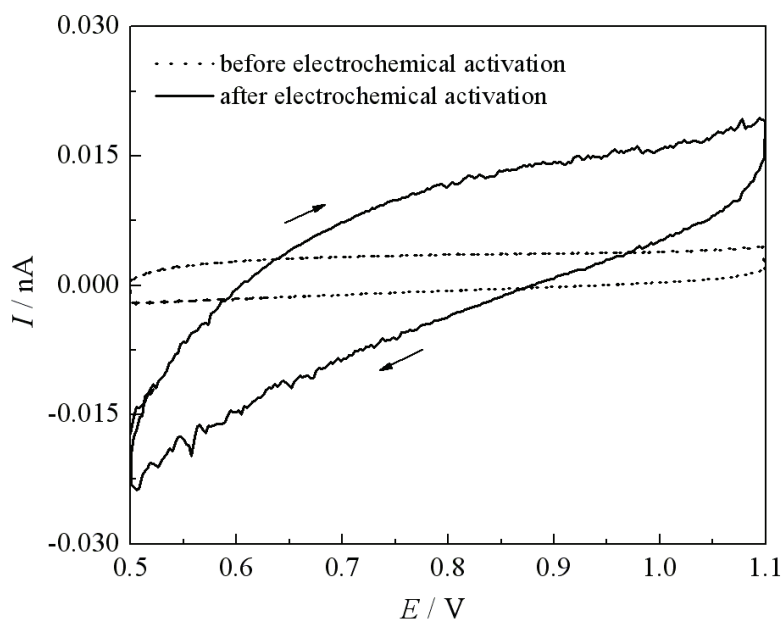


**Figure 4.37** Cyclic voltammograms of an Au microelectrode in 0.1M H<sub>2</sub>SO<sub>4</sub> before (dotted line) and after (solid line) electrochemical activation ( $|dE/dt| = 50 \text{ mV s}^{-1}$ ).

The activation of lithographically prepared gold microelectrodes after this pretreatment is illustrated by the cyclic voltammograms in Figure 4.37. Only freshly activated

microelectrodes showing a reasonable electrochemical response have been used for the preparation of nanogaps and nanocontacts via gold electrodeposition described in the following.

The narrowing of the initial micrometer gap has been carried out by controlled potentiostatic electrodeposition of gold applying different deposition potentials  $E_1$  and  $E_2$  on both working microelectrodes (WE1 and WE2) and monitoring the current changes with the time. Due to the applied potential difference  $\Delta E = E_1 - E_2$ , the currents at both electrodes include contributions of the corresponding deposition currents and of the conductance current flowing between the two electrodes. The conductance current allows a distinguishing of various electrode separations, which cause characteristic symmetric current behaviour of both working microelectrodes.

At short deposition times the current  $I$  at both microelectrodes is in the pA range and is determined by the electrodeposition of gold. With increasing deposition time the electrode separation decreases and for sufficiently long times becomes only several nanometers. In this time range the current increases up to several hundred nA due to a direct electron tunnelling between both microelectrodes. The further deposition leads to formation of different nanoscale gold contacts and the current increases in a stepwise fashion in the  $\mu\text{A}$  range until a macroscopic bulk gold contact is formed between the two electrodes. The stepwise increase of the conductance current is more pronounced at relatively low cathodic deposition potentials, where the gold deposition occurs by relatively low deposition rate. At high cathodic deposition potentials the conductance current increases abruptly due to the very fast deposition rate. This behaviour is illustrated in Figure 4.38 showing two conductance current traces recorded at two different deposition potentials ( $E_1 = -0.5\text{V}$  and  $E_1 = -0.1\text{V}$ ) and  $\Delta E = 25\text{ mV}$ . Due to the relatively high deposition rate at  $E_1 = -0.5\text{V}$ , the steps in the conductance current appear at very short times close to the limit of the measurement equipment and it is difficult to control the formation of the nanocontacts. In contrast, at  $E_1 = -0.1\text{V}$  the gold deposition occurs slowly and the conductance current steps due to formation of gold nanocontacts can be clearly distinguished.

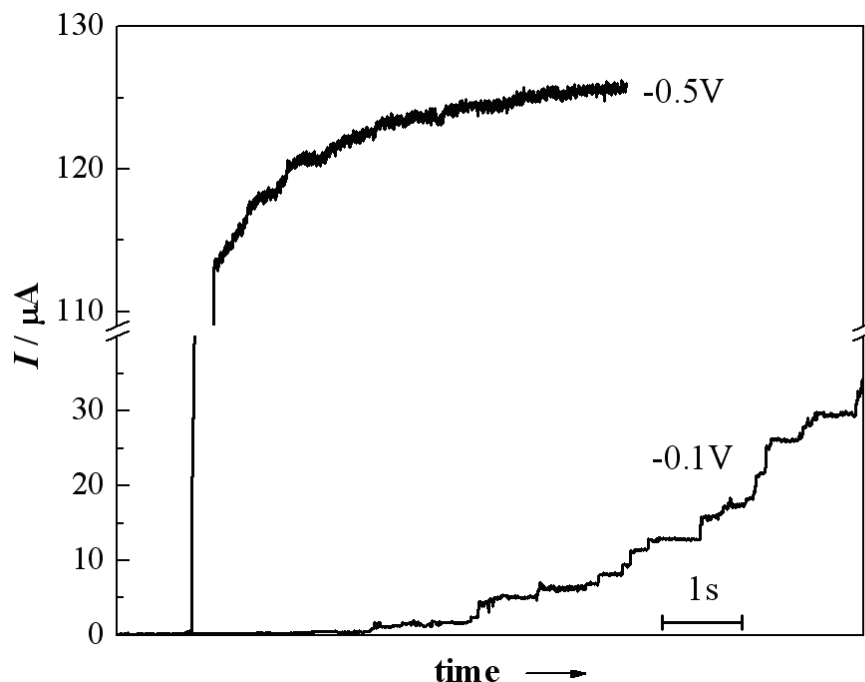


**Figure 4.38** Conductance current transients obtained during contact formation between WE1 and WE2 via electrodeposition of gold at  $E_1 = -0.1\text{V}$  and  $-0.5\text{V}$  in  $5\text{mM HAuCl}_4 + 42\text{mM Na}_2\text{S}_2\text{O}_3 + 42\text{mM Na}_2\text{SO}_3$  ( $\Delta E = 25\text{mV}$ ).

Figure 4.39 shows typical SEM images of electrode pairs modified by gold electrodeposition at different deposition potentials. The gold electrodeposits obtained at relatively low cathodic potentials (Figs. 4.39b and 4.39c) are smooth and follow the initial geometry of microelectrodes (Figure 4.39a). In contrast, the deposits obtained at a relatively high cathodic potential  $-0.5\text{V}$  (Figure 4.39d) show very inhomogeneous and rough growth morphology, which can be attributed to the high deposition rate and/or to the hydrogen evolution occurring in this potential range simultaneously with the gold deposition. The electrochemical measurements and SEM observations reveal that a better control of the electrode separation and the formation of various nanocontacts can be achieved by gold electrodeposition at relatively low cathodic potentials.

However, at potentials more positive than  $-0.15\text{V}$  the deposition process is too slow and the bridging of the initial  $2\text{ }\mu\text{m}$  gap takes several hours. Therefore, the nanoscale modification of the gaps between the electrodes has been performed applying the following two-step electrodeposition routine. In a first step the electrode separation was reduced to a tunnelling distance of several nanometers by gold electrodeposition at a relatively high cathodic

potential (typically  $-0.2$  or  $-0.3\text{V}$ ), where the deposit morphology is still smooth (cf. Figs. 4.39b and 4.39c). After reaching a tunnelling current in the range of  $10\text{-}20\text{ nA}$  the deposition potential was switched to  $-0.1\text{V}$  and the conductance current during the slow gold deposition at this potential was monitored.

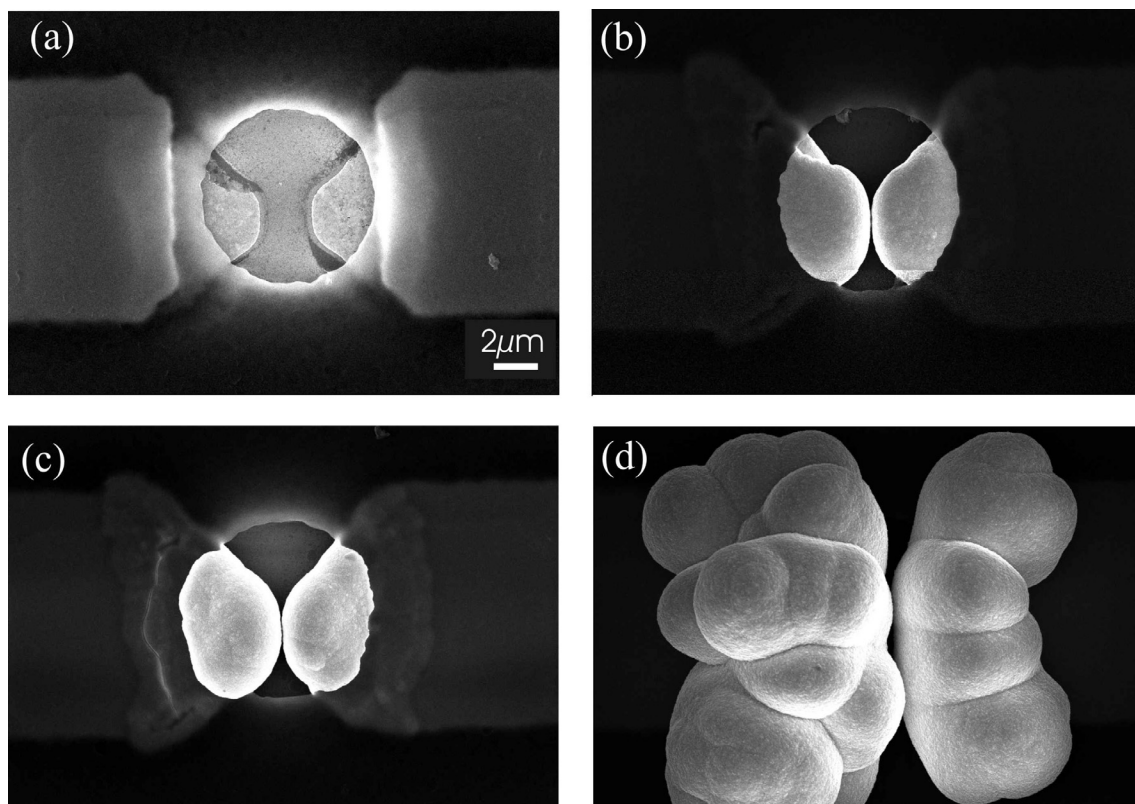


**Figure 4.39** SEM images of (a): unmodified gold electrode pair; electrode pairs modified by gold electrodeposition in  $5\text{mM HAuCl}_4 + 42\text{mM Na}_2\text{S}_2\text{O}_3 + 42\text{mM Na}_2\text{SO}_3$  at  $\Delta E = 25\text{mV}$ ;  $E_1 =$  (b):  $-0.2\text{V}$ ; (c):  $-0.3\text{V}$ ; (d):  $-0.5\text{V}$ .

The measured current was converted to conductance using the relation  $G = I / \Delta E$  after current correction for the contribution of the series resistance of the connecting leads. This resistance was estimated from the value of the current corresponding to the formation of the bulk micro size contact at  $E_1 = -0.5\text{V}$  (cf. Figure 4.38). The conductance  $G$  was normalized with the conductance quantum  $G_0 = 2e^2 / h = 77\text{ }\mu\text{S}$ . Figure 4.40 shows a typical time dependence of the normalized conductance  $G / G_0$  obtained during the modification of an electrode pair by gold electrodeposition at  $E_1 = -0.1\text{V}$  and  $\Delta E = 25\text{ mV}$ .



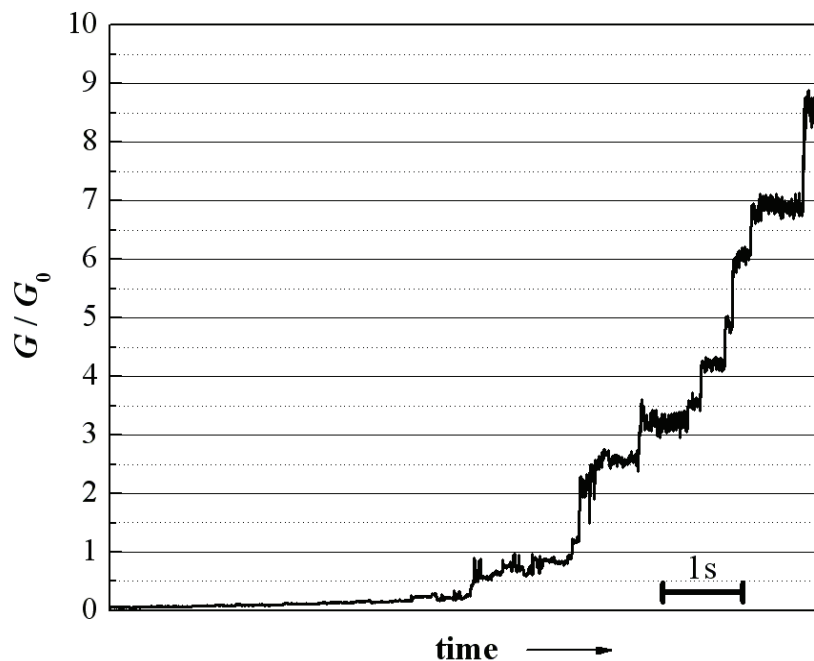


**Figure 4.40** Change of normalized conductance  $G/G_0$  with the time during contact formation between gold microelectrodes by gold electrodeposition at  $E_1 = -0.1\text{V}$  and  $\Delta E = 25\text{mV}$  in  $5\text{mM HAuCl}_4 + 42\text{mM Na}_2\text{S}_2\text{O}_3 + 42\text{mM Na}_2\text{SO}_3$ .

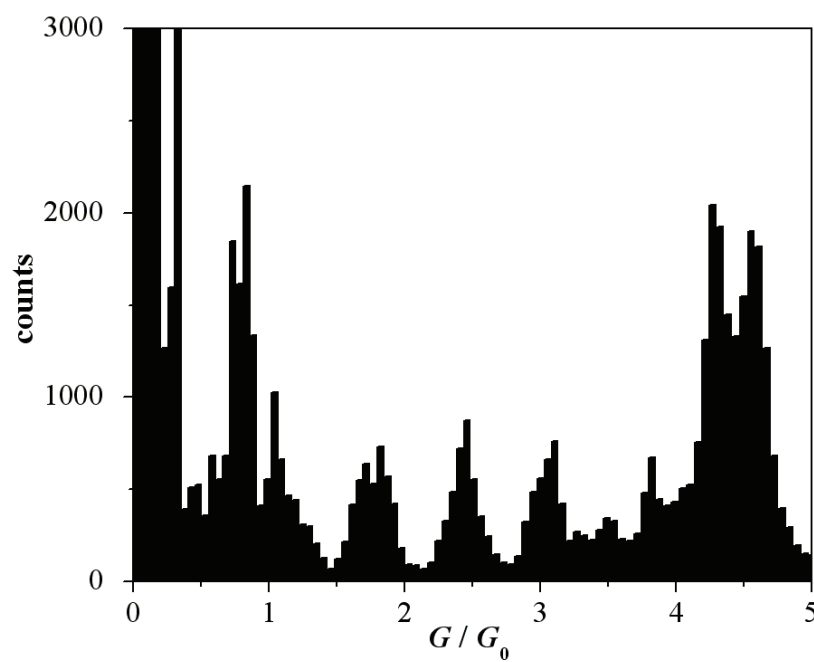


**Figure 4.41** Normalized conductance histogram determined from thirty conductance traces obtained during gold electrodeposition at  $E_1 = -0.1\text{V}$  and  $\Delta E = 25\text{mV}$ .

A sequence of conductance steps separated by plateaus with various lengths can be clearly distinguished in this case. Such stepwise increase of the conductance has been observed recently also in other electrochemical systems during the formation of nanoscale contacts by metal electrodeposition [85-88,90,91] and is usually related to the conductance quantization predicted by the Landauer formula (cf. Equations (2.35) and (2.36)). The conductance plateau at about  $1G_0$  corresponds to the formation of an atomic size contact. Figure 4.41 shows the conductance histogram determined from thirty conductance traces obtained during gold electrodeposition at  $E_1 = -0.1\text{V}$ . As seen, various well-defined sharp peaks appear near integer and fractional multiples of  $G_0$  in the histogram. The appearance of fractional multiples of  $G_0$  has been observed in all conductance traces obtained during gold electrodeposition at potentials in the range  $-0.3\text{V} < E < -0.1\text{V}$ .

An advantage of the used electrolyte is that the formed gold nanocontacts can be electrochemically dissolved by applying electrode potentials more anodic than the open circuit potential of gold in present system ( $E^{\text{OCP}} \approx 0.2\text{ V}$ ). However, at potentials higher than  $0.3\text{V}$  in this system an electrooxidation of thiosulphate can occur, which leads to a formation of a tightly bounded layer of elemental sulphur, blocking the electrode surface [137]. Therefore, the experiments on the dissolution of the gold nanocontacts have been performed at potential  $E_1 = 0.3\text{ V}$ .

As shown in Figure 4.42 during the dissolution process at this potential is observed a stepwise decrease of the conductance related to demolition of the nanocontacts. Figure 4.43 shows the conductance histogram obtained from the analysis of several conductance traces for gold electrodisolution at  $E_1 = 0.3\text{ V}$ . In the histogram appear again peaks near integer and fractional multiples of  $G_0$ , very similar to those observed in the case of gold electrodeposition (Figure 4.41). The only difference between the histograms obtained from the conductance traces for formation and demolition of nanocontacts is that in the second case the features at  $G < G_0$ , corresponding to the transition between the direct tunnelling and quantized conductance are not clearly manifested.

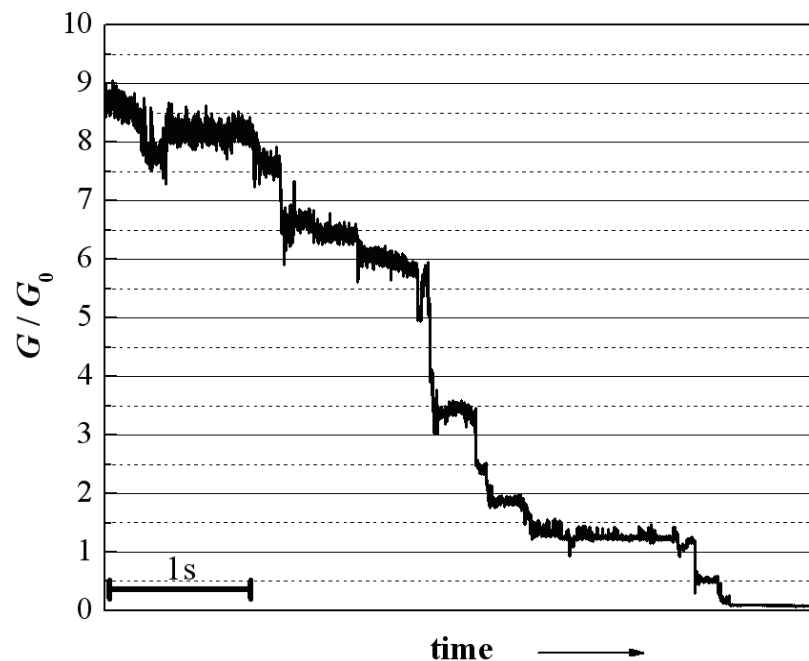


**Figure 4.42** Change of normalized conductance  $G/G_0$  with the time during gold contact dissolution at  $E_1 = 0.3\text{V}$  and  $\Delta E = 25\text{mV}$  in  $5\text{mM H AuCl}_4 + 42\text{mM Na}_2\text{S}_2\text{O}_3 + 42\text{mM Na}_2\text{SO}_3$ .

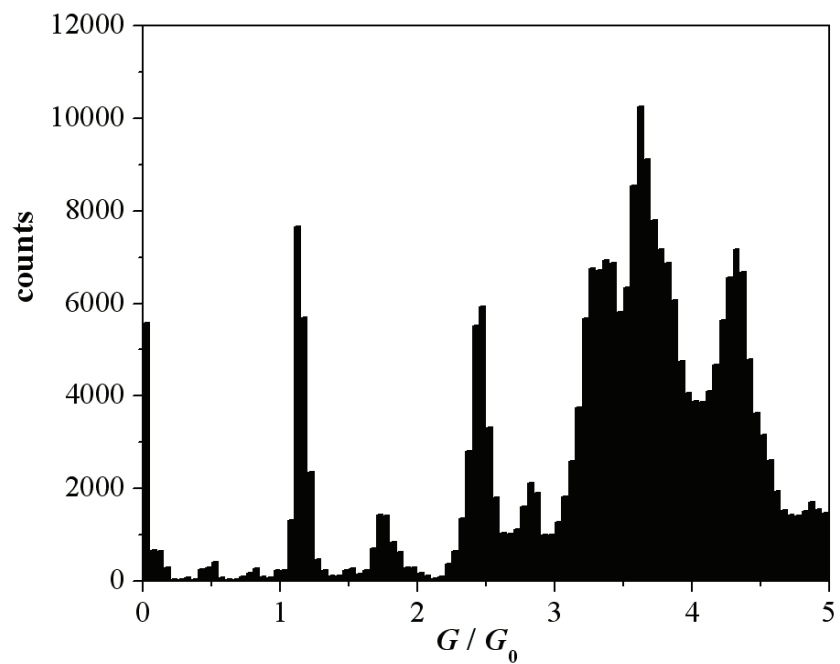


**Figure 4.43** Normalized conductance histogram determined from conductance traces obtained during gold electrodisolution at  $E_1=0.3\text{V}$  and  $\Delta E=25\text{mV}$ .

Fractional conductance quantization of gold nanocontacts has been observed in several electrochemical systems and has attracted recently much attention [138-142]. The experimental results show that the appearance of fractional conductance peaks in the conductance histograms is affected by both the electrolyte composition and the electrode potential. In the investigated systems the fractional conductance peaks are observed at negative electrode potentials ( $E < 0$  V vs.SHE). The fractional conductance quantization is discussed in terms of potential induced Fermi energy shift [139], potential induced adsorption of ions and organic molecules [140, 141] and potential induced surface stress changing the atomic configurations of nanocontacts [142]. In contrast to the above studies, the conductance histograms obtained in the present work (Figures 4.41 and 4.43) show fractional conductance peaks at both negative and positive electrode potentials ( $-0.3 \text{ V} < E < 0.3 \text{ V}$ ).

These results indicate that the hydrogen adsorption taking place only at negative potentials can not be considered as a single reason for the observed fractional conductance quantization in this case. Also, a possible adsorption of thiosulphate anions, which can occur at positive electrode potentials, can not be related to the fractional conductance steps observed in the overall potential range studied. The observed fractional conductance could be attributed to atomic rearrangements of gold nanocontacts taking place during the gold deposition/dissolution processes. However, a complete understanding of the origin of these phenomena needs further more detailed studies in various electrochemical systems.

As already mentioned, by nanoscale separations between the gold electrodes a tunnelling current in the nA ranges is observed. Figure 4.44 shows the increase of the tunnelling current, due to the gradual narrowing of the gap between the electrodes by gold electrodeposition at  $E_1 = -0.1 \text{ V}$  and  $\Delta E = 25 \text{ mV}$ . During the narrowing of the gap the tunnelling current increases also in a stepwise fashion but this behaviour is different from the conductance quantization behaviour discussed above. The step heights increase exponentially with the tunnelling current and are not equally spaced. Similar behaviour of the tunnelling current has been reported previously and has been attributed to the discrete nature of atoms, leading to discrete changes in the gap [85]. Possible contributions from specifically adsorbed species and water molecules present in the gap have been also discussed [143,144].

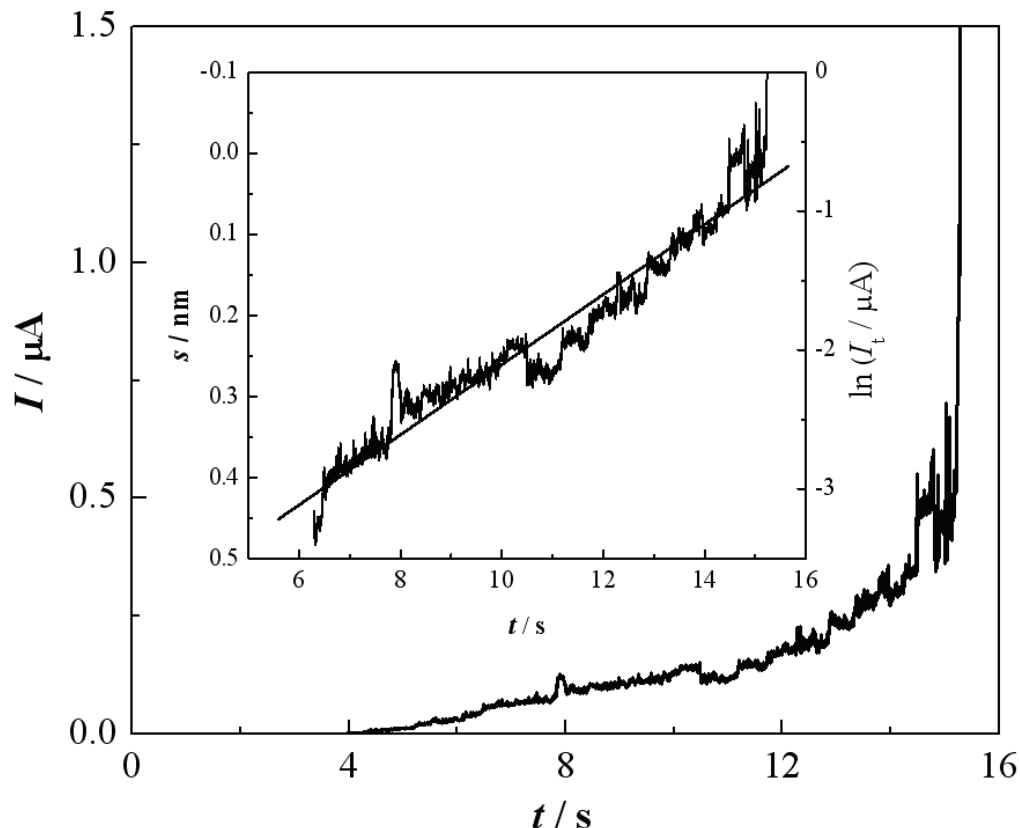


**Figure 4.44** Tunnelling current, measured during electrochemical gold deposition on gold microelectrode pair at  $E_1 = -0.1\text{V}$  and  $\Delta E = 26\text{mV}$  in  $5\text{mM H AuCl}_4 + 42\text{mM Na}_2\text{S}_2\text{O}_3 + 42\text{mM Na}_2\text{SO}_3$ ; (inset – correlation between the gap width  $s / \text{nm}$  and the tunnelling current  $I_t / \mu\text{A}$ ).

The gap width  $s$  corresponding to the tunnelling current shown as an inset in Figure 4.44 was estimated using Equation (2.38) with a decay constant  $k = 5 \text{ nm}^{-1}$  reported for gold in aqueous solution at gap resistances below  $10^8 \Omega$  [145]. Applying this evaluation by precise monitoring of the tunnelling current temporary stable molecular sized gaps between the two gold electrodes have been fabricated. Figure 4.45 displays an example of a stabilized molecular scale gap at  $E_1 = 0.2\text{V}$  and  $\Delta E = 26\text{mV}$ . The gap width fluctuates between two constant values and the height of the plateau is about  $0.16\text{nm} \pm 0.01$ . This value is close to the interlayer spacing of gold and the fluctuations are probably related to the dynamic equilibrium between deposition and dissolution of gold atoms.

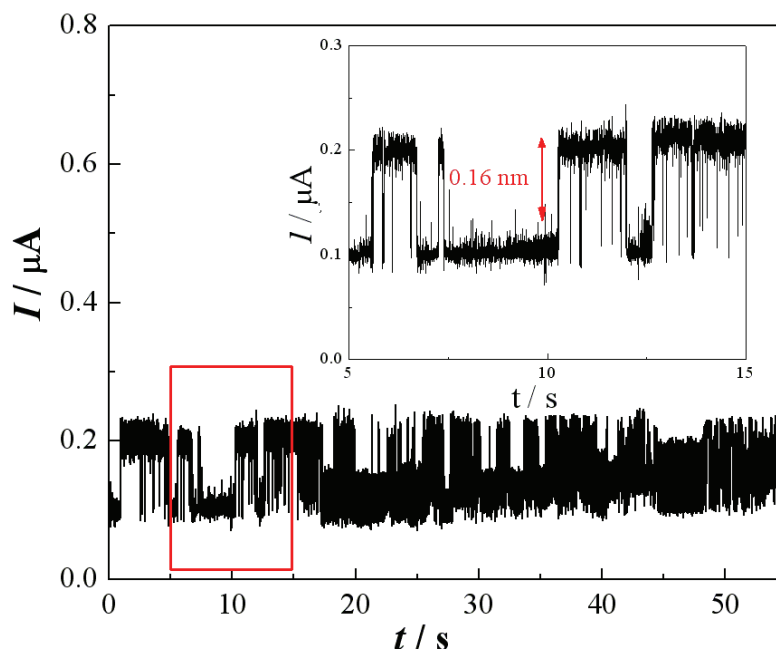


**Figure 4.45** Long term behaviour of temporary stabilized Au-Au gap at  $E_1=0.2\text{V}$  and  $\Delta E=26\text{mV}$  in  $5\text{mM H AuCl}_4 + 42\text{mM Na}_2\text{S}_2\text{O}_3 + 42\text{mM Na}_2\text{SO}_3$ .

As already mentioned, the stabilized gaps were bridged later via electrochemical deposition of PANI. Here it should be mentioned, that after exchanging of the electroplating gold bath with the aniline deposition solution the tunnelling between the electrodes does not occur any more. The absence of tunnelling in this case can be attributed to rearrangement of atoms at open circuit potential caused by the high mobility of gold and leading to an increase of the electrode separation.

### 4.3.3 Preparation and properties of polyaniline nanojunctions

It is well known that the growth morphology, structure and electronic and mechanical properties of electrodeposited polyaniline (PANI) films depend strongly on the applied deposition technique [146-149]. In the present study we have used different methods for PANI electrodeposition based on potential control, in order to establish optimal conditions for modification of the gold nanogaps, prepared as described in the previous section. The applied potentiodynamic (PD), pulse-potentiostatic (PP) and potentiostatic (PS) techniques are presented schematically in Figure 4.46. The PD technique (Figure 4.46a) is used most frequently for electrochemical synthesis of PANI. The applied potential is cycled with certain

rate in the potential window between 0V and 1V vs. SHE and the thickness of the polymer layer is determined by the number of performed potentiodynamic cycles (scans).

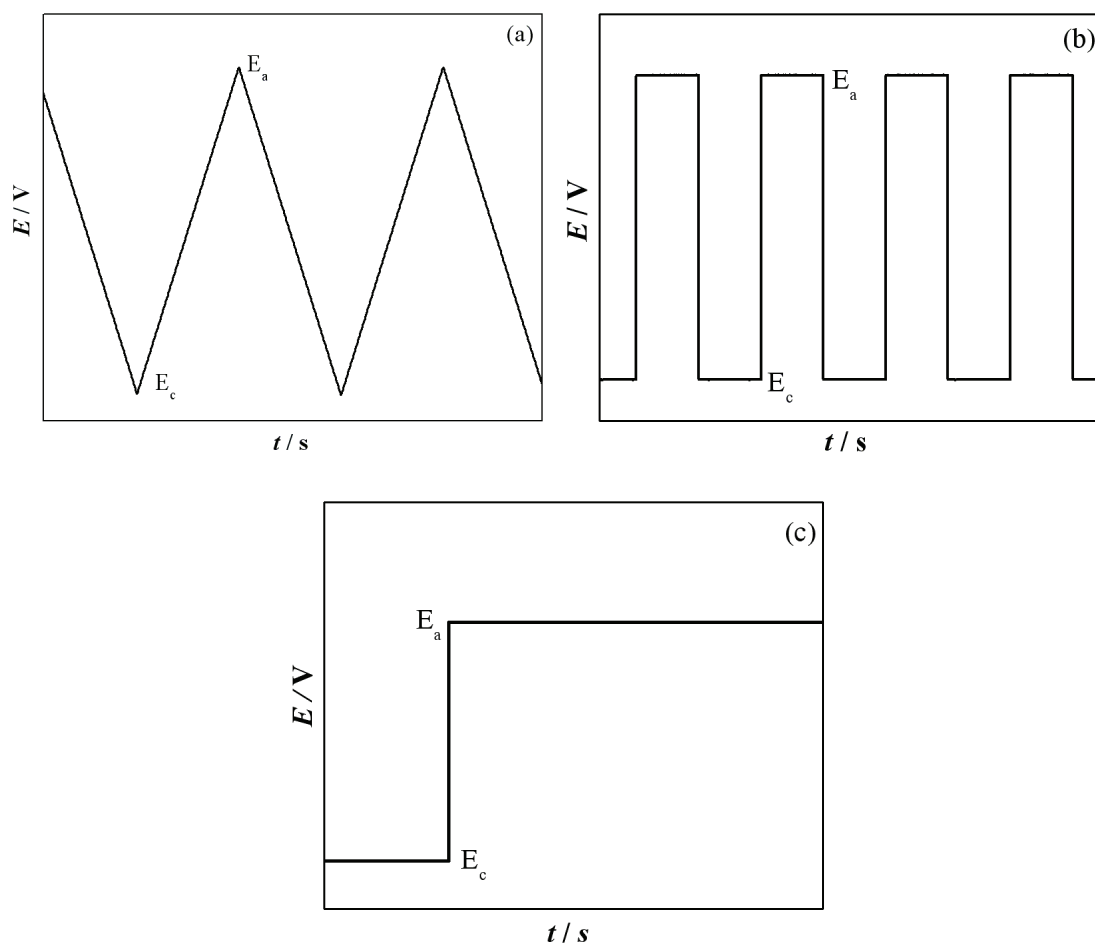


**Figure 4.46** Polarization routines for electrochemical deposition of PANI; (a): potentiodynamic (PD); (b): pulse-potentiostatic (PP); (c): potentiostatic (PS).

Using this technique can be prepared compact PANI films with relatively high electrochemical stability. Recently He et al. [25,26] applied successfully the PD deposition method also for bridging of a gold nanoscale gap by PANI junction. By the PP technique the potential is switched between certain anodic ( $E_a$ ) and cathodic ( $E_c$ ) values applying multiple potential pulses with definite time duration  $\tau$  (Figure 4.46b). In this case the thickness of the deposited polymer film is controlled by the number, amplitude and duration of applied pulses. The PANI layers synthesized using the PP technique exhibit good electrochemical stability comparable to that of PD deposited PANI films [146]. In the PS technique (Figure 4.46c) the applied anodic potential ( $E_a$ ) is constant during the all electropolymerization process.

Generally, the PANI films prepared by this method are less dense and exhibit lower electrochemical stability in comparison to the films prepared by the PD and PP techniques [146,148].

It should be noted, however, that the above discussion is related to PANI layers obtained by PD, PP and PS deposition on a microscopic scale and is not necessarily valid for the case of nanoscale PANI electrodeposition. The results obtained in this study by the preparation of Au-PANI-Au nanojunctions applying the PD, PP and PS electrodeposition techniques are presented in the following.

Figure 4.47 shows typical cyclic voltammograms obtained in various cycles (scans) during the modification of an electrochemically prepared Au-Au nanogap by PD electrodeposition of PANI. During the initial deposition cycles (before the formation of the polymer bridge) the cyclic voltammograms show only a relatively low Faraday current ( $|I| < 1 \text{ nA}$ ) caused by the electropolymerization and the electrochemical red/ox processes occurring in PANI deposit on the microelectrode (see the cyclic voltammogram of the 4<sup>th</sup> cycle in Figure 4.47a). As can be seen in Figure 4.47 however, small current oscillations appear in the reversed cathodic scan during the 5<sup>th</sup> deposition cycle. It can be suggested that these current oscillations are related to the formation of the first PANI contacts between the microelectrodes. The current behaviour observed in the cyclic voltammogram of the following 6<sup>th</sup> deposition cycle (Figure 4.47b) confirms this suggestion. The observed relatively large anodic current in the cyclic voltammogram is caused by the increased contribution of the conductance current due to the formed Au-PANI-Au junction. Once the Au-PANI-Au bridge is formed, a conductance current starts to flow due to the potential difference  $\Delta E = 15 \text{ mV}$  applied between the two electrodes. During the forward anodic scan the increase of the anodic current observed in the potential range  $0.2 \text{ V} < E_1 < 0.6 \text{ V}$  is related to the increasing conductance of the Au-PANI-Au junction due to the transition from the insulating LM state to the conducting EM state. At more positive electrode potentials ( $E_1 > 0.6 \text{ V}$ ) the conductance current behaviour during the anodic scan is determined by the transition from the conducting EM form to the insulating PN form. By the reversed cathodic scan the conductance current rises up to about 8 nA due to the reduction of PN to the EM state as well as due to the additional PANI electrodeposition leading to an increase of the size of the PANI bridge. The observed decrease of the conductance current during the cathodic scan at  $E_1 < 0.4 \text{ V}$  is caused by the reduction of PANI to the nonconductive LM state.



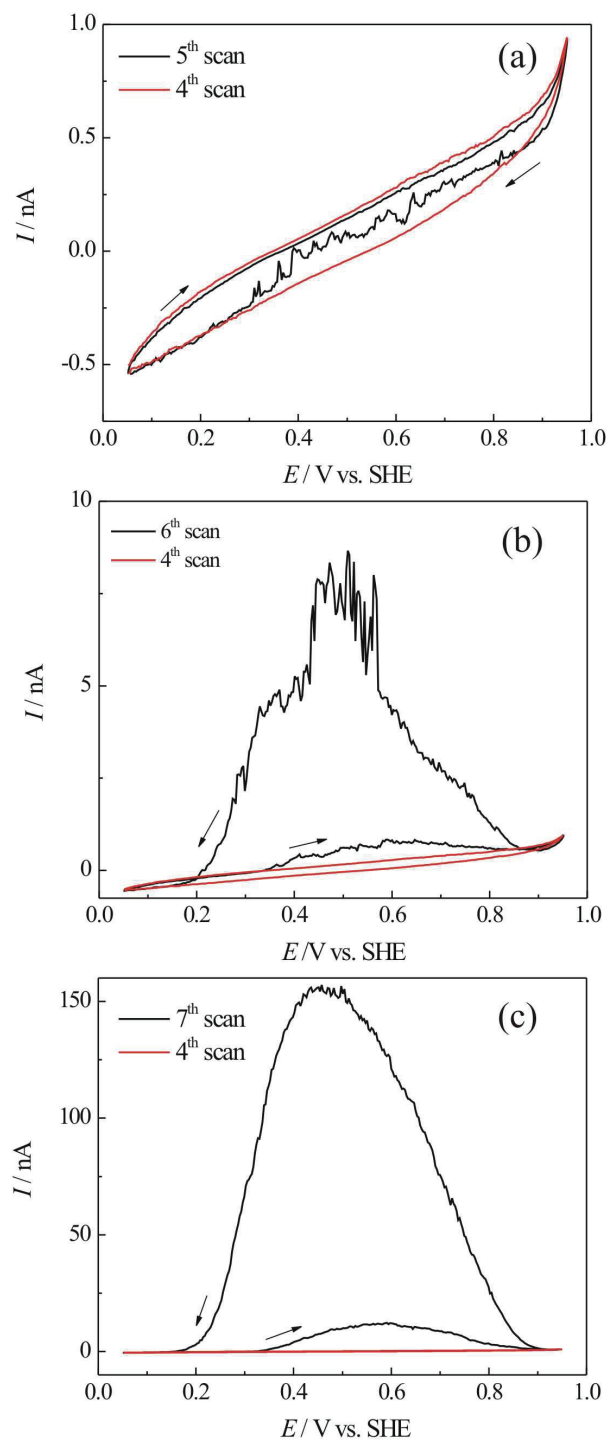


**Figure 4.47** PD formation of PANI junction between opposite gold microelectrodes separated by nanoscale gap ( $\Delta E=15\text{mV}$ ,  $|dE/dt| = 50 \text{ mV s}^{-1}$ ). Electrolyte solution 0.1M Aniline + 0.5M  $\text{H}_2\text{SO}_4$ .

As illustrated in Figure 4.47c, each following deposition scan leads to further increase of the size of the Au-PANI-Au junction causing enhancement of the conductance current. Figure 4.48 presents a SEM image of the Au-PANI-Au junction corresponding to the 7<sup>th</sup> deposition cycle in Figure 4.47c.

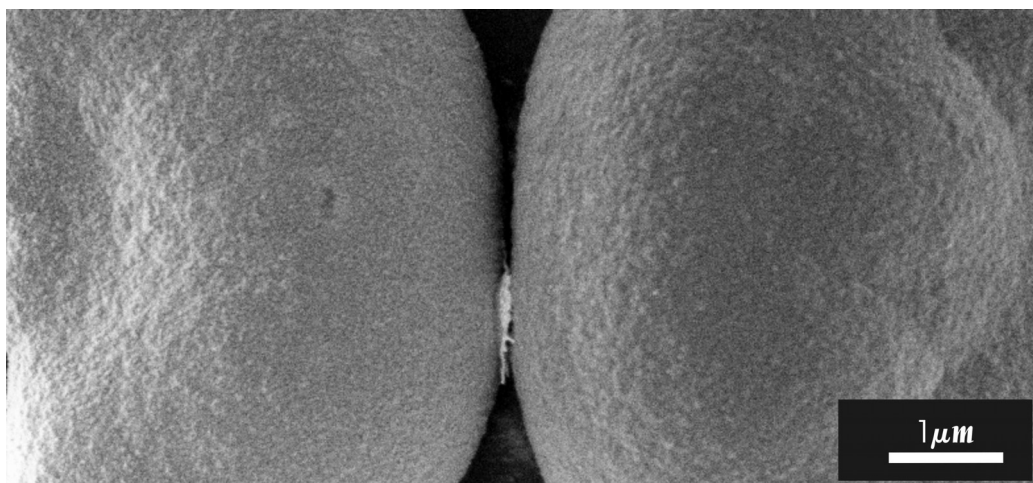


**Figure 4.48** SEM image of Au-PANI-Au junction obtained after 7 PD deposition scans.

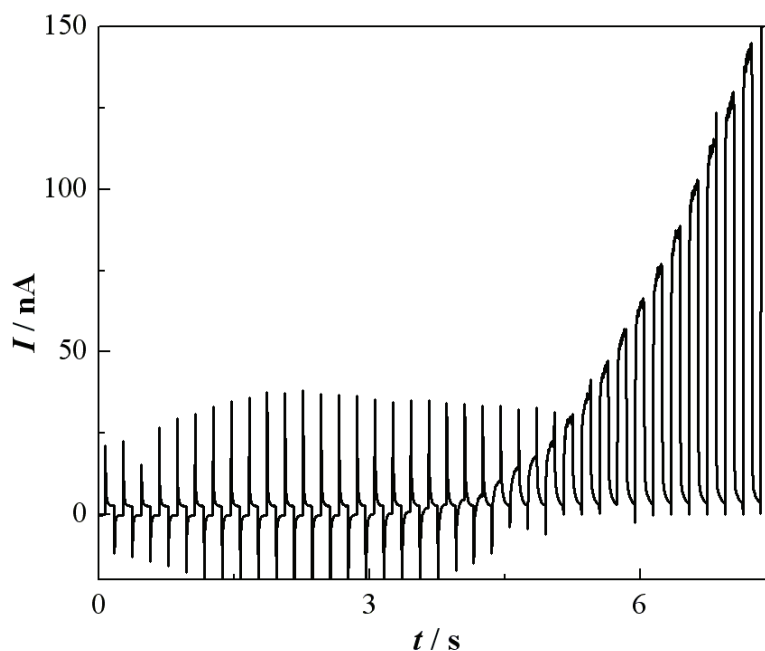


**Figure 4.49** PP formation of PANI junction between opposite gold microelectrodes separated by nanoscale distance; ( $\Delta E = 15$  mV,  $E_{1,a} = 1$  V,  $E_{1,c} = 0.2$  V,  $\tau = 0.1$  s). Electrolyte solution 0.1 M Aniline + 0.5 M  $H_2SO_4$ .

These results show that the obtained PANI bridges consists of a large number of polymer strands. Although a preparation of nanojunctions consisting only of several PANI strands by PD electrodeposition has been reported in the literature [25,26], the results presented above indicate that during the PD procedure it is difficult to control precisely the size of the polymer bridge.

Figure 4.49 represents a current trace recorded during the modification of an Au-Au nanogap by PP electrodeposition of PANI. Similarly as in the case of PD deposition, in the initial deposition stages (before the formation of the PANI bridge) are observed relatively low anodic and cathodic currents corresponding to the processes of electropolymerization and reduction of PANI deposit [150]. Due to the short potential pulses and the high polymerization rate during the PP electrodeposition, it is very difficult to determine the exact time of appearance of the polymer junction between the electrodes. Thus, the PP procedure can be applied for a fast deposition of larger PANI deposits with good stability but is not convenient method for preparation of nanoscale Au-PANI-Au junctions.

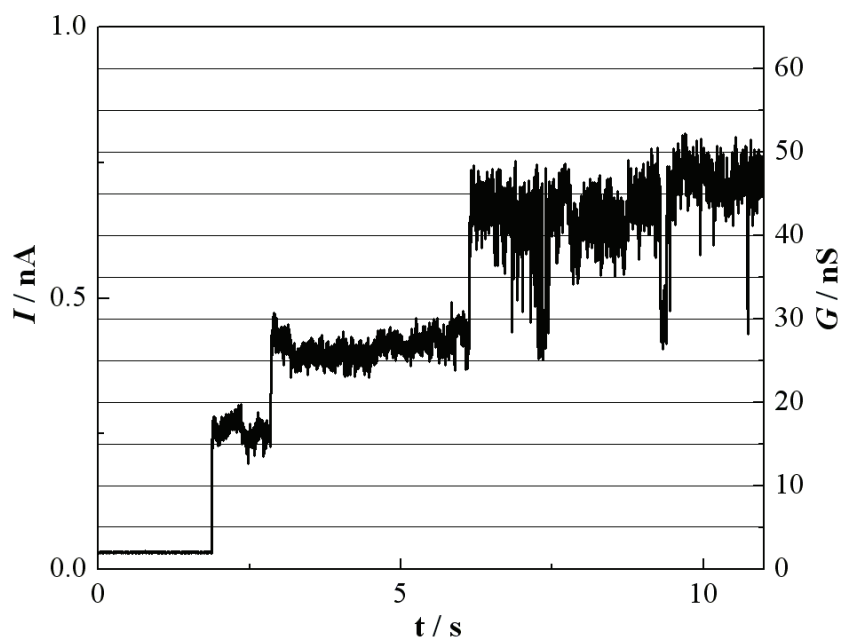


**Figure 4.50** PS formation of PANI junction between opposite gold microelectrodes separated by nanoscale distance ( $E_1 = 0.9 \text{ V}$ ,  $\Delta E = 15 \text{ mV}$ ) Electrolyte solution 0.1M Aniline + 0.5M  $\text{H}_2\text{SO}_4$ .

Figure 4.50 shows a typical current-time response obtained during the modification of an Au-Au nanogap by PS PANI deposition at  $E_1 = 0.9 \text{ V}$  and  $\Delta E = 15 \text{ mV}$ . A low anodic current of

30 pA is observed in the beginning of the polymerization process. At longer times the current-time response shows characteristic current steps with approximately equal heights of about 200 pA. This behaviour is very similar to the stepwise increase of the conductance current, observed during the electrochemical formation of metal nanocontacts, discussed in the previous section. Therefore, each current step of the current-time response shown in Figure 4.50 can be assigned to the formation of a new Au-PANI-Au junction acting as a new transmission channel. These observations show that the PS electrodeposition allows a better control of electropolymerization process and is more convenient method for preparation of nanoscale Au-PANI-Au bridges.

The conductance behaviour of various PANI bridges prepared by PS electrodeposition was characterized by cyclic voltammetry in the same electrolyte. The measurements were performed in the potential range of LM-EM transition ( $0\text{ V} < E < 0.64\text{ V}$ ), where no electropolymerization reaction takes place. In this case the cyclic voltammograms represent the potential dependence of the conductance current, which is several orders of magnitude higher than the Faraday current resulting from the red/ox processes.

In order to compare the properties of nanoscale and microscale Au-PANI-Au junctions, the conductance measurements have been performed on PANI bridges between electrodes separated with nanogaps and microgaps. The microscale PANI bridges were prepared by PS electrodeposition of PANI on the initial Au microelectrodes separated by a  $2\text{ }\mu\text{m}$  gap (cf. Figure 4.39a). Typical cyclic voltammogram of such Au-PANI-Au microbridge is shown in Figure 4.51a. As expected, during the anodic scan the conductance current behaviour reflects the red/ox transition from the insulating LM form to the conducting EM form. The large hysteresis of the conductance current observed during the anodic and cathodic scans is in agreement with previous observations on PANI microjunctions [25] and is attributed to kinetic hindrances of involved electrochemical processes and to structural relaxations of the polymer bridge.

Figure 4.51b shows the conductance current behaviour of the PANI bridge by switching the electrode potential  $E_1$  between  $0\text{ V}$  and  $0.6\text{ V}$ . As can be seen, at potential  $E_1 = 0\text{ V}$  the conductance is 0 and the PANI bridge is practically switched “off”, whereas at potential  $E_1 = 0.6\text{ V}$  corresponding to the EM form of PANI the conductance increases to more than  $100\text{ }\mu\text{S}$  and the bridge is “on”.

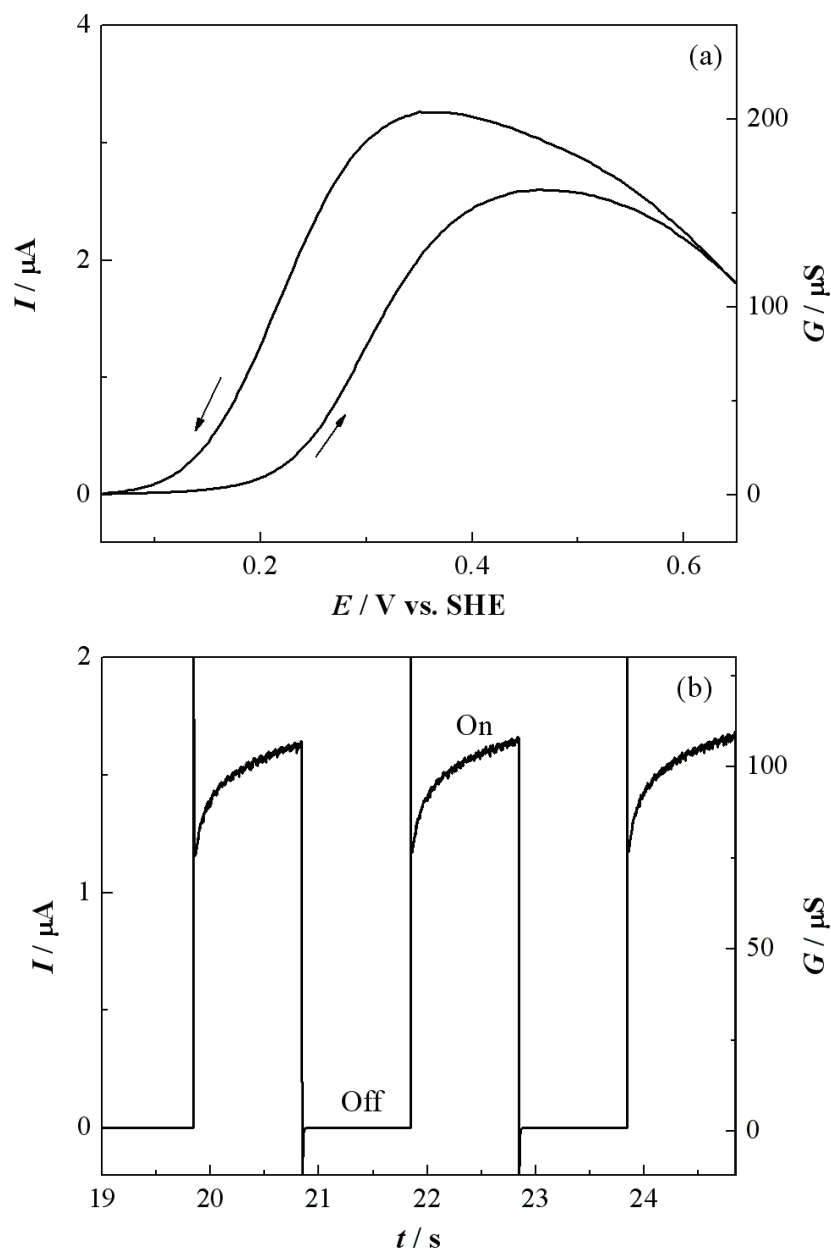


**Figure 4.51** (a): Potential dependence of the conductance current of Au-PANI-Au microbridge in 0.1M Aniline + 0.5M  $\text{H}_2\text{SO}_4$ ;  $|dE/dt| = 50 \text{ mV s}^{-1}$ ; (b): Behaviour of Au-PANI-Au microbridge in 0.1M Aniline + 0.5M  $\text{H}_2\text{SO}_4$  during multiple switching of  $E_1$  between 0V (Off) and 0.6V (On); ( $\Delta E=15\text{mV}$ ).

This “on-off” switching is stable and reproducible. As seen in Figure 4.51b, however, during the “on” stage the conductance current increases slowly without reaching a constant value. This behaviour is attributed to the slow LM-EM transformation within the relatively large PANI bridge. The SEM image presented in Figure 4.52 shows that the PANI deposit in the

Au-PANI-Au junction covers not only the Au microelectrodes but also the SiO<sub>2</sub> surface area between them.

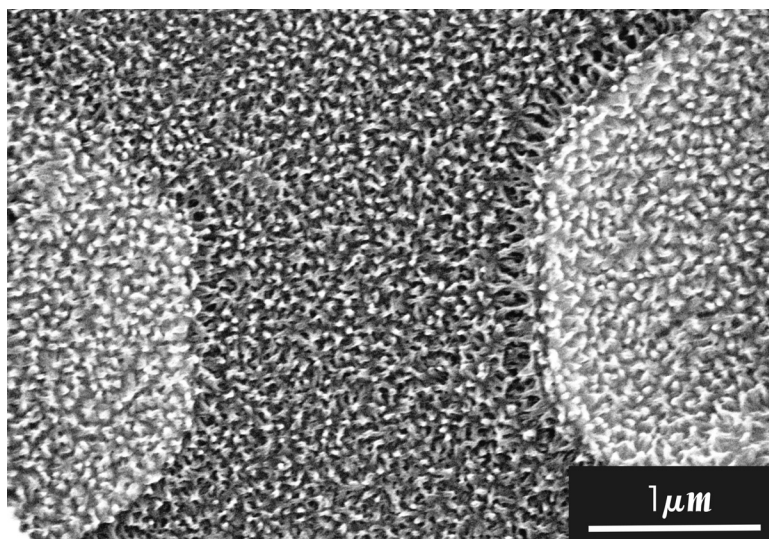


**Figure 4.52** SEM image of Au-PANI-Au microbridge deposited potentiostatically in a 2 μm gap between the two gold microelectrodes.

This observation indicates a relatively high propagation rate of PANI deposit at longer deposition times despite the insulating SiO<sub>2</sub> surface, and is in agreement with the results presented in Section 4.2. The measured high conductance values are obviously related to the large size of the PANI bridge consisting of large number polymer chains.

The conductance behaviour of prepared Au-PANI-Au nanojunctions was characterized as in the case of the microscale junctions discussed above. The cyclic voltammogram of a PANI nanojunction in the potential range of the LM-EM transition is shown in Figure 4.53a. In contrast to the microscale junction (Figure 4.51a) the cyclic voltammogram of the nanoscale PANI junction shows a smaller hysteresis and a lower conductance. This behaviour is most probably due to the much smaller number of polymer strands forming the nanobridge. The abrupt changes of the conductance current observed in the cyclic voltammogram in Figure 4.53a can be assigned to changes of the red/ox states of single polymer strands in the nanojunction.

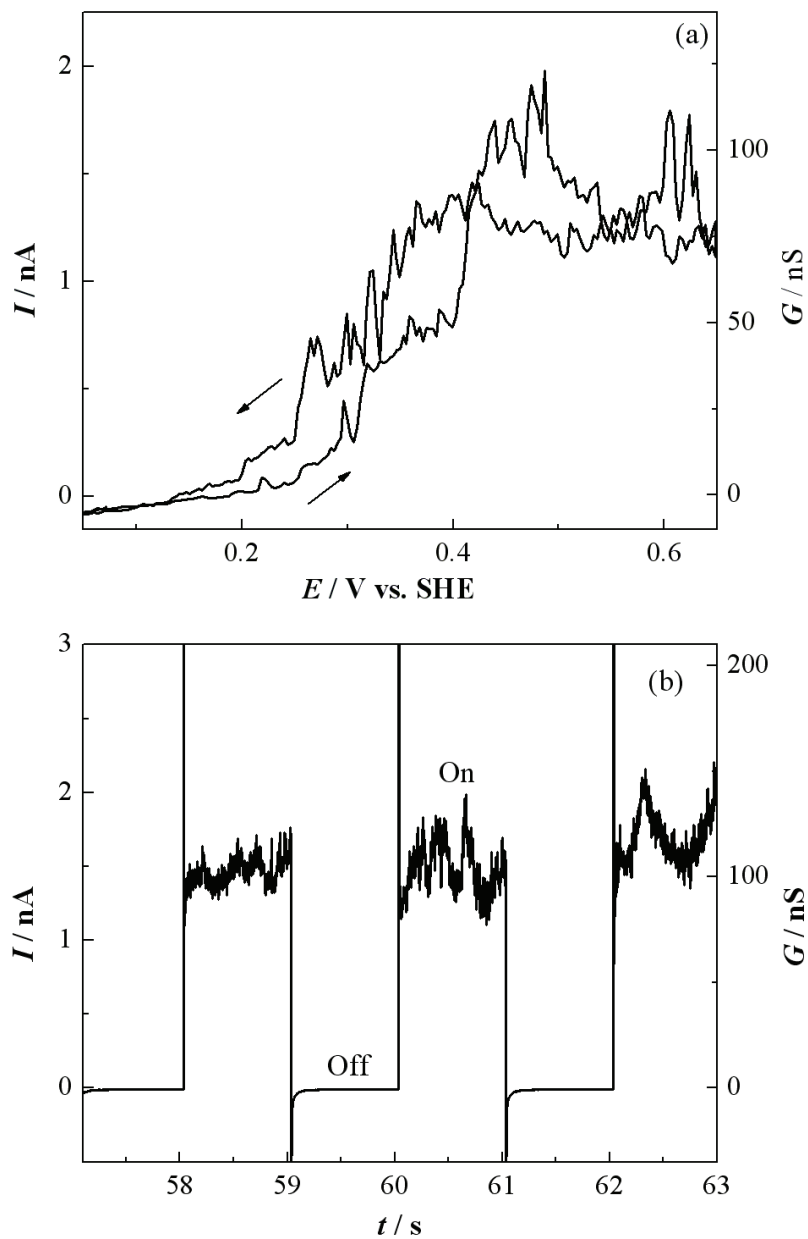


**Figure 4.53** (a): Potential dependence of the conductance current of Au-PANI-Au nanobridge in 0.1M Aniline + 0.5M  $\text{H}_2\text{SO}_4$ ;  $|dE/dt| = 50 \text{ mV s}^{-1}$ ; (b): Behaviour of Au-PANI-Au nanobridge in 0.1M Aniline + 0.5M  $\text{H}_2\text{SO}_4$  during multiple switching of  $E_1$  between 0V (Off) and 0.6V (On); ( $\Delta E=15\text{mV}$ ).

Figure 4.53b shows the conductance behaviour of the PANI nanojunction during the multiple switching of the electrode potential  $E_1$  between 0 V and 0.6 V. The observed conductance trace indicates that the charge transfer process in the nanojunction is much faster than that in the microjunction (cf. Figure 4.51b).

If the potential is kept constant at 0.6 V the conductance shows some fluctuations and a random switching between different discrete levels (Figure 4.54). The observed conductance switching is in agreement with the results reported recently by He et al. [25,26] and according to these authors can be attributed to a switching between the conducting state and insulating reduced state of individual polymer strands forming the PANI nanojunction. However, a better understanding of this phenomenon requires further more detailed experiments.

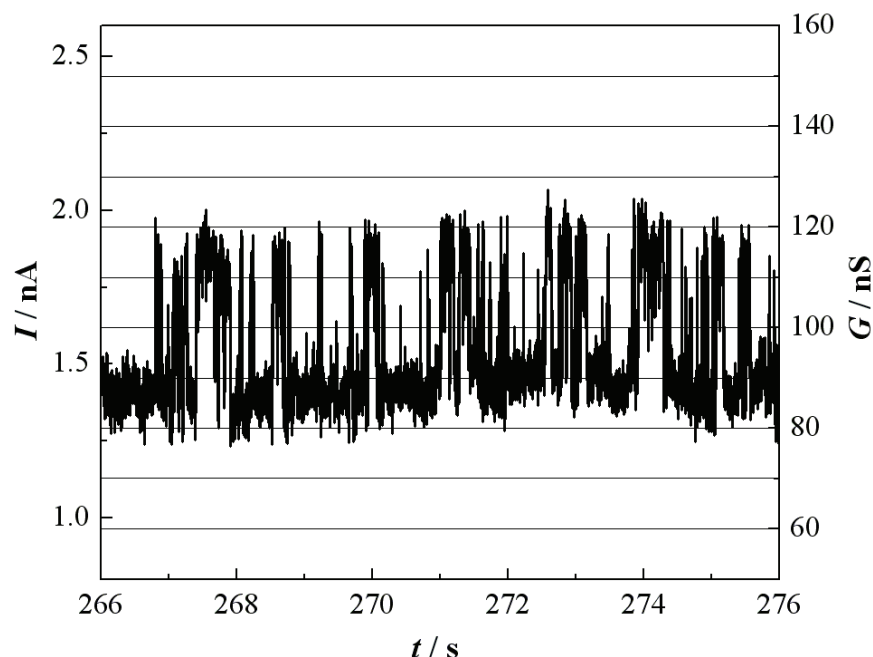


**Figure 4.54** Long term behaviour of PS deposited Au-PANI-Au nanobridge in 0.1M Aniline + 0.5M  $\text{H}_2\text{SO}_4$  at  $E_1=0.6\text{V}$  and  $\Delta E=15\text{mV}$ .

The experimental results presented above demonstrate the potentiostatic deposition of PANI can be applied successfully for preparation of Au-PANI-Au nanojunctions consisting of only few polymer strands. These nanojunctions can be used for further investigations of the potential dependence of charge transport phenomena in PANI on a nanometer scale.



## 5. Summary and Outlook

The aims of the present work were the clarification of the mechanism and kinetics of electrodeposition of gold and polyaniline (PANI) in selected electrochemical systems and the development of appropriate experimental routines for a potential controlled nanoscale modification of surfaces and structures by these processes.

The kinetics of electrochemical nucleation and growth of Au nanoparticles on glassy carbon (GC) were investigated for the first time in the systems GC/1mM KAuCl<sub>4</sub>+0.1M HClO<sub>4</sub> and GC/5mM HAuCl<sub>4</sub>+42mM Na<sub>2</sub>S<sub>2</sub>O<sub>3</sub>+42mM Na<sub>2</sub>SO<sub>3</sub>. The experimental results show that in both systems the gold electrodeposition is diffusion-controlled and follows the so-called Volmer-Weber growth mechanism involving formation and growth of 3D Au islands on an unmodified GC substrate.

The analysis of current transients for Au electrodeposition in the system GC/1mM KAuCl<sub>4</sub>+0.1M HClO<sub>4</sub> at relatively low cathodic potentials ( $E \geq 0.84\text{V}$ ) reveals that the initial deposition kinetics corresponds to a model including progressive nucleation and diffusion-controlled 3D growth of Au nanoparticles. The potential dependence of the nucleation rate extracted from the experimental current transients is in good agreement with the atomistic theory of electrochemical nucleation. The results show that at sufficiently high cathodic potentials ( $E \leq 0.64\text{V}$ ) the nucleation rate in this system becomes very high and the nucleation changes from progressive to instantaneous. Based on this behaviour was proposed a potentiostatic double-pulse routine allowing a controlled deposition of Au nanoparticles with a narrow size distribution. The Au nanoparticles deposited by this double-pulse technique were modified additionally by underpotential deposition (UPD) of Cu and a subsequent electroless displacement of the Cu UPD monolayer by Pt monolayer. The enhanced catalytic activity of the prepared Au/Pt(core/shell) nanoparticles towards the methanol electrooxidation was demonstrated by electrochemical measurements in methanol containing H<sub>2</sub>SO<sub>4</sub> solution.

The experimental results obtained in the system GC/5mM  $\text{HAuCl}_4$ +42mM  $\text{Na}_2\text{S}_2\text{O}_3$ +42mM  $\text{Na}_2\text{SO}_3$  show that the gold electrodeposition starts at relatively high cathodic potentials ( $E < -0.4\text{V}$ ) and is accompanied by hydrogen evolution. Therefore, a quantitative transient analysis based on the existing theoretical nucleation and growth models was not possible in this system. The SEM images indicate that the involved nucleation remains progressive even at very high cathodic potentials. Due to this behaviour no suitable conditions for a controlled electrodeposition of Au nanoparticles could be found in this case.

The mechanism of electrodeposition and the properties of thin PANI films on p-Si(111) and Au(111) single crystal substrates were studied by means of potentiostatic transient measurements, cyclic voltammetry, electrochemical impedance spectroscopy, SEM and AFM. The results show that the mechanism of formation, the structure and the electrochemical behaviour of the electrodeposited PANI films depend strongly on the nature and the electronic properties of the substrate. The kinetics of initial stages of PANI electrodeposition on Au(111) correspond to a model including a progressive appearance and kinetically controlled 2D growth of polymer islands. The electrodeposition of PANI on p-Si(111) is strongly inhibited due to the formation of an anodic  $\text{SiO}_2$  film, which is inhomogeneous and leads to a deposition mechanism involving progressive appearance and growth of 3D PANI islands. No electrodeposition of PANI could be obtained on p-Si(111) substrates covered by a native oxide. It was demonstrated, however, that a successful PANI electrodeposition can be achieved also in this case after additional preceding modification of oxide covered p-Si(111) substrates by photoelectrochemical cathodic deposition of Au nanoparticles acting as active sites for the electropolymerization process.

The electrodeposition of gold from the thiosulfate-sulfite electrolyte (5mM  $\text{HAuCl}_4$ +42mM  $\text{Na}_2\text{S}_2\text{O}_3$ +42mM  $\text{Na}_2\text{SO}_3$ ) was also used for surface modification of gold electrodes and preparation of nanogaps and nanocontacts. The evolution of surface morphology during gold electrodeposition on Au(111) was studied by AFM applying the so-called dynamic scaling analysis. The obtained dependences of the surface roughness on the scale length and the deposition time, and the extracted scaling exponents show that the observed morphology evolution corresponds to a deposition mechanism with surface diffusion and step growth. The experiments on preparation of nanogaps and nanocontacts were performed on pairs of planar opposite Au microelectrodes fabricated on silicon chips by conventional optical lithography. For the nanoscale modification of the initial microgaps was developed a two-step deposition

procedure allowing a precise control of the electrode separation and the formation of various nanocontacts by monitoring the changes of the conductance current flowing between the two Au microelectrodes. The experimental conductance current transients exhibit the characteristic stepwise increase due to the formation of nanocontacts. The corresponding conductance histograms show peaks near integer and fractional multiplies of the conductance quantum  $G_0 = 2e^2 / h$ . A fractional conductance quantization during the formation of Au nanocontacts has been reported recently also for other electrochemical systems and could be attributed to atomic rearrangements occurring during the gold electrodeposition. A complete understanding of this phenomenon, however, requires further more detailed studies. By monitoring of the tunnelling current increase during the electrodeposition process were successfully prepared stable Au nanogaps with different gap widths.

The bridging of electrochemically fabricated Au nanogaps by electrodeposition of PANI was studied applying different deposition techniques. The conductance behaviour of various PANI bridges was characterized by cyclic voltammetry and transient measurements in the potential range of the “on-off” switching between the conducting emeraldine (EM) and the insulating Leukoemeraldine (LM) states of PANI. The experimental results show that the potentiostatic deposition technique offers optimal conditions for preparation of Au-PANI-Au nanojunctions consisting of only several polymer strands.

Looking to future works, it is necessary to continue the studies on preparation of nanogaps and molecular nanojunctions because of their technological importance for the development of the nanoelectronics. Further experiments should be performed on Au electrode pairs with nanoscale separation, prepared via E-beam lithography. In order to clarify the questions that remained open, the behaviour of the obtained Au nanocontacts and nanogaps should be examine in different electrolytes. The Au nanogaps can be further modified by UPD of metal monolayers and by subsequent electroless displacement reactions, which were applied successfully in this thesis for modification of Au nanoparticles.

Concerning the properties of the Au-PANI-Au nanobridges their stability and conductivity can be improved by fuctionalization of the monomeric species and/or using deposition solution with specific polyanions. The electrodeposition routine used in the present work can be applied also for preparation of nanojunctions with other conducting polymers such as Polypyrrole (PPy), Polythiophene (PT) and their derivates.

## 5. Zusammenfassung und Ausblick

Die Ziele der vorliegenden Arbeit waren die Aufklärung des Mechanismus und der Kinetik der elektrochemischen Abscheidung von Gold und Polyanilin (PANI) in ausgewählten elektrochemischen Systemen und die Entwicklung geeigneter experimentellen Routinen für eine potentialkontrollierte Nanomodifizierung von Oberflächen und Strukturen mit Hilfe dieser Prozesse.

Die Kinetik der elektrochemischen Keimbildung und des Wachstums von Au Nanopartikeln auf Glaskohlenstoff (GC) wurde erstmals in den Systemen GC/1mM KAuCl<sub>4</sub>+0.1M HClO<sub>4</sub> and GC/5mM HAuCl<sub>4</sub>+42mM Na<sub>2</sub>S<sub>2</sub>O<sub>3</sub>+42mM Na<sub>2</sub>SO<sub>3</sub> untersucht. Die experimentellen Ergebnisse zeigen, dass in beiden Systemen die elektrochemische Goldabscheidung diffusionskontrolliert ist und nach dem so genannten Volmer-Weber-Wachstumsmechanismus durch Bildung und Wachstum von 3D Au-Inseln auf einem unmodifizierten GC-Substrat erfolgt.

Die Analyse der Stromtransienten, die während der elektrochemischen Goldabscheidung im System GC/1mM KAuCl<sub>4</sub>+0.1M HClO<sub>4</sub> bei relativ niedrigen kathodischen Potentialen ( $E \geq 0.84\text{V}$ ) gemessen wurden, zeigt, dass die Anfangsabscheidungskinetik einem Modell mit progressiver Keimbildung und diffusionskontrolliertem 3D Wachstum der Au-Nanopartikeln entspricht. Die Potentialabhängigkeit der aus der experimentellen Stromtransienten bestimmten Keimbildungsgeschwindigkeit ist in gute Übereinstimmung mit der atomistischen Theorie der elektrochemischen Keimbildung. Die Ergebnisse zeigen, dass bei genügend hohen kathodischen Potentialen ( $E \leq 0.64\text{V}$ ) die Keimbildungsrate stark zunimmt und die Nukleation von progressiv zu instantan wechselt. Auf der Basis dieses Verhaltens wurde eine Doppelpulsroutine vorgeschlagen, die eine kontrollierte Abscheidung von Au-Nanopartikeln mit einer schmalen Größenverteilung erlaubt. Die mit dieser Doppelpulstechnik abgeschiedenen Au-Nanopartikel wurden durch eine Unterpotential-abscheidung (UPD) von Cu und einen folgenden stromlosen Austausch der Cu-UPD-Monoschicht durch einen Pt-Monoschicht zusätzlich modifiziert. Die verstärkte katalytische Aktivität der präparierten

Au/Pt(Kern/Schale)-Nanopartikel wurde bezüglich der Methanolelektrooxidation mit Hilfe von elektrochemischen Messungen in einer methanolhaltigen  $\text{H}_2\text{SO}_4$ -Lösung demonstriert.

Die im System  $\text{GC}/5\text{mM HAuCl}_4+42\text{mM Na}_2\text{S}_2\text{O}_3+42\text{mM Na}_2\text{SO}_3$  erhaltenen experimentellen Ergebnisse zeigen, dass die elektrochemische Goldabscheidung bei relativ hohen kathodischen Potentialen ( $E < -0.4\text{V}$ ) beginnt und von einer Wasserstoffentwicklung begleitet wird. Deshalb konnte eine quantitative Analyse der Transienten in diesem System nicht durchgeführt werden. Die REM Aufnahmen weisen darauf hin, dass die involvierte Nukleation sogar bei sehr hohen kathodischen Potentialen progressiv bleibt. Wegen dieses Verhaltens konnten keine geeigneten Bedingungen für eine kontrollierte elektrochemische Abscheidung von Au-Nanopartikeln gefunden werden.

Der elektrochemische Abscheidungsmechanismus von dünnen PANI Schichten auf p-Si(111) und Au(111) wurde mit der Hilfe von potentiostatischen Transientenmessungen, zyklische Voltammetrie, elektrochemische Impedanz Spektroskopie, REM und AFM studiert. Die Ergebnisse zeigen, dass der Bildungsmechanismus, die Struktur und das elektrochemische Verhalten der Polymerschichten von der Natur und der elektronischen Eigenschaften des Substrates stark abhängig sind. Die Kinetik der Anfangsstadien der elektrochemischen Abscheidung von PANI auf Au(111) entspricht einem Modell für progressive Bildung und kinetisch kontrollierten 2D Wachstum von PANI-Inseln. Auf p-Si(111) ist die elektrochemische Abscheidung von PANI stark inhibiert wegen der anwesenden anodischen  $\text{SiO}_2$  Schicht, die inhomogen ist und zur progressiven Bildung und zum kinetisch kontrollierten 3D Wachstum von PANI-Inseln führt. Eine elektrochemische Abscheidung von PANI konnte auf p-Si(111), bedeckt mit einer natürlichen  $\text{SiO}_2$  Schicht, nicht durchgeführt werden. Es wurde demonstriert, dass eine erfolgreiche elektrochemische Abscheidung von PANI realisiert werden kann, wenn vorher das oxydbedeckte p-Si(111) Substrat durch photoelektrochemische Abscheidung von Au-Nanopartikeln modifiziert wird. In diesem Fall wirken die erzeugten Au-Nanopartikel als aktive Zentren für die Elektropolymerisation.

Die elektrochemische Abscheidung von Au aus dem thiosulfat-sulfitischen Elektrolyt ( $5\text{mM HAuCl}_4+42\text{mM Na}_2\text{S}_2\text{O}_3+42\text{mM Na}_2\text{SO}_3$ ) wurde zur Modifizierung von Goldelektroden und zur Erstellung von Nanogaps und Nanokontakte verwendet. Die Entwicklung der Oberflächenmorphologie während der Au Abscheidung auf Au(111) wurde mit AFM studiert

unter Anwendung der so genannten Dynamic Scaling Analysis. Die erhaltenen Abhängigkeiten der Oberflächenrauigkeit von der Skalenlänge und der Abscheidungszeit, sowie die extrahierten Skalierungsexponenten, weisen darauf hin, dass die beobachtete Morphologieentwicklung einem Abscheidungsmechanismus mit Oberflächendiffusion und Stufenwachstum entspricht. Die Erzeugung von Nanogaps und Nanokontakten wurde auf planaren entgegenstehenden lithographisch präparierten Au-Mikroelektroden durchgeführt. Eine zweistufige Routine wurde für die Nanomodifizierung der Mikrogaps entwickelt, die eine präzise Kontrolle des Elektrodenabstand und der Bildung verschiedener Nanokontakte durch gleichzeitige Messung des Leitfähigkeitsstromes zwischen den beiden Elektroden erlaubt. Die experimentellen Leitfähigkeitsstromtransienten weisen eine charakteristische stufenartige Erhöhung des Stromes während der Kontaktbildung vor. Die entsprechenden Leitfähigkeitshistogramme zeigen Peaks in der Nähe von Ganzzahl- und Bruchzahl-Vielfachwerten des Leitfähigkeitsquantums  $G_0 = 2e^2/h$ . Beobachtete Bruchzahl-Vielfachwerte des Leitfähigkeitsquantums wurden auch bei der Kontaktbildung aus anderen Systemen berichtet und könnten auf atomare Reorganisationsprozesse während der Au-Abscheidung zurückgeführt werden. Eine komplette Aufklärung dieses Phänomens verlangt jedoch weitere detaillierte Untersuchungen. Durch die Kontrolle des zunehmenden Tunnelstromes während der elektrochemischen Abscheidung konnten stabile Au-Nanogaps mit verschiedenen Breiten erfolgreich erzeugt werden.

Die Überbrückung der hergestellten Au-Nanogaps durch elektrochemische Abscheidung von PANI wurde unter Anwendung verschiedener Abscheidungstechniken studiert. Das Leitfähigkeitsverhalten von zahlreichen PANI Brücken wurde mit zyklischer Voltammetrie und Transientenmessungen in dem Potentialbereich des „on-off“ Umschaltens zwischen des leitfähigen Emeraldine(EM)- und des isolierenden Leukoemeraldine(LM)-Zustands untersucht. Die experimentellen Ergebnisse zeigen, dass die potentiostatische Abscheidungstechnik optimale Bedingungen für eine kontrollierte Abscheidung von Au-PANI-Au Nanobrücken bestehend nur aus einigen Polymerfäden anbietet.

Im Ausblick auf zukünftige Arbeiten sollten aufgrund der technologischen Bedeutung für die Entwicklung der Nanoelektronik weitere Untersuchungen zur Präparation von Nanogaps und molekulare Nanojunctions durchgeführt werden. Weitere Experimente sollen auf Au-Elektrodenpaare erfolgen, die mit Elektronstrahl-Lithographie hergestellt werden und einen Elektrodenabstand auf die Nanometerskala aufweisen.

Um die Fragen, die offen geblieben sind, zu beantworten, müsste das Verhalten der erzeugten Au-Nanokontakte und Nanogaps in verschiedene Elektrolyten studiert werden. Die Au-Nanogaps können durch UPD von Metallmonoschichten und durch folgende stromlose Austauschreaktionen, die in dieser Arbeit für die Modifizierung von Au-Nanopartikel erfolgreich ausgeführt wurden, weiterhin modifiziert werden.

Im Bezug auf die Eigenschaften der Au-PANI-Au –Nanobrücken, könnten deren Stabilität und Leitfähigkeit durch eine Funktionalisierung der Monomerspezies und/oder unter Anwendung von Abscheidungslösungen mit spezifischen Polyanionen verbessert werden. Die Routine für die elektrochemische Abscheidung, die in dieser Arbeit benutzt wurde, kann auch für Präparation von Nanojunctions mit weiteren leitfähigen Polymeren wie Polypirol (PPy), Polythiophen (PT) und deren Derivaten eingesetzt werden.

## 6. References

- [1] H. Fischer, *Elektrolytische Abscheidung und Elektrokristallisation von Metallen*, Springer, Berlin (1954).
- [2] M. Fleischmann, H.R. Thirsk, in: *Advances in Electrochemistry and Electrochemical Engineering*, Vol. 3, P. Delahay (Ed.), Wiley, New York (1963) p. 123.
- [3] J.A. Harrison, H.R. Thirsk, in: *Electroanalytical Chemistry*, A. Bard (Ed.), Vol. 5, Marcel Dekker, New York (1971) p. 67.
- [4] E. Budevski, G. Staikov, W.J. Lorenz, *Electrochemical Phase Formation and Growth*, VCH, Weinheim (1996).
- [5] M. Paunovic, M. Schlesinger, *Fundamentals of Electrochemical Deposition*, Wiley-Interscience, New York (1998).
- [6] A. Milchev, *Electrocrystallization: Fundamentals of Nucleation and Growth*, Kluwer Academic Publishers, Boston/Dordrecht/London (2002).
- [7] G. Staikov, in: *Electrochemical Microsystem Technologies*, J.W. Schultze, T. Osaka and M. Datta (Eds.), Taylor & Francis, London and New York (2002) p. 156.
- [8] G. Staikov, A. Milchev, in: *Electrocrystallization in Nanotechnology*, G. Staikov(Ed.), Wiley-VCH, Weinheim (2007) p. 3.
- [9] P.C. Andricacos, C. Uzoh, J.O. Dukovic, J. Horkans, H. Deligianni, *IBM J. Res. Develop.* 42 (1998) 567.
- [10] P.C. Andricacos, *Interface* 8 (1999) 32.
- [11] G. Hodes (Ed.), *Electrochemistry of Nanomaterials*, Wiley-VCH, Weinheim (2001).
- [12] G. Staikov (Ed.), *Electrocrystallization in Nanotechnology*, Wiley-VCH, Weinheim (2007).
- [13] M. Daniel, D. Astruc, *Chem. Rev.* 104 (2004) 293.
- [14] D. Lu, K. Tanaka, *J. Phys. Chem.* 100 (1996) 1833.
- [15] M.O. Finot, G.D. Braybrook, M.T. McDermott, *J. Electroanal. Chem.* 466 (1999) 234.
- [16] M.O. Finot, M.T. McDermott, *J. Electroanal. Chem.* 488 (2000) 125.
- [17] H. Liu, F. Favier, K. Ng, M.P. Zach, R.M. Penner, *Electrochim. Acta* 47 (2001) 671.
- [18] M.S. El-Deab, T. Sotomura, T. Ohsaka, *J. Electrochem. Soc.* 152 (2005) C1, C730.
- [19] M.S. El-Deab, T. Okajima, T. Ohsaka, *J. Electrochem. Soc.* 153 (2006) E201.
- [20] X. Dai, R.D. Compton, *Anal. Sci.* 22 (2006) 567.



- [21] G. Trejo, A.F. Gil, I. Gonzales, *J. Electrochem. Soc.* 142 (1995) 3404.
- [22] U. Schmidt, M. Donten, J.G. Osteryoung, *J. Electrochem. Soc.* 144 (1997) 2013.
- [23] A.J. Heeger, *Curr. Appl. Phys.* 1 (2001) 247.
- [24] G. Inzelt, m. Pineri, J.W. Schultze, M.A. Vorontyntsev, *Electrochim. Acta* 45 (2000) 2403.
- [25] H.X. He, J. Zhu, N.J. Tao, L.A. Nagahara, I. Amlani, R. Tsui, *J. Am. Chem. Soc.* 123 (2001) 7730.
- [26] H.X. He, X.L. Li, N.J. Tao, L.A. Nagahara, I. Amlani, R. Tsui, *Phys. Rev. B* 68 (2003) 045302.
- [27] P.N. Bartlett, Y. Astier, *Chem. Commun.* (2000) 105.
- [28] V. Saxena, B.D. Malhotra, *Curr. Appl. Phys.* 3 (2003) 293.
- [29] E.S. Forzani, H. Zhang, L.A. Nagahara, I. Amlani, R. Tsui, N.J. Tao, *Nano Lett.* 4 (2004) 1785.
- [30] H. Zhang, S. Boussaad, N. Ly, N.J. Tao, *Appl. Phys. Lett.* 84 (2004) 133.
- [31] A.D. Aguilar, X.L. Li, N.J. Tao, L.A. Nagahara, I. Amlani, R. Tsui, *Appl. Phys. Lett.* 87 (2005) 193108.
- [32] J. Heinze, in *Topics in Current Chemistry*, Vol. 152, M.J.S. Dewar, J.D. Dunitz, K. Hafner, E. Heilbronner, S. Ito, J.M. Lehn, K. Niedenzu, K.N. Raymond, C.V. Rees, and F. Vögtle (Eds.), Springer-Verlag, Berlin, Heidelberg (1990) p. 1.
- [33] K. Bade, V. Tsakova, J.W. Schultze, *Electrochim. Acta* 37 (1992) 2255.
- [34] V. Tsakova, J.W. Schultze, *Bulg. Chem. Commun.* 27 (1994) 138.
- [35] R. Córdova, M.A. del Valle, A. Arratia, H. Gómez, R. Schrebler, *J. Electroanal. Chem.* 377 (1994) 75.
- [36] E. Matveeva, V.P. Parkhutik, R. Diaz Calleja, J.M. Martinz-Duart, *J. Lumin.* 57 (1993)175; *Synth. Met.* 67 (1994) 111.
- [37] Z.H Yang, P. Zhang, D.J. Wang, D. Zhang, X.D. Chai, T.J. Li, *Synth. Met.* 85 (1997) 1293.
- [38] J.W. Schultze, T. Osaka and M. Datta (Eds.), *Electrochemical Microsystem Technologies*, Taylor & Francis, London and New York (2002).
- [39] G. Staikov, W.J. Lorenz, E. Budevski, in: *Imaging of Surfaces and Interfaces*, J. Lipkowski and P.N. Ross (Eds.), Wiley-VCH, New York (1999) p. 1.
- [40] E. Budevski, G. Staikov, W.J. Lorenz, *Electrochim. Acta*, 45 (2000) 2499.
- [41] A. Milchev, S. Stoyanov, R. Kaischew, *Thin Solid Films* 22 (1974) 255, 267.
- [42] A. Milchev, *Contemp. Phys.* 32 (1991) 321.

- [43] P. Bindra, A.P. Brown, M. Fleischmann, D. Pletcher, *J. Electroanal. Chem.* 58 (1975) 31.
- [44] M. Fleischmann, S. Pons, J. Sousa, J. Ghoroghchian, *J. Electroanal. Chem.* 366 (1994) 171.
- [45] M.Y. Abyaneh, M. Fleischmann, *J. Electroanal. Chem.* 530 (2002) 108.
- [46] A. Kolmogoroff, *Bull. Acad. Sci. URSS. Math. Nat.* 3 (1937) 355.
- [47] M. Avrami, *J. Chem. Phys.* 7 (1939) 1103; 8 (1940) 212; 9 (1941) 177.
- [48] M.Y. Abyaneh, M. Fleischmann, *Electrochim. Acta* 27 (1982) 1513.
- [49] B. Scharifker, G. Hills, *Electrochim. Acta* 28 (1983) 879.
- [50] B.R. Scharifker, J. Mostany, *J. Electroanal. Chem.* 177 (1984) 13.
- [51] M.V. Mirkin, A.P. Nilov, *J. Electroanal. Chem.* 283 (1990) 35.
- [52] L. Heerman, A. Tarallo, *J. Electroanal. Chem.* 470 (1999) 70.
- [53] F. Family, T. Vicsek (Eds.), *Dynamics of Fractal Surfaces*, World-Scientific, Singapore (1991).
- [54] W.M. Tong, R.S. Williams, *Ann. Rev. Phys. Chem.* 45 (1994) 401.
- [55] A.L. Barabasi, H.E. Stanley (Eds.), *Fractal Concepts in Surface Growth*, Cambridge University Press, Cambridge (1995).
- [56] W. Schwarzacher, *J. Phys.: Condens. Matter* 16 (2004) R859.
- [57] J. Krug, H. Spohn, in: *Solids Far From Equilibrium*, C. Godreche (Ed.), Cambridge University Press, Cambridge (1992) p. 479.
- [58] S.F. Edwards, D.R. Wilkinson, *Proc. R. Soc. London Ser. A* 381 (1982) 17.
- [59] M. Kardar, G. Parisi, Y-C. Zhang, *Phys. Rev. Lett.* 56 (1986) 889.
- [60] D.E. Wolf, J. Villain, *Europhys. Lett.* 13 (1990) 389.
- [61] J. Villain, *J. Phys. I* 1 (1991) 19.
- [62] Z.-W. Lai, S. Das Sarma, *Phys. Rev. Lett.* 66 (1991) 2348.
- [63] H. Shirakawa, E. J. Edwin, A. G. MacDiarmid, Ch. K. Chiang, A. J. Heeger, *J. Chem. Society, Chem. Commun.* (1977) 578.
- [64] A. J. Heeger, *Rev. Mod. Phys.* 73 (2001) 681.
- [65] A. G. MacDiarmid, *Rev. Mod. Phys.* 73 (2001) 701.
- [66] H. Shirakawa, *Rev. Mod. Phys.* 73 (2001) 713.
- [67] K. Gurunathan, A. Vadivel Murugan, R. Marimuthu, U. Mulik, D. Amalnerkar, *Mat. Chem. Phys.* 61 (1999) 173.
- [68] M. Agnelopoulos, IBM; *J. Res. & Dev.* 45 (2001) 57.
- [69] A. Pron, P. Rannou, *Prog. Polym. Sci.* 27 (2002) 135.

- [70] A. MacDiarmid, A. Epstein, *Faraday Discuss. Chem. Soc.* 88 (1989) 317.
- [71] E.T. Kang, K. G. Neoh, K.L. Tan, *Prog. Polym. Sci.* 23 (1998) 277.
- [72] S. Stafström, J. Brédas, A. Epstein, H. Woo, D. Tanner, W.Huang, A. MacDiarmid, *Phys. Rev. Lett.* 59 (1987) 1464.
- [73] D. Mohilner, R. Adams, W. J. Argersinger, Jr., *J. Am. Chem. Soc.* 84 (1962) 3618.
- [74] E. M.Genies, C. Tsintavis, *J. Electroanal. Chem.* 195 (1985) 109.
- [75] R.B. Griffiths, in: *Phase Transitions and Critical Phenomena*, Vol. 1, C. Domb and M.S. Green (Eds.), Academic Press, London, New York (1972) p. 7.
- [76] L. Kouwenhoven, *Science* 268 (1995) 1440.
- [77] M.A. Kastner, *Rev. Mod. Phys.* 64 (1992) 849.
- [78] J. K. Gimzewski, R. Moller, *Phys. Rev. B* 36 (1987) 1284.
- [79] R. M. Penner, *Scanning Microsc.* 7 (1993) 805.
- [80] S. Datta, *Electronic Transport in Mesoscopic Systems*, Cambridge University press, Cambridge (1997).
- [81] J.M. van Ruitenbeek, *arXiv:cond-mat/9910394 v1* (1999).
- [82] D. M. Kolb, F.C. Simeone, *Electrochim. Acta* 50 (2005) 2989.
- [83] H. Park, P.K.L. Lim, A.P. Alivisatos, J. Park, P.L. McEuen, *Appl. Phys. Lett.* 75 (1999) 301.
- [84] F. Chen, N.J. Tao, in: *Electrocrystallization in Nanotechnology*, G. Staikov(Ed.), Wiley-VCH, Weinheim (2007) p. 167.
- [85] C.Z. Li, H.X. He, N.J. Tao, *Appl. Phys. Lett.* 77 (2000) 3995.
- [86] G. Mészáros, S. Kronholz, S. Krathäuser, D. Mayer, T. Wandlowski, *Appl. Phys. A* 87 (2007) 569.
- [87] A.F. Morpugo, C.M. Marcus, D.B. Robinson, *Appl. Phys. Lett.* 74 (1999) 2084.
- [88] Y. V. Kervennic, H. S. Van der Zant, A. F. Morpugo, L. Gurevich, *Appl. Phys. Lett.* 80 (2002) 321.
- [89] J. Xiang, Bo Liu, S. T. Wu, B. Ren, F. Yang, B. W. Mao, Y. L. Chow, Z. Q. Tian, *Ange. Chem. Int. Ed.* 44 (2005) 1265.
- [90] A. Umeo, K. Hirakawa, *Appl. Phys. Lett.* 86 (2005) 143103.
- [91] H.X. He, S. Boussaad, B.Q. Xu, C.Z. Li, N.J. Tao, *J. Electroanal. Chem.* 522 (2002) 167.
- [92] C.Z. Li, H.X. He, A. Bogozzi, J.S. Bunch, N.J. Tao, *Appl. Phys. Lett* 76 (2000) 1333.
- [93] A. Javey, J. Guo, M. Paulsson, Q. Wang, D. Mann, M. Lundstrom, H. Dai, *Phys. Rev. Lett.* 92 (2004) 106804.

- [94] X.L. Li, H.X. He, B.Q. Xu, X.Y. Xiao, L.A. Nagahara, I. Amlani, R. Tsui, N.J. Tao, *Surf. Sci.* 573 (2004) 1.
- [95] R. Laundauer, *IBM J. Res. Dev.* 1 (1957) 223.
- [96] G. Binnig, H. Rohrer, *IBM J. Res. Dev.* 30 (1986) 355.
- [97] J. Halbritter, *Appl. Phys. A* 68 (1999) 153.
- [98] M.J. Liew, S. Roy, K. Scott, *Green Chem.* 5 (2003) 376.
- [99] T.A. Green, A.J. Liew, S. Roy, *J. Electrochem. Soc.* 150 (2003) C104.
- [100] M.J. Liew, S. Sobri, S. Roy, *Electrochim. Acta* 51(2005) 877.
- [101] T.A. Green, S. Roy, *J. Electrochem. Soc.* 153 (2006) C157.
- [102] G. Mészáros, C. Li, I. Pobelov, T. Wandlowski, *Nanotech.* 18 (2007) 424004.
- [103] H. Martin, P. Carro, A. Hernandez Creus, S. Gonzales, R.C. Salvarezza, A.J. Arvia, *Langmuir* 13 (1997) 100.
- [104] A.J. Bard, R. Parsons, J. Jordan, *Standard Potentials in Aqueous Solutions*, Marcel Dekker, New York (1985).
- [105] J.E. Anderson, S.M. Sawtelle, *Inorg. Chim. Acta* 194 (1992) 171.
- [106] A.J. Bard, L.R. Faulkner, *Electrochemical Methods: Fundamentals and Applications*, John Wiley and Sons, New York (2001).
- [107] R.M. Penner, *J. Phys. Chem. B* 106 (2002) 3339.
- [108] K. Marquez, G. Staikov, J.W. Schultze, *Trans. IMF* 80 (2002) 73.
- [109] A. Serruya, J. Mostany, B.R. Scharifker, *J. Electroanal. Chem.* 464 (1999) 39.
- [110] G. Oskam, P.C. Searson, *J. Electrochem. Soc.* 147 (2000) 2199.
- [111] A. Radisic, J.G. Long, P.M. Hoffmann, P.C. Searson, *J. Electrochem. Soc.* 148 (2001) C41.
- [112] C. Ehlers, U. König, G. Staikov, J.W. Schultze, *Electrochim. Acta* 47 (2001) 379.
- [113] A. Milchev, L. Heerman, *Electrochim. Acta* 48 (2003) 2903.
- [114] D. Grujicic, B. Pesic, *Electrochim. Acta* 50 (2005) 4426.
- [115] T. Zapryanova, A. Hrussanova, A. Milchev, *J. Electroanal. Chem.* 600 (2007) 311.
- [116] W. Shao, G. Pattanaik, G. Zangari, *J. Electrochem. Soc.* 154 (2007) D339.
- [117] A. Radisic, P.M. Vereecken, J.B. Hannon, P.C. Searson, F.M. Ross, *Nano Lett.* 6 (2006) 238.
- [118] A. Radisic, P.M. Vereecken, P.C. Searson, F.M. Ross, *Surf. Sci.* 600 (2006) 1817.
- [119] A. Radisic, F.M. Ross, P.C. Searson, *J. Phys. Chem. B* 110 (2006) 7862.
- [120] M.P. Zach, R.M. Penner, *Adv. Mater.* 12 (2000) 878.

- [121] J.L. Stickney, in: *Advances in Electrochemical Science and Engineering*, Vol. 7, R. C. Alkire and D. M. Kolb (Eds.), Wiley-VCH, Weinheim (2001) p. 1.
- [122] D.M. Kolb, *Electrochim. Acta* 45 (2000) 2387.
- [123] D.M. Kolb, in: *Advances in Electrochemical Science and Engineering*, Vol. 7, R. C. Alkire and D. M. Kolb (Eds.), Wiley-VCH, Weinheim (2001) p. 107.
- [124] E. Herrero, L.J. Buller, H.D. Abruna, *Chem. Rev.* 101 (2001) 1897.
- [125] K. Sasaki, Y. Mo, J.X. Wang, M. Balasubramanian, F. Uribe, J. mcBreen, R.R. Adzic, *Electrochim. Acta* 48 (2003) 3841.
- [126] J. Zhang, F.H.B. Lima, M.H. Shao, K. Sasaki, J.X. Wang, J. Hanson, R.R. Adzic, *J. Phys. Chem. B* 109 (2005) 22701.
- [127] H. Tang, J.H. Chen, M.Y. Wang, L.H. Nie, Y.F. Kuang, S.Z. Yao, *Applied Catalysis A: General* 275 (2004) 43.
- [128] X.G. Zhang, *Electrochemistry of Silicon and Its Oxide*, Kluwer Academic/Plenum Publishers, New York (2001).
- [129] V. Lehmann, *Electrochemistry of Silicon*, Wiley-VCH, Weinheim (2002).
- [130] D.E. Stilwell, S.M. Park, *J. Electrochem. Soc.* 135 (1988) 2254.
- [131] C.Q. Cui, L.H. Ono, T.C. Tan, J.Y. Lee, *Electrochim. Acta* 38 (1993) 1395.
- [132] O. Genz, M.M. Lohrengel, J.W. Schultze, *Electrochim. Acta* 39 (1993) 179.
- [133] K.R. Prasad, N. Munichandraiah, *Synth. Met.* 123 (2001) 459.
- [134] J. Schneir, V. Elings, P.K. Hansma, *J. Electrochem. Soc.* 135 (1988) 2774.
- [135] J. Krug, P. Politi, Th. Michely, *Phys. Rev. B* 61 (2000) 14037.
- [136] D.M. Kolb, A.S. Dakkouri, N. Batina, in: *Nanoscale Probes of the Solid/Liquid Interface*, A.A. Gewirth, H. Siegenthaler (Eds.), Kluwer Academic Publishers, Dordrecht (1995), p.263.
- [137] A.M. Pedraza, I. Villegas, P.L. Freund, *J. Electroanal. Chem.* 250 (1988) 443-449.
- [138] W.A. Heer, S. Frank, D. Ugarte, *Z. Phys. B* 104 (1997) 469.
- [139] C. Shu, C. Z. Li, H. X. He, A. Bogozi, J. S. Bunch, N.J. Tao, *Phys. Rev. Lett.* 84 (2000) 5196.
- [140] H. X. He, C. Shu, N. J. Tao, *J. Electroanal. Chem.* 522 (2002) 26.
- [141] M. Kiguchi, T. Konishi, K. Murakoshi, *Phys. Rev. B* 73 (2006) 125406.
- [142] B. Xu, H. He, S. Boussaad, N.J. Tao, *Electrochim. Acta* 48 (2003) 3085.
- [143] S. Boussaad, B.Q. Xu, L.A. Nagahara, I. Amlani, W. Schmickler, R. Tsui, N.J. Tao, *J. Chem. Phys.* 118 (2003) 889.
- [144] G. Nagy, T. Wandlowski, *Langmuir* 19 (2003) 10271.

- [145] A. Vaught, T. W. Jing, S.M. Lindsay, *Chem. Phys. Lett.* 236 (1995) 306.
- [146] V. Tsakova, A. Milchev, *Electrochim. Acta* 36 (1991) 1579.
- [147] H. N. Dinh, P. Vanýsek, V. I. Briss, *J. Electrochem. Soc.* 146 (1999) 3324.
- [148] S. -J. Choi, S. -M. Park, *J. Electrochem. Soc.* 149 (2002) E26.
- [149] S. K. Mondal, K. R. Prasad, N. Munichandraiah, *Synth. Met.* 148 (2005) 275.
- [150] V. Tsakova, A. Milchev, *J. Electroanal. Chem.* 346 (1993) 85.

## Abbreviations

1D	one-dimensional
2D	two-dimensional
3D	three-dimensional
<i>ac</i>	alternating current
AFM	atomic force microscopy
(c)	condensed bulk phase
CE	counter electrode
(el)	parent electrolyte phase
EM	Emeraldine
GC	glassy carbon
HOMO	highest occupied molecular orbital
HOPG	highly oriented pyrolytic graphite
IPC	interparticle diffusion coupling
LM	Leukoemeraldine
LUMO	lowest occupied molecular orbital
$L^{y-}$	ligand
Me	metal
$Me^{z+}$	simple metal cation
$[MeL_m]^{(my-z)-}$	complex metal ion
MSE	saturated mercury sulfate electrode
OPD	overpotential deposition
PANI	polyaniline
PD	potentiodynamic deposition
PMMA	poly-methyl-methacrylate
PN	Pernigraniline
PP	pulse-potentiostatic deposition
PPy	polypyrrol
PS	potentiostatic deposition
PT	polythiophene
RE	reference electrode

rms	root mean square surface roughness
SEM	scanning electron microscopy
SCE	saturated calomel electrode
SHE	standard hydrogen electrode
STM	scanning tunnelling microscopy
TEM	transmission electron microscopy
UHV	ultra high vacuum
UPD	underpotential deposition
WE	working electrode

## Symbols

$A, A'$	preexponential factor in the nucleation rate equation	$\text{cm}^{-2} \text{s}^{-1}$
$b$	geometric factor depending on the shape of 2D cluster	
$c$	concentration	$\text{mol cm}^{-3}$
$d$	thickness of the growing 2D particle	cm
$D$	diffusion coefficient	$\text{cm}^2 \text{s}^{-1}$
$e$	elementary charge	C
$e^-$	electron	
$E$	actual electrode potential	V
$E_{\text{3DMe}}$	Nernst equilibrium potential	V
$E^{\text{OCP}}$	open circuit potential	V
$E_{\text{fb}}$	flat band potential	V
$f_{\text{n}}$	frequency of nucleation per nucleation site	$\text{s}^{-1}$
$F$	Faraday constant	$\text{C mol}^{-1}$
$G$	conductance	S
$G_0$	conductance quantum	S
$h'$	surface height	nm
$h$	Planck's constant	J s
$H$	roughness scaling exponent	
$i_0$	exchange current density	$\text{A cm}^{-2}$
$i(t)$	overall current density	$\text{A cm}^{-2}$
$i_{\text{lim}}$	limiting current density	$\text{A cm}^{-2}$



$I_1(t)$	current for the growth of a single isolated particle	A
$I_t$	tunnelling current	A
$i_{\max}$	current maximum of a transient	A cm <sup>-2</sup>
$J$	nucleation rate	s <sup>-1</sup> cm <sup>-2</sup>
$k$	decay constant	nm <sup>-1</sup>
$k_B$	Boltzmann constant	J K <sup>-1</sup>
$k_{\text{ct}}, K_{\text{ct}}, K_d$	growth constants	
$K', K''$	constants depend on $E$ and the growth geometry	
$l$	length	cm
$L$	length scale	nm
$L_c$	critical length	nm
$m$	number of ligands	
$n$	number of monomer particles	
$n_{\text{crit}}$	number of atoms in a critical nucleus	
$N_0$	number density of active nucleation sites on the substrate	cm <sup>-2</sup>
$N_s$	saturated number density of nuclei	cm <sup>-2</sup>
$N(t)$	number density of nuclei	cm <sup>-2</sup>
$N$	number of conducting channels	
$N$	cycle number	
$Q$	redox charge density	mC cm <sup>-2</sup>
$Q_0$	initial redox charge density	mC cm <sup>-2</sup>
$Q_N$	redox charge density of the $N^{\text{th}}$ cycle	mC cm <sup>-2</sup>
$R$	gas constant	J K <sup>-1</sup> mol <sup>-1</sup>
$S$	cross sectional area	cm <sup>2</sup>
$s$	gap width	nm
$t$	time	s
$t_0$	induction period	s
$t_{\max}$	time of a current transient maximum	s
$T$	temperature	K
$T_i$	transmission probability of each mode	
$V_m$	molar volume	cm <sup>3</sup> mol <sup>-1</sup>
$w$	surface roughness	nm

$w_s$	saturated surface roughness	nm
$z$	charge number; number of transferred electrons	
$Z$	Zeldovich factor	
$\alpha$	charge transfer coefficient	
$\beta$	growth scaling exponent	
$\beta_{\text{loc}}$	local growth exponent	
$\delta_N$	the thickness of the Nernst diffusion layer	cm
$\Delta\tilde{G}(n)$	Gibbs energy of cluster formation	J
$\Delta E$	potential difference	V
$\Delta\tilde{\mu}$	electrochemical supersaturation	J mol <sup>-1</sup>
$\eta$	overpotential	V
$\theta_{\text{ext}}(t)$	extended surface fraction	
$\sigma$	conductivity	S cm <sup>-1</sup>
$\phi_i, \phi_\infty$	binding energies	J
$\Phi(n)$	work function	eV
$\omega_+$	frequency of attachment of monomer particles	s <sup>-1</sup>